



Università degli Studi di Messina

DIPARTIMENTO DI SCIENZE MATEMATICHE E INFORMATICHE,
SCIENZE FISICHE E SCIENZE DELLA TERRA

DOTTORATO DI RICERCA IN FISICA (XXXV CICLO)
SSD FIS/04

**Investigation on exclusive beam
asymmetry measurements of
 $e + p \rightarrow e + p + \pi^0$ process at CLAS12**

Supervisor:
Prof. **Giuseppe Mandaglio**

Author:
Letterio Biondo

Co-supervisor:
Dr. **Marco Battaglieri**
Prof. **Alessandro Pilloni**

Coordinatore del dottorato:
Prof.ssa **Vincenza Crupi**

Anno accademico 2021/2022

Declaration of Authorship

I, Letterio BIONDO, declare that this thesis titled, "Investigation on exclusive beam asymmetry measurements of $e + p \rightarrow e + p + \pi^0$ process at CLAS12" and the work presented in it are my own. I confirm that:

- This work was done wholly or mainly while in candidature for a research degree at this University.
- Where any part of this thesis has previously been submitted for a degree or any other qualification at this University or any other institution, this has been clearly stated.
- Where I have consulted the published work of others, this is always clearly attributed.
- Where I have quoted from the work of others, the source is always given. With the exception of such quotations, this thesis is entirely my own work.
- I have acknowledged all main sources of help.
- Where the thesis is based on work done by myself jointly with others, I have made clear exactly what was done by others and what I have contributed myself.

Signed:

Date:

UNIVERSITÀ DEGLI STUDI DI MESSINA

Abstract

PhD Program in Physics, Cycle XXXV, SSD FIS/04
Department of Mathematical and Computer Sciences, Physical Sciences and Earth
Sciences (MIFT)

Doctor of Philosophy

**Investigation on exclusive beam asymmetry measurements of $e + p \rightarrow e + p + \pi^0$
process at CLAS12**

by Letterio BIONDO

MesonEx experiment at CLAS12 studies exotic mesons production. Investigating single π^0 production is necessary before addressing the more complicated 3π reaction where the hybrid meson is expected to be seen. This thesis focuses on the extraction of beam asymmetry Σ in quasi-real photoproduction, and the comparison of the latter with the same obtained by GlueX and SLAC experiments. These experiments show discrepancies in a region that is crucial to distinguish the various production mechanisms. The results provided by CLAS12 at small Q^2 can be relevant to sort out the issue. In detail, the aim of the present work is a feasibility investigation of the π^0 beam asymmetry measurement of quasi-real photoproduction at CLAS12 using the CLAS12 Forward Tagger detector.

Contents

Declaration of Authorship	iii
Abstract	v
Introduction	1
1 The reaction $\gamma^{(*)}p \rightarrow \pi^0 p$	3
1.1 Theoretical Background	3
1.1.1 Two-to-Two Scattering Processes	3
1.1.2 Single pion photoproduction	5
1.1.3 Regge Theory	7
1.1.4 Beam Asymmetry	9
1.1.5 From Two-to-Three to Two-to-Two Scattering Process	11
Electron-Proton Scattering	11
Process Factorization	12
1.2 Previous Results	14
1.2.1 SLAC	14
1.2.2 GlueX	16
2 Experimental Setup	17
2.1 Facility	17
2.1.1 Hall B Beamline	19
2.2 CLAS12	20
2.2.1 Superconductive Magnets	22
The Torus Magnet	22
The Solenoid Magnet	22
2.2.2 Forward Detector	23
Drift Chamber (DC)	23
High Threshold Cherenkov Counter (HTCC)	24
Low Threshold Cherenkov Counter (LTCC)	25
Ring Imaging Cherenkov Detector (RICH)	25
Forward Time-of-Flight (FTOF)	26
Electromagnetic Calorimeters (ECAL)	27
Forward Tagger (FT)	27
2.2.3 Central Detector	28
Central Vertex Tracker (CVT)	29
Central Time-of-Flight (CTOF)	30
Central Neutron Detector (CND)	31
Back Angle Neutron Detector (BAND)	31
2.3 Forward Tagger	32
2.3.1 Detector Layout	34
The Calorimeter (FT-Cal)	34
The Hodoscope (FT-Hodo)	35

	The Micromegas Tracker (FT-Trk)	36
2.3.2	Events Reconstruction	37
2.3.3	Detector Performance	38
	Acceptance	38
	Energy Resolution and Electromagnetic Shower Reconstruction	38
	Timing Resolution	40
2.3.4	Trigger System	42
	Forward Tagger Trigger	43
3	Data Analysis	45
3.1	RunGroup-A Description	45
3.1.1	CLAS12 Reconstruction Software	46
3.2	Analysis Framework	51
3.2.1	CLAS12 Offline Software	51
	GEANT4 & GEMC	52
	GEMC Detailed Description	54
	GEMC Forward Tagger Digitization	58
	HIPO files	61
	Data Structure and Banks	61
	CoatJava	63
3.2.2	ROOT	64
3.2.3	CLAS12ROOT	64
	Custom Classes and Methods	64
3.2.4	RooFit	64
	BruFit	65
	sPlot	65
3.3	Analysis Process	67
3.3.1	The Missing Mass Method	69
3.3.2	Applied Cuts and Filters	70
	Time Coincidence	70
	Invariant Mass M_{π^0}	71
	Sum of Photons Momenta $P_{\gamma_1} + P_{\gamma_2}$	71
	Proton Missing Mass Refinishing	73
3.3.3	Energy Correction	75
3.3.4	Kinematic Regions Boundaries Selection	75
3.3.5	Beam asymmetry Σ preliminary extraction	76
3.3.6	Detector Acceptance Analysis	77
4	Results and Conclusions	83
A	Forward Tagger Trigger Settings	85
B	Monte Carlo Particle Numbering Scheme	101
C	CLAS12Root Classes and Methods	103
	Bibliography	109

List of Figures

1.1	2 in 2 scattering process scheme.	3
1.2	2 in 2 scattering process scheme in terms of center of mass.	4
1.3	Photoproduction in the GJ frame	6
1.4	Schematic representation of the reaction	7
1.5	Chew-Frautschi plot	8
1.6	Differential π^0 photoproduction cross section	9
1.7	Prediction for the Beam Asymmetry	10
1.8	Kinematics of π^0 electroproduction	13
1.9	Latest measurements of Beam Asymmetry	15
2.1	CEBAF and JLab facility	17
2.2	CLAS12 side view from design model	18
2.3	Hall B beamline section	19
2.4	CLAS12 photograph	20
2.5	CLAS12 magnet system	21
2.6	CLAS12 Drift Chambers	23
2.7	CLAS12 High Threshold Cherenkov Counter	24
2.8	CLAS12 Low Threshold Cherenkov Counter	25
2.9	CLAS12 Ring Imaging Cherenkov Detector	26
2.10	CLAS12 Forward Time-Of-Flight Detector and Electromagnetic Calorimeter	27
2.11	CLAS12 Central Detector	28
2.12	CLAS12 Central Vertex Tracker	29
2.13	CLAS12 Central Time Of Flight	30
2.14	CLAS12 fully assembled Central Detector	31
2.15	Forward Tagger CAD drawing	32
2.16	Forward Tagger CAD drawing (CLAS12 integration)	33
2.17	Forward Tagger Calorimeter)	34
2.18	Forward Tagger Hodoscope)	36
2.19	Forward Tagger Micromegas Tracker	37
2.20	Forward Tagger acceptance	39
2.21	FT-Cal shower radius	40
2.22	Time resolution for FT	41
2.23	Time correlation for FT subdetectors	41
2.24	Electron trigger rate.	43
3.1	Distance of the particle trajectory's closest approach to the detector hit.	47
3.2	CED display of a charged particle track penetrating the material of the CLAS12 forward detector.	48
3.3	Comparison of Electron Vertex Time and Reported RF Time.	50
3.4	GEMC interface from JLab computer center webpage.	52
3.5	GEMC architecture.	53
3.6	GEMC application example.	55

3.7	GEMC hit detection algorithm.	56
3.8	FADC Digitized Output and Trigger Optimization.	57
3.9	GEMC Forward Tagger implementation.	60
3.10	CoatJava event visualization example.	64
3.11	Electron-photon time correlation	68
3.12	π^0 invariant mass comparison	69
3.13	Proton missing mass to π^0	70
3.14	Detected photons momenta comparison	71
3.15	Cut efficiency tests	72
3.16	Final cut on photons momenta	73
3.17	Brufit application on given dataset	74
3.18	Energy correction.	75
3.19	t' distribution for π^0 exclusive electroproduction	76
3.20	Kinematic region of interest selection.	77
3.21	Phi fitting for Σ extraction	78
3.22	Acceptance calculation example.	79
3.23	Acceptance for different t ranges.	80
3.24	Acceptance corrected beam asymmetry.	81
3.25	Highlight of the studied $-t$ regions.	82

List of Abbreviations

CEBAF	C ontinuous E lectron B eams A ccelerator F acility
CLAS12	C EBAF L arge A cceptance S pectrometer 12 (GeV)
CM	C enter (of) M ass
CND	C entral N eutron D etector
CTOF	C entral T ime O f F light
CVT	C entral V ertex T racker
DC	D rift C hamber
EC	E lectromagnetic C alorimeter
FADC	F lash A nalog to D igital C onverter
FT	F orward T agger
FTCAL	F orward T agger C ALorimeter
FTHODO	F orward T agger H ODOscope
FTOF	F orward T ime O f F light
HIPO	H Igh P erformance O utput
HTCC	H IGH T hreshold C herenkov C ounter
LINAC	L INEar A ccelerator
LTCC	L ow T hreshold C herenkov C ounter
PCAL	P reshower C alorimeter
PWA	P artial W ave A nalysis
RF	R adio F requency

Introduction

The investigation of hadron structure, taking into account the existence of exotic hybrid mesons, is nowadays led by meson spectroscopy experiments focused on the analysis of quark-antiquark-gluon bound states.

Exotic hybrid mesons are a class of mesons that are characterized by the presence of gluonic excitations within their quark-antiquark structure. Unlike conventional mesons composed solely of quark-antiquark pairs, exotic hybrid mesons exhibit unique quantum numbers, such as exotic quantum charges and hybrid quantum numbers. Their investigation offers valuable insights into the fundamental dynamics of quantum chromodynamics (QCD) and aids in elucidating the role of gluonic degrees of freedom in the hadron spectrum.

Hybrid mesons gluonic degrees of freedom can be clearly analyzed by a Partial Wave Analysis (PWA). PWA is a powerful technique employed in high-energy physics to unravel the underlying structure of particle interactions. It involves decomposing the scattering process into distinct angular momentum states known as partial waves. By analyzing the angular distributions of the scattered particles, PWA enables the determination of resonance parameters, phase shifts, and decay properties.

While the PWA containing exotic waves can be used on exotic mesons, they present large particle multiplicity decays, making high-performance experimental apparatus mandatory to carry on this research.

The MesonEx experiment, started in 2016 and located in the Hall B of the Thomas Jefferson National Laboratory (VA, USA), is one of these experiments, and is aimed to provide fully reconstructed high statistic data of large multiplicity decay events thanks to CLAS12 detector.

The detector provides a large coverage of the forward angle ($2^\circ \leq \theta \leq 125^\circ$), aiming for the reconstruction of forward-boosted reactions due to the 6-12 GeV energy of the electron beam produced by CEBAF, the Continuous Electron Beam Accelerator Facility.

In the specific case discussed in this thesis, the analysis will be focused on meson (π^0) electro-production at beam energies up to 11 GeV. The Forward Tagger apparatus has been fundamental for the experiment, making it possible to extend the analysis to quasi-real photo-production processes characterized by low Q^2 values.

The extraction of the beam asymmetry Σ for the studied reaction may be used for the confirmation of Regge theory for high energy scattering.

Two experiments with the same target, GlueX, and SLAC, analyzed the same reaction investigated in this thesis, bringing deeply different results. The implication of understanding the reason for this strong disagreement can be crucial in the comprehension of the mechanism of the production of the exchange particles.

The chapters in this thesis will be divided as follow:

- **Chapter 1:** Composed of two sections, gives the basis for a better understanding of the content of this thesis. The first section is focused on some of the theories implied in this work, while the other two are aimed at the description of GlueX and SLAC. The aforementioned experiments are only briefly described, being a comparison with the one detailed in this thesis: MesonEx.
- **Chapter 2:** Composed of three sections, this chapter gives an overview of the experimental setup and the tools that have been used during the data acquisition. The facility and the detectors are described in the first two sections. Particular attention is given to the Forward Tagger detector, treated separately in the third section, as a fundamental instrument for the analysis presented in this thesis.
- **Chapter 3:** Composed of two sections, this part of the thesis is focused on the explanation of the analysis done on the research data. While the key instrument of the analysis (*CLAS12ROOT*, *BruFit*, *GEMC*) are briefly presented in the first section, the whole analysis process carried on during the investigations is shown and explained in the latter. The different cuts applied to the dataset and the detector acceptance analysis are presented in this last section.
- **Chapter 4:** The last chapter summarizes the research results, highlighting the process steps, the obtained information, and the next options for the ongoing analysis.

Chapter 1

The reaction $\gamma^{(*)}p \rightarrow \pi^0 p$

1.1 Theoretical Background

In this section of the thesis, some theoretical notions are reported, helping in a better understanding of the following chapter. Starting from the mathematical formulation for the Mandelstam Variables investigating two-to-two scattering processes, the section dives into a brief description of the photon-proton scattering, fundamental for the analysis and decomposition of the π^0 electro-production process in a simpler two-to-two reaction. Following, the definition of the Beam Asymmetry Σ and an introduction to Regge Theory, the chapter shows a description of how to reconduce the two-to-three process subject of this thesis, treating it, with reasonably good approximation, as a two-to-two scattering process. Natural units $\hbar = c = 1$ will be adopted hereafter.

1.1.1 Two-to-Two Scattering Processes

It is often helpful to introduce Lorentz-invariant variables, in order to separate the dependence on physical variables from the ones related to frame choice and to the orientation of the detector in the lab frame. This simplifies the analysis and notation. In particular, it is customary to adopt the *Mandelstam Invariants*. These quantities will be now explained for a better understanding of the next chapters. Please note that the derivation from López, 2017 has been followed.

Suppose that a 2-body \rightarrow 2-body scattering process is occurring; given $p_{1,2,3,4}$, which are respectively the 4-momenta of the particles involved in the process, it can be described as follow:

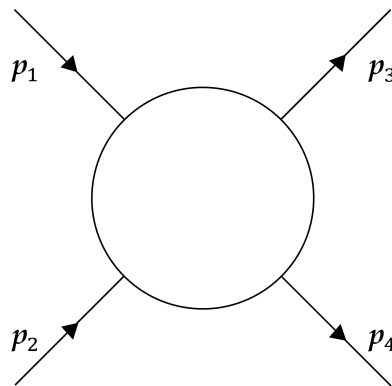


FIGURE 1.1: Two particle to two particle scattering process scheme. In this picture, $\mathbf{p}_{1,2}$ and $\mathbf{p}_{3,4}$ are, respectively, the 3-momenta of the particles in the initial and final state.

$$(p_1, p_2) \rightarrow (p_3, p_4).$$

Known the relation between the i -th particle 4-momentum \vec{p}_i and invariant mass m_i , which is

$$p_i^2 = (p_{i0}, p_{i1}, p_{i2}, p_{i3})^2 = p_{i0}^2 - p_{i1}^2 - p_{i2}^2 - p_{i3}^2 = m_i^2, \quad (1.1)$$

and the *mass-energy equivalence* for the four cases ($E_i, i = 1, 2, 3, 4$),

$$E_i^2 = \mathbf{p}_i^2 + m_i^2, \quad (1.2)$$

it is possible, without loss of generality, to express the 4-momenta of the particles involved in the process in terms of the center of mass (CM) frame:

$$\begin{aligned} p_1 &= (E_1, 0, 0, |\mathbf{p}_1|), \\ p_2 &= (E_2, 0, 0, -|\mathbf{p}_1|), \\ p_3 &= (E_3, 0, |\mathbf{p}_3| \sin \theta, |\mathbf{p}_3| \cos \theta), \\ p_4 &= (E_4, 0, -|\mathbf{p}_3| \sin \theta, -|\mathbf{p}_3| \cos \theta), \end{aligned}$$

where θ is defined as the angle between particles 1 and 3 in the CM.

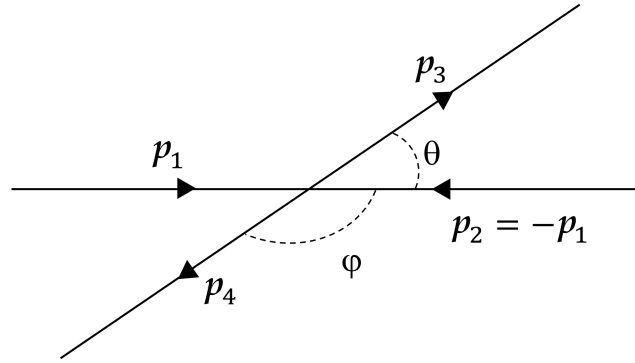


FIGURE 1.2: Two particles to two particles scattering process scheme expressed in terms of the reaction center of mass. In this picture, $\mathbf{p}_{1,2}$ and $\mathbf{p}_{3,4}$ are, respectively, the 3-momenta of the particles in the initial and final state. The scattering angle θ is also shown.

The *Mandelstam variables* can now be defined as:

$$s = (p_1 + p_2)^2 = (p_3 + p_4)^2; \quad (1.3)$$

$$t = (p_1 - p_3)^2 = (p_2 - p_4)^2; \quad (1.4)$$

$$u = (p_1 - p_4)^2 = (p_2 - p_3)^2. \quad (1.5)$$

The variable s corresponds to the total CM energy squared, while t and u are momentum transferred, depending on the particle numbering. It is conventional to consider t as the squared difference of the initial and final momenta of the most similar particles.

Using relation No.(1.1) along with the momentum conservation,

$$p_1 + p_2 = p_3 + p_4,$$

it is possible to write:

$$s + t + u = p_1^2 + p_2^2 + p_3^2 + p_4^2 = m_1^2 + m_2^2 + m_3^2 + m_4^2,$$

showing that the three variables are not independent, two of them being sufficient to characterize the kinematics. Mixing the latter with equations No.(1.2) and No.(1.3)–(1.5), it is possible to write:

$$|\mathbf{p}_{1,3}^2| = \frac{(s - m_{1,3}^2 - m_{2,4}^2)^2}{4s},$$

$$t = (\vec{p}_1 - \vec{p}_3)^2 = (E_1 - E_3)^2 - \mathbf{p}_3^2 - \mathbf{p}_1^2 + 2\mathbf{p}_1^2 \mathbf{p}_3^2 \cos \theta,$$

leading finally to the relations between the Mandelstam variables and the kinematic parameters of the reaction:

$$t = m_1^2 + m_3^2 - 2\sqrt{m_1^2 + \mathbf{p}_1^2}\sqrt{m_3^2 + \mathbf{p}_3^2} + 2\mathbf{p}_1^2 \mathbf{p}_3^2 \cos \theta \quad (1.6)$$

$$u = m_1^2 + m_2^2 + m_3^2 + m_4^2 - s - t. \quad (1.7)$$

If the particles involved carry spin, the amplitude will depend on additional discrete variables related to their polarization. Generally polarizations are frame-dependent observables, so that the frame in which they are defined must be specified. Hereafter we will consider mostly the CM frame, with particle spin quantized along their direction of motion (*helicity basis*), see e.g. Jacob and Wick, 1959.

1.1.2 Single pion photoproduction

Single pion photoproduction on a nucleon is one of the key reactions in hadron physics. At low energies, it is used to excite nucleon resonances while at high energies it can be used to test predictions of Regge theory, as we will discuss later. In the CM frame, the amplitude is $F(s, t)_{\lambda_\gamma \lambda; \lambda'}$, where $\lambda_\gamma = \pm 1$ is the photon helicity, and $\lambda^{(\prime)}$ the helicity of target (recoil) proton in the CM frame. The pion is spinless, so there is no helicity index related to it. The unpolarized cross section is given by

$$\frac{d\sigma(s, t)}{dt} = \frac{1}{16\pi(s - m_p^2)^2} \times \frac{1}{4} \sum_{\lambda_\gamma \lambda \lambda'} |F(s, t)_{\lambda_\gamma \lambda; \lambda'}|^2, \quad (1.8)$$

where the separate factor 1/4 takes into account the average over initial polarizations.

For the photon, the helicity eigenstate corresponds to circular polarization. Linearly polarized photons can be derived using the density matrix formalism. In the Gottfried-Jackson frame shown in Fig 1.3, the polarization vector of the photon is $\boldsymbol{\varepsilon}(\Phi) = (\cos \Phi, \sin \Phi, 0)$, which leads to the pure photon state (see Schilling, Seyboth, and Wolf, 1970 and Walker, 1969)

$$|\Phi\rangle = -\frac{1}{\sqrt{2}} \left[e^{-i\Phi} |+\rangle - e^{i\Phi} |-\rangle \right]. \quad (1.9)$$

The helicity states $|\pm\rangle \equiv |\lambda = \pm 1\rangle$ are defined in the Cartesian basis by $\boldsymbol{\varepsilon}(\lambda = \pm 1) = (\mp 1, -i, 0)/\sqrt{2}$. The density matrix for a pure photon state in Eq. (1.9) is thus

$$\rho_{\text{pure}}(\Phi) = |\Phi\rangle \langle \Phi| = \frac{1}{2} \begin{pmatrix} 1 & -e^{-2i\Phi} \\ -e^{2i\Phi} & 1 \end{pmatrix}. \quad (1.10)$$

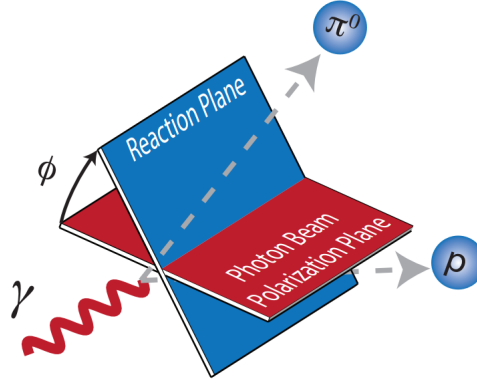


FIGURE 1.3: Representation of the process in the GJ frame, with the target proton at rest. The photon beam defines the z axis, and the xz plane contains the photon momentum and polarization. The reaction plane contains the photon, π^0 and recoil proton momenta. The Φ is the angle between the polarization and reaction planes. Courtesy of A. Austregesilo.

To describe a partially linearly polarized beam we consider a statistical mixture of the pure states $|\pm\rangle$ and $|\Phi\rangle$. The degree of polarization P_γ is the probability ($0 \leq P_\gamma \leq 1$) of finding the state $|\Phi\rangle$ in the statistical ensemble. The density matrix is thus:

$$\begin{aligned} \rho(\Phi, P_\gamma) &= \frac{1 - P_\gamma}{2} \left(|+\rangle\langle +| + |-\rangle\langle -| \right) + P_\gamma |\Phi\rangle\langle \Phi| \\ &= \frac{1}{2} (I + P_\gamma(\Phi) \cdot \sigma) , \end{aligned} \quad (1.11)$$

where the vector $P_\gamma(\Phi)$ depends on P_γ and Φ , $P_\gamma = -P_\gamma (\cos 2\Phi, \sin 2\Phi, 0)$. The cross section becomes:

$$\frac{d\sigma(s, t; \Phi, P_\gamma)}{dt} = \frac{1}{16\pi(s - m_p^2)^2} \sum_{\lambda_\gamma \lambda'_\gamma} \rho(\Phi, P_\gamma)_{\lambda_\gamma \lambda'_\gamma} \times \frac{1}{2} \sum_{\lambda \lambda'} F_{\lambda_\gamma \lambda; \lambda'}(s, t) F_{\lambda'_\gamma \lambda; \lambda'}^*(s, t). \quad (1.12)$$

If $P_\gamma = 0$, the ρ matrix is proportional to the identity matrix, and we recover the formula for the unpolarized cross section. We define $d\sigma_\parallel$ the differential cross section for $\Phi = 0$, when the photon polarization lies on the reaction plane. Similarly, we define $d\sigma_\perp$ the differential cross section for $\Phi = \pi/2$, when the production plane is orthogonal to the reaction plane.

$$\frac{d\sigma_\parallel(s, t)}{dt} = \frac{1}{16\pi(s - m_p^2)^2} \sum_{\lambda_\gamma \lambda'_\gamma} \frac{1}{2} \left(\delta_{\lambda_\gamma \lambda'_\gamma} - P_\gamma \delta_{\lambda_\gamma, -\lambda'_\gamma} \right) \times \frac{1}{2} \sum_{\lambda \lambda'} F_{\lambda_\gamma \lambda; \lambda'}(s, t) F_{\lambda'_\gamma \lambda; \lambda'}^*(s, t) \quad (1.13)$$

$$\frac{d\sigma_\perp(s, t)}{dt} = \frac{1}{16\pi(s - m_p^2)^2} \sum_{\lambda_\gamma \lambda'_\gamma} \frac{1}{2} \left(\delta_{\lambda_\gamma \lambda'_\gamma} + P_\gamma \delta_{\lambda_\gamma, -\lambda'_\gamma} \right) \times \frac{1}{2} \sum_{\lambda \lambda'} F_{\lambda_\gamma \lambda; \lambda'}(s, t) F_{\lambda'_\gamma \lambda; \lambda'}^*(s, t). \quad (1.14)$$

Again, for $P_\gamma = 0$ the two cross sections are both equal to the unpolarized one.

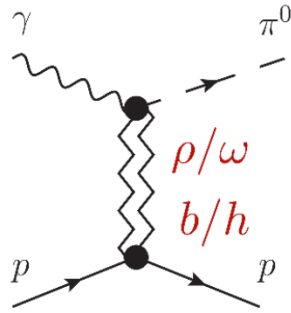


FIGURE 1.4: Schematic representation of the reaction. The process can be explained with Reggeon exchanges. Top and bottom vertices factorize.

1.1.3 Regge Theory

Regge theory is a framework developed in the 1950s and 1960s that provides a way to understand the behavior of elementary particles at high energies, for a reference book see Collins, 2009.

The central idea of the theory is the description of the scattering of particles thanks to the study of their angular momentum properties. The exchange of a fixed-spin particle with spin J implies an amplitude growing asymptotically as s^J . If one admits the existence of particles with arbitrary high spin, this is clearly unphysical. Regge theory focuses on the exchange of a full tower of particles with increasing spin, defined *Reggeons*, in scattering processes. This results in a sum over J , which makes the amplitude well behaved at large s .

One of the key results of Regge theory is that poles in the complex angular momentum plane correspond to the exchange of such particle tower, described by a function $\alpha(t)$ called *Regge trajectory*. The particles on the trajectory satisfy $J = \alpha(m_J^2)$, where J is the particle spin. As shown in Fig. 1.5 these trajectories are well approximated by linear functions, $\alpha(t) \simeq \alpha_0 + \alpha' t$. Although for technical reasons particles with odd and even spin cannot belong to the same tower, most of them lie on the same trajectory (*exchange degeneracy*, EXD). These Reggeons behave like particles, which means that the whole amplitude factorizes into a propagator, and a top and bottom vertices (smooth functions of t). This is schematically represented in Fig. 1.4.

The Reggeon propagator is given by

$$R(s, t) = \frac{\pi}{\Gamma(\alpha(t))} \frac{1 + \tau e^{-i\pi\alpha(t)}}{2 \sin \pi\alpha(t)} \left(\frac{s}{s_0} \right)^{\alpha(t)-1}, \quad (1.15)$$

where $\tau = (-1)^J$ is the so-called signature, and $s_0 = 1 \text{ GeV}^2$ sets the scale. The factor $\sin \pi\alpha(t)$ has poles for all integers $\alpha(t) = J$, while the factor $1 + \tau \exp[-i\pi\alpha(t)]$ cancels the poles the odd (even) ones. The additional $\Gamma(\alpha(t))$ in the denominator cancels the unphysical poles for negative integer J (the case $J = 0$ will be discussed later). This amplitude grows like $s^{\alpha(t)-1} \gtrsim s^{\alpha_0-1}$, being t negative in the physical region. That means that the amplitude will decrease if $\alpha_0 < 1$, as happens in the known meson trajectories. The possibility $\alpha_0 \simeq 1$ which is realized by gluonic exchanges (*Pomeron*) and is responsible for the logarithmic growth of total cross sections at high energies will not be discussed any further.

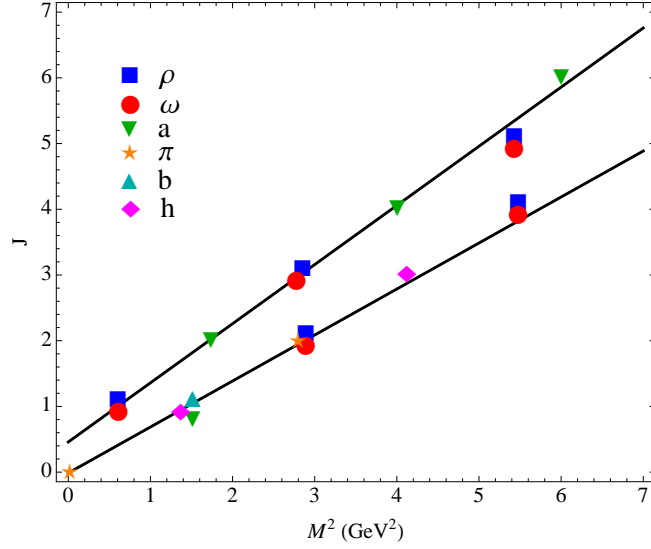


FIGURE 1.5: Chew-Frautschi plot of mass vs. spin of the exchanged particles. One sees that particles with natural and unnatural parity belong to different trajectories. On each trajectory, particles with both odd and even spin are found. This feature is called Exchange Degeneracy (EXD), and according to Regge theory it is accidental. Figure from Mathieu et al., 2018.

For the case of neutral pion photoproduction, the exchange must be neutral as well. The charge conjugation is fixed to be $C = -1$ from the top vertex. Each reggeon is usually identified with the lightest (lowest spin) meson on the trajectory. We consider the odd-signature trajectories only:

- ρ^0 exchange, with $I = 1$ and $J^{PC} = 1^{--}, 3^{--}, \dots$, and naturality $\eta = P(-1)^J = +1$;
- ω exchange, with $I = 0$ and $J^{PC} = 1^{--}, 3^{--}, \dots$, and naturality $\eta = P(-1)^J = +1$;
- b_1 exchange, with $I = 1$ and $J^{PC} = 1^{+-}, 3^{+-}, \dots$, and naturality $\eta = P(-1)^J = -1$;
- h_1 exchange, with $I = 0$ and $J^{PC} = 1^{+-}, 3^{+-}, \dots$, and naturality $\eta = P(-1)^J = -1$.

Even-signature trajectories are either exotic (like b_2 with $J^{PC} = 2^{+-}$) or allowed but never observed (like the ρ_2 with $J^{PC} = 2^{--}$), so their contribution is likely small and will not be considered.

The values of the trajectory parameter are given by (in GeV units)

$$\rho, \omega : \alpha(t) = 1 + 0.9(t - m_\rho^2) \sim 0.5 + 0.9t \quad (1.16a)$$

$$b_1, h_1 : \alpha(t) = 1 + 0.7(t - m_{b_1}^2) \sim 0.7t \quad (1.16b)$$

After considering the trajectories, one can analyze the couplings, generally referred to as Regge residues. These are analytical functions of t and can have zeros forced by spin considerations. In particular, since the photon always carries helicity 1 and the pion is spinless, the Reggeon must have at least $J = 1$ in order to enforce

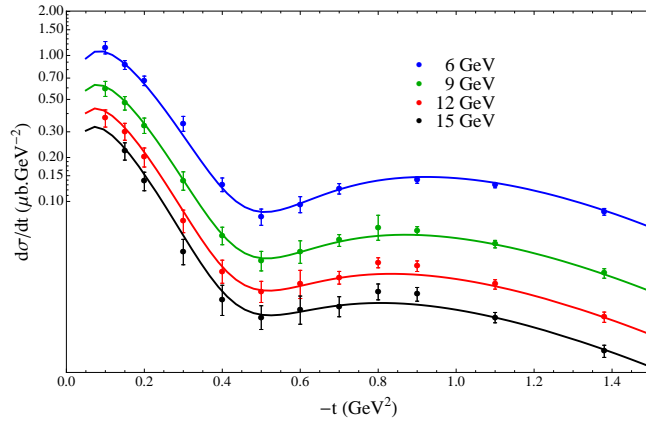


FIGURE 1.6: Differential cross section for neutral pion photoproduction. The dip at $t = -0.5 \text{ GeV}^2$ is due to the nonsense point as discussed in the text. From Mathieu, 2015.

angular momentum conservation. This can be realized by adding a zero in the top coupling when $\alpha(t) = 0$. In this model this is more simply achieved by adding $\Gamma(\alpha(t))$ in the denominator of Eq. (1.15).

Additionally, one can consider the presence of cuts in the complex angular momentum plane, that correspond to rescattering (box diagrams) of the various reggeons. Phenomenologically, they can be taken into account with a pole-like propagator, with an ad-hoc trajectory,

$$R_c(s, t) = \frac{1}{\log(s/s_0)} \frac{\pi}{\Gamma(\alpha_c(t))} \frac{1 - e^{-i\pi\alpha_c(t)}}{2 \sin \pi\alpha_c(t)} \left(\frac{s}{s_0}\right)^{\alpha_c(t)-1}. \quad (1.17)$$

with $\alpha_c(t) \sim 0.5 + 0.2t$.

The differential cross section in the energy range $E_\gamma = 6 - 15 \text{ GeV}$ is shown in Fig. 1.6. It has a dip at $t \sim -0.5 \text{ GeV}^2$. This value of momentum transfer is close to the wrong signature point of the vector trajectory when $\alpha(t) = 0$. At this point, as explained above, the vector exchange is expected to vanish since it corresponds to a nonsense point, i.e. an unphysical helicity coupling. The minimum seen in the data has therefore a clear interpretation within the Regge theory, at least at energies high enough.

At the nonsense point the cross section will never actually vanish, but one will be sensitive to subleading effects. These can be nonvanishing axial exchanges, or Regge cuts. As we will discuss in the next section, these impact differently the prediction for the beam asymmetry.

More details can be found in Collins, 2009 and Mathieu, 2015.

1.1.4 Beam Asymmetry

The Beam Asymmetry Σ is a measurable quantity that characterizes the asymmetry in the scattering of particles related to the direction of the incident beam, and for single pion photoproduction is directly related to the naturality of the exchange.

Such quantity is defined as the ratio of the difference to the sum of the cross-sections for photon linear polarization perpendicular and parallel as defined in the previous section:

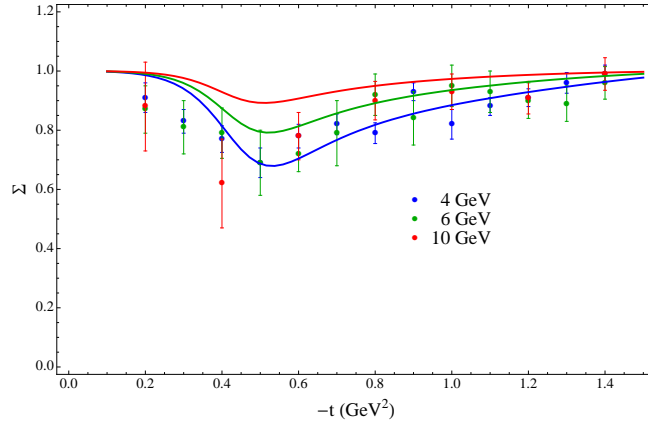


FIGURE 1.7: Prediction for the Beam Asymmetry from Mathieu, 2015.

$$\Sigma(s, t) = \frac{1}{P_\gamma} \frac{\frac{d\sigma_\perp}{dt} - \frac{d\sigma_\parallel}{dt}}{\frac{d\sigma_\perp}{dt} + \frac{d\sigma_\parallel}{dt}} = \frac{\sum_{\lambda_\gamma \lambda \lambda'} F_{\lambda_\gamma \lambda; \lambda'}(s, t) F_{-\lambda_\gamma \lambda; \lambda'}^*(s, t)}{\sum_{\lambda_\gamma \lambda \lambda'} |F_{\lambda_\gamma \lambda; \lambda'}(s, t)|^2}. \quad (1.18)$$

To how this is related to the naturality of the exchange, we rewrite the amplitude as a partial wave series in the t -channel, where the process is $\gamma\pi^0 \rightarrow p\bar{p}$,¹

$$F_{\lambda_\gamma \lambda; \lambda'}(s, t) = \sum_J (2J+1) A_{\lambda_\gamma; \lambda \lambda'}^J(t) d_{\lambda_\gamma, \lambda - \lambda'}^J(\theta_t), \quad (1.19)$$

with θ_t , the scattering angle in the t -channel. Parity conservation imposes the relation

$$A_{-\lambda_\gamma; \lambda \lambda'}^J(t) = -\eta A_{\lambda_\gamma; \lambda \lambda'}^J(t), \quad (1.20)$$

where η is the naturality of the exchange. At high energies and small t , $\cos \theta_t \propto s$ becomes very large and the rotation function obeys the relation

$$d_{-\lambda_\gamma, \lambda - \lambda'}^J(\theta_t) \simeq (-1)^{\lambda_\gamma} d_{\lambda_\gamma, \lambda - \lambda'}^J(\theta_t), \quad (1.21)$$

where the symbol \simeq means that the relation is valid only for the leading term in s .

Combining the results of Eqs. (1.20) and (1.21) we obtain the relations

$$F_{-\lambda_\gamma \lambda; \lambda'}(s, t) \simeq -\eta (-1)^{\lambda_\gamma} F_{\lambda_\gamma \lambda; \lambda'}(s, t) = \eta F_{\lambda_\gamma \lambda; \lambda'}(s, t), \quad (1.22)$$

as $\lambda_\gamma = \pm 1$. Plugging this into Eq. (1.18) one gets that $\Sigma \simeq \eta$ if a single exchange dominates. In general, the dominance of natural exchanges will result in $\Sigma \simeq 1$, while if unnatural dominate $\Sigma \simeq -1$. It is thus interesting to see what happens at the nonsense point $t = -0.5 \text{ GeV}^2$, where the leading vector exchange vanishes. If the subleading contribution is due to unnatural exchange, we expect the beam asymmetry to drop to negative values. If instead the dominant subleading contribution is a Regge cut, the beam asymmetry will stay close to one. The prediction from Mathieu, 2015, where a sizeable cut contribution is present, are shown in Fig. 1.7.

¹Technically, the helicities in the s - and t -channel are not the same, and additional Wigner rotations should be considered. However, since the proton helicities are summed over, and the photon helicity is frame independent, no difference occurs.

1.1.5 From Two-to-Three to Two-to-Two Scattering Process

Electron-Proton Scattering

Suppose that is interesting to determine a random charge distribution using electron scattering. The procedure, which derivation from Halzen and Martin, 1984 has been partially followed, is to measure the angular distribution of the scattered electrons and compare it to the cross section for scattering electrons from an equivalent point charge. Defining \mathbf{q} as the momentum transfer between the incident electron and the target ($\mathbf{q} = \mathbf{p}_i - \mathbf{p}_f$) and $F(\mathbf{q})$ as the *form factor*, which expresses the scattering amplitude of a wave by an isolated atom, we can express what said before as:

$$\frac{d\sigma}{d\Omega} = \left(\frac{d\sigma}{d\Omega} \right)_{point} |F(\mathbf{q})|^2. \quad (1.23)$$

It is possible to gain insight into the form factor by looking at the scattering of unpolarized electrons of energy E from a static, spinless charge distribution $Ze\rho(\mathbf{x})$, where

$$\int \rho(\mathbf{x}) d^3x = 1.$$

It is known that, for a static target, it is possible to obtain the requested information as both the form factor (expressed in terms of Fourier transform of the charge distribution) and cross section are known and written as follows:

$$F(\mathbf{q}) = \int \rho(\mathbf{x}) e^{i\mathbf{q}\cdot\mathbf{x}} d^3x, \quad (1.24)$$

$$\left(\frac{d\sigma}{d\Omega} \right)_{point} \equiv \left(\frac{d\sigma}{d\Omega} \right)_{Mott} = \frac{(Z\alpha)^2 E^2}{4p^4 \sin^4 \frac{\theta}{2}} \left(1 - v^2 \sin^2 \frac{\theta}{2} \right), \quad (1.25)$$

where $p = |\mathbf{p}_i| = |\mathbf{p}_f|$, $v = p/E$ and θ is the angle through which the electron is scattered.

The previous equation still cannot describe, though, the electron-proton scattering, since the structure of the proton is strongly different from a random charge distribution. The electric charge of the proton it's not the only quantity that has to be taken into account in this derivation: its magnetic moment is also involved in the scattering of the electron. Also, the proton is not static, but it will recoil under the electron's impact.

Suppose that, however, the proton is a point charge e with a Dirac magnetic moment $e/2M$. In this condition, the electron-muon scattering cross section can be used, replacing the mass of the muon with the proton one.

$$\left(\frac{d\sigma}{d\Omega} \right)_{lab} = \left(\frac{\alpha^2}{4E^2 \sin^4 \frac{\theta}{2}} \right) \frac{E'}{E} \left\{ \cos^2 \frac{\theta}{2} - \frac{q^2}{2M^2} \sin^2 \frac{\theta}{2} \right\} \quad (1.26)$$

Please note that the factor E/E' , which is tied to the recoil of the target, can be expressed also as follows:

$$\frac{E'}{E} = \frac{1}{1 + \frac{2E}{M} \sin^2 \frac{\theta}{2}}. \quad (1.27)$$

Process Factorization

Factorizing a 2-to-3 scattering reaction into a 1-to-2 and a subsequent 2-to-2 scattering reaction involves considering an interaction where the effects of the additional particle are incorporated into the properties of the two-particle system.

In order to do this, the Initial and Final States of the reaction have to be identified. For a better understanding of the process, the particle in the initial state will be e (beam electron) and p (target proton), while the ones in the final state will be e' (scattered electron), p (scattered proton), and π^0 (pion).

Specifically considering our reaction, the interaction between electron and proton is the core of the reaction. Since the electron does not interact strongly, the interaction can only be mediated by electromagnetic forces. At leading order in QED, this happens through an intermediate virtual photon γ_* . With this assumption, it is thus possible to factorize the pion electroproduction into a reaction $\gamma_* + p \rightarrow p' + \pi^0$. We remark that a virtual photon can also carry longitudinal polarization, $\lambda_\gamma = 0$. We follow the description in Bedlinskiy et al., 2014. The kinematic variables of the process

$$e(k) + p(p) \rightarrow e'(k') + p'(p') + \pi^0(v)$$

are defined as follows. The four-momenta of the incident and outgoing electrons are denoted by k and k' and the four-momentum of the virtual photon q is defined as $q = k - k'$. In the laboratory system θ is the scattering angle between the incident and outgoing electrons, with energies E and E' , respectively. The photon virtuality, given by

$$Q^2 = -q^2 = -(k - k')^2 \approx 4 E E' \sin^2 \frac{\theta}{2} \quad (1.28)$$

is positive. The four-momenta of the incident and outgoing protons are denoted by p and p' . The energy of the virtual photon is

$$v = \frac{p \cdot q}{m_p} = E - E', \quad (1.29)$$

where m_p is the proton mass. The Bjorken scaling variable x_B is defined as

$$x_B = \frac{Q^2}{2p \cdot q} = \frac{Q^2}{2m_p v}. \quad (1.30)$$

The squared invariant mass of the photon-proton system is given by

$$s = W^2 = (p + q)^2 = m_p^2 + 2m_p v - Q^2 = m_p^2 + Q^2 \left(\frac{1}{x_B} - 1 \right). \quad (1.31)$$

The momentum transfer t to the proton is defined by the relation

$$t = (p - p')^2 = (q - p_\pi)^2, \quad (1.32)$$

where p_π is the four-momentum of the π^0 meson. The minimum momentum transfer for a given Q^2 and W (or x_B) is denoted by t_{\min} .

The angle ϕ_π between the leptonic and hadronic planes is defined according to the Trento convention Bacchetta et al., 2004 (see Fig. 1.8).

Under the single photon assumption, the differential cross section of the reaction $ep \rightarrow e'p'\pi^0$ for an unpolarized electron beam and proton target can be written as

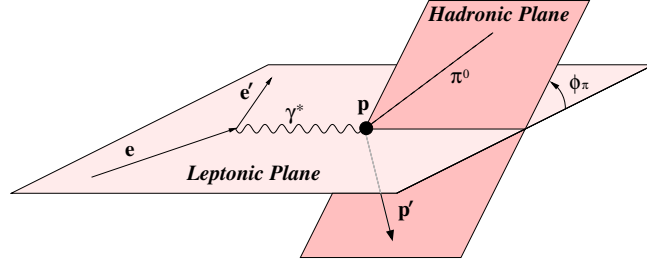


FIGURE 1.8: The kinematics of π^0 electroproduction. ϕ_π is the angle between the lepton and hadron planes. The lepton plane is defined by the incident and the scattered electron. The hadron plane is defined by the π^0 and the scattered proton. From Bedlinskiy et al., 2014.

Goloskokov and Kroll, 2010

$$\frac{d^4\sigma}{dQ^2 dx_B dt d\phi_\pi} = \Gamma(Q^2, x_B, E) \frac{1}{2\pi} \times \left[\left(\frac{d\sigma_T}{dt} + \epsilon \frac{d\sigma_L}{dt} \right) + \epsilon \cos 2\phi_\pi \frac{d\sigma_{TT}}{dt} + \sqrt{2\epsilon(1+\epsilon)} \cos \phi_\pi \frac{d\sigma_{LT}}{dt} \right], \quad (1.33)$$

where $\Gamma(Q^2, x_B, E)$ is the flux of transverse virtual photons and $\sigma_T, \sigma_L, \sigma_{TT}$ and σ_{LT} are the transverse, longitudinal, and asymmetric cross sections. They depend in general on the variables Q^2, x_B and t . We note that the dependence on x_B is a proxy for the dependence on the photon-proton CM energy, as shown in Eq. (1.31). The Hand convention Hand, 1963 was adopted for the definition of the virtual photon flux factor $\Gamma(Q^2, x_B, E)$:

$$\Gamma(Q^2, x_B, E) = \frac{\alpha}{8\pi} \frac{Q^2}{m_p^2 E^2} \frac{1-x_B}{x_B^3} \frac{1}{1-\epsilon}, \quad (1.34)$$

and α is the standard electromagnetic coupling constant. The variable ϵ represents the ratio of fluxes of longitudinally and transversely polarized virtual photons and is given by

$$\epsilon = \frac{1-y-\frac{Q^2}{4E^2}}{1-y+\frac{y^2}{2}+\frac{Q^2}{4E^2}}, \quad (1.35)$$

with $y = p \cdot q / q \cdot k = \nu / E$.

The reduced cross section is defined as

$$\frac{d^2\sigma}{dt d\phi_\pi} = \frac{1}{2\pi} \left[\left(\frac{d\sigma_T}{dt} + \epsilon \frac{d\sigma_L}{dt} \right) + \epsilon \cos 2\phi_\pi \frac{d\sigma_{TT}}{dt} + \sqrt{2\epsilon(1+\epsilon)} \cos \phi_\pi \frac{d\sigma_{LT}}{dt} \right]. \quad (1.36)$$

The cross section σ_L and σ_T involves longitudinally and transversely polarized photons, respectively:

$$\frac{d\sigma_L(s, t, Q^2)}{dt} = \frac{1}{2K} \sum_{\lambda\lambda'} |F_{0\lambda, \lambda'}(s, t, Q^2)|^2 \quad (1.37)$$

$$\frac{d\sigma_T(s, t, Q^2)}{dt} = \frac{1}{4K} \sum_{\lambda_\gamma=\pm 1} \sum_{\lambda\lambda'} |F_{\lambda_\gamma, \lambda, \lambda'}(s, t, Q^2)|^2, \quad (1.38)$$

where the quantity K is the phase space factor in the Hand convention, which depends on W^2 , Q^2 , m_p^2 and x_B .

$$\begin{aligned} K &= 16\pi \left(W^2 - m_p^2\right) \lambda^{1/2} \left(W^2, -Q^2, m^2\right) \\ &= 16\pi Q^4 \left(\frac{1}{x_B} - 1\right) \sqrt{\frac{1}{x_B^2} + \frac{4m_p^2}{Q^2}} \end{aligned} \quad (1.39)$$

However, here we are interested in the transverse-transverse interference cross section σ_{TT} ,

$$\frac{d\sigma_{TT}(s, t, Q^2)}{dt} = -\frac{1}{4K} \sum_{\lambda_\gamma = \pm 1} \sum_{\lambda\lambda'} F_{\lambda_\gamma\lambda,\lambda'}(s, t, Q^2) F_{-\lambda_\gamma\lambda,\lambda'}^*(s, t, Q^2). \quad (1.40)$$

One can recognize basically the same structure of the beam asymmetry for photoproduction as in Eq. (1.18). We are interested in the limit of quasi-real photoproduction, where $Q^2 \simeq 0$. In this case, one can neglect the contribution of longitudinal polarizations, as they decouple in the $Q^2 \rightarrow 0$ limit. The cross section of Eq. (1.36) reduces to

$$\frac{d^2\sigma}{dt d\phi_\pi} \simeq \frac{1}{2\pi} \left[\frac{d\sigma(s, t, Q^2)}{dt} + \epsilon \cos 2\phi_\pi \frac{d\sigma_{TT}}{dt} \right] = \frac{1}{2\pi} \frac{d\sigma_T}{dt} [1 - \epsilon \cos 2\phi_\pi \Sigma(s, t, Q^2)] \quad (1.41)$$

with the factor $\epsilon = \epsilon(s, Q^2, E)$ that plays the role of the degree of polarization P_γ . The function $\Sigma(s, t, Q^2)$ represents the beam asymmetry of a quasi-real photon with virtuality Q^2 . Although in this thesis we focus on the real photon limit, studying the dependence of the beam asymmetry with Q^2 allows to validate further the Regge cut model. In particular, in Collins and Wilkie, 1981 it is argued that Regge cuts and poles have different Q^2 dependences, that lead to filling the dip in the differential cross section already at moderate Q^2 . Measuring Σ in bins of Q^2 will allow us to validate whether the subleading contribution at $t = -0.5 \text{ GeV}^2$ is indeed saturated by a Regge cut, as suggested in Mathieu, 2015.

1.2 Previous Results

As said before, comparing CLAS12 Beam Asymmetry results with what has been found in SLAC (Anderson et al., 1971) and GlueX (Al Ghoul et al., 2017) is the main focus of this thesis. The two aforementioned experiments will be later briefly explained for the sake of clarity. From Fig. 1.9 it is interesting to see a marginal disagreement in the region of the nonsense point $t = -0.5 \text{ GeV}^2$, which calls for an independent measurement that is the subject of this thesis.

1.2.1 SLAC

Stanford Linear Accelerator Center (SLAC), then renamed to SLAC National Accelerator Laboratory, is a research facility located in California and operated by Stanford University.

SLAC is known for its state-of-the-art particle accelerators and detectors, which have been used to conduct fundamental experiments for the understanding of nuclear matter. One of the notable detectors at SLAC is BaBar, which collected data from 1999 to 2008 and made significant contributions to the field of flavor physics.

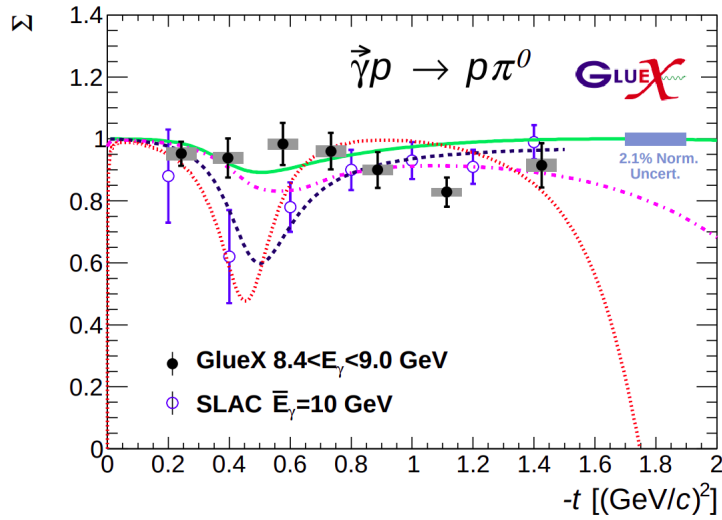


FIGURE 1.9: Beam Asymmetry for $\gamma + p \rightarrow p + \pi^0$ measured by SLAC and GlueX experiments. Comparison with models and theory. Figure from Al Ghoul et al., 2017.

Other notable facilities at SLAC are the Linac Coherent Light Source (LCLS), and the Large Synoptic Survey Telescope (LSST) Camera Integration and Testing Facility. In addition to these, SLAC is involved in various collaborative research projects with institutions and organizations worldwide and is deeply involved in the upgrade of accelerator science, particle physics, and related fields.

The study of photoproduction at high energies and small momentum transfers at SLAC has been carried out through precise measurements of the cross-section and asymmetry using polarized photons, the experiment observed a distinct dip in the differential cross-section at $t = -0.5 \text{ GeV}^2$ Anderson et al., 1971. This dip persisted across different incident energies, challenging the naïve Regge model's interpretation.

The analysis revealed that the dip's behavior with increasing photon energy differed from what was initially expected based on the sum of Compton scattering and photoproduction cross-sections. This discrepancy highlighted the strong dependence of the cross-section in the dip region on the applied Compton correction, leading to uncertainties in the measured values.

To overcome these challenges, the experiment adopted an updated approach. The earlier data were reevaluated, incorporating the now-known Compton cross-section for improved accuracy. Furthermore, additional measurements were performed at higher incident photon energies to extend the energy range covered by the experiment. Coincidence measurements in the critical region around $t = -0.5 \text{ GeV}^2$ provided valuable insights, validating the dip observed at lower energies.

The results obtained from the SLAC experiment challenged the conventional Regge model's ability to explain the observed data. It became clear that absorption effects needed to be considered or modifications to the trajectory and residue functions associated with p and w exchange were required. Models incorporating absorption or cuts were found to better fit the experimental findings.

1.2.2 GlueX

GlueX experiment, set at Jefferson Laboratory in Virginia, has been designed to study photoproduction reactions with a 9-GeV linearly polarized photon beam.

The energy and arrival time of beam photons are tagged using a scintillator hodoscope and a scintillating fiber array. The photon flux is determined using a pair spectrometer, while the linear polarization of the photon beam is determined using a polarimeter based on triplet photoproduction. Charged-particle tracks from interactions in the central target are analyzed in a solenoidal field using a central straw-tube drift chamber and six packages of planar chambers with cathode strips and drift wires.

Electromagnetic showers are reconstructed in a cylindrical scintillating fiber calorimeter inside the magnet and a lead-glass array downstream. Charged particle identification is achieved by measuring energy loss in the wire chambers and using the flight time of particles between the target and detectors outside the magnet.

The signals from all detectors are recorded with flash ADCs and/or pipeline TDCs into memories allowing trigger decisions with a latency of $3.3\mu\text{s}$. The detector operates routinely at trigger rates of 40 kHz and data rates of 600 megabytes per second.

The photon beam, the GlueX detector components, electronics, data-acquisition and monitoring systems, and the performance of the experiment during the first three years of operation are deeply described in Al Ghoul, 2021.

As the two main experiment previously involved in the work treated in this thesis has been explained, it's fundamental to focus on Fig. 1.9, where the models by Goldstein and Owens, 1973 (red dotted) and Donnachie and Kalashnikova, 2016 (black dashed) are shown and suggest the presence of a dip in beam asymmetry due to subleading unnatural exchanges and which seems to be seen in SLAC data (Anderson et al., 1971). Conversely, the models by Laget, 2011 (pink dash-dotted) and Mathieu, 2015 (solid green) fill the dip with Regge cuts, and favor a constant beam asymmetry $\Sigma \simeq 1$, which seems backed up by new GlueX data of Al Ghoul et al., 2017.

Chapter 2

Experimental Setup

In this chapter, CLAS12 and Jefferson's Laboratory facility detectors and setups will be analyzed in detail. The chapter will start with an overview of the facility, diving then into a full description of the CLAS12 spectrometer, going into the detail of the two detector blocks and their components. In the last section, a deep description of the Forward Tagger detector will be reported. Please note that some of the data and information about the composition and setup of the facility and detectors are extracted from Burkert et al., 2020 and Acker et al., 2020a.

2.1 Facility

The CEBAF accelerator, shown along the experimental halls in Fig.[2.1], is designed from two parallel linear accelerators (*LINACs*) based on superconducting radio frequency (*RF*) technology, and arranged in a race track configuration (Leemann, Douglas, and Krafft, 2001). Spin-polarized electrons are generated in the gun and then are pre-accelerated in the injector. They are then injected and accelerated in the north LINAC.

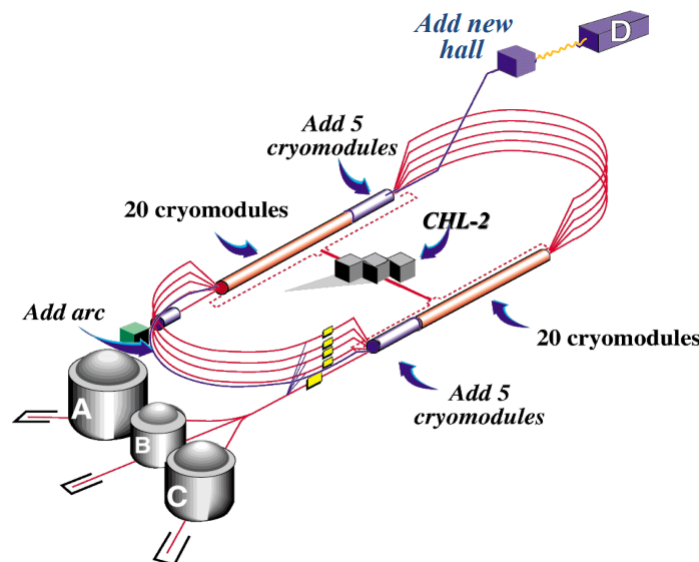


FIGURE 2.1: CEBAF continuous electron beam accelerator at 12 GeV. Note the adding of the new experimental end station (Hall D) for photon physics experiments. The accelerator is 1400 m in circumference.

Burkert et al., 2020.

Electrons are then bent in a 180° arc and injected into the second LINAC. This cycle can repeat four and a half more times, reaching the required energy for Hall D, or up to four times, for any value of energy requested by Halls A, B, and C.

In the recirculating arcs, electrons are transported in 5 independent out-of-phase tracks that transport the electron at different energies to the Halls. Five accelerating cryomodules machines were added to each of the two existing LINACs to reach a maximum energy of 11 GeV for Halls A, B, and C, and 12 GeV for Hall D. For the latter, which is the only Hall capable of receiving such energy, one additional arc path and one more pass through the north LINAC were added. The other three halls can also simultaneously receive beams at different beam energies, with a difference in current that goes from 1 nA to $100 \mu\text{A}$.

All the Halls have been equipped with new detectors and other experimental instruments, in support to a broad science program focused on nuclear and hadronic physics.

In Hall D, a large hermetic detector with a solenoid magnet at its core has been working since 2015 and incorporates tracking capabilities and photon detection over nearly the full 4π solid angle.

The new CLAS12 spectrometer is located in Hall B, and will be analyzed deeply in the following section.

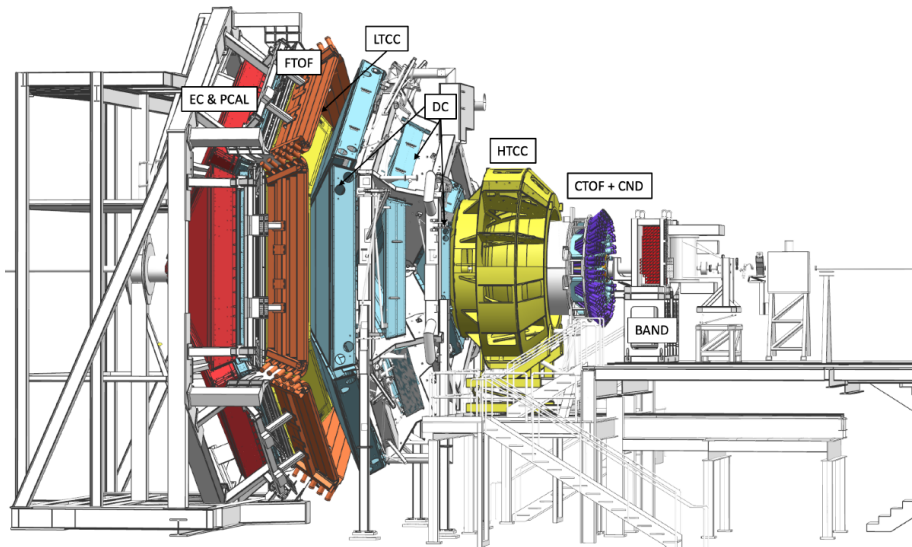


FIGURE 2.2: The CLAS12 detector in the Hall B beamline. The electron beam enters from the right and impinges on the production target located in the center of the solenoid magnet shown at the right (upstream) end of CLAS12, where other detector components are also visible. Scattered electrons and forward-going particles are detected in the Forward Detector (FD) consisting of the High Threshold Cherenkov Counter (HTCC) (yellow) with full coverage in polar angle $5^\circ \leq \theta \leq 35^\circ$ and $\Delta\phi = 2\pi$ coverage in azimuth. The HTCC is followed by the torus magnet (gray), the drift chamber tracking system (light blue), another set of Cherenkov counters (hidden), time-of-flight scintillation counters (brown), and electromagnetic calorimeters (red). Between the HTCC and the torus, the FT is installed to detect electrons and photons at polar angles $2^\circ \leq \theta \leq 5^\circ$. The Central Detector (CD) consists of the Silicon Vertex Tracker (hidden), which is surrounded by a Barrel Micromesh Tracker (hidden), the Central Time-of-Flight system, and the Central Neutron Detector (PMTs in blue). At the upstream end, a Back Angle Neutron Detector (red) is installed. In the operational configuration, the entire CLAS12 detector extends for 13 m along the beamline.

Burkert et al., 2020.

Hall C, in addition to the existing high momentum spectrometer, includes the new super-high momentum magnetic spectrometer (SHMS).

In Hall A, on top of the existing high-resolution spectrometer pair HRS2, a new super big bite spectrometer (SBS) has been added.

Along with the new equipment, we can add highly spin-polarized electron gun, high-power cryogenic targets, and several spinpolarized targets using NH_3 , ND_3 , HD , 3He , and 7Li as target materials to support a huge range of polarization measurements.

2.1.1 Hall B Beamline

The two sections of the Hall B beamline, 2C and 2H line, run from and to different points; while the first one starts at the Beam Switch Yard (BSY) and ends at the Hall proper, the latter run from the upstream end of the experimental Hall to Faraday Cup (also called Beam Dump) in the downstream tunnel, as seen by the portions shown in Fig.[2.3].

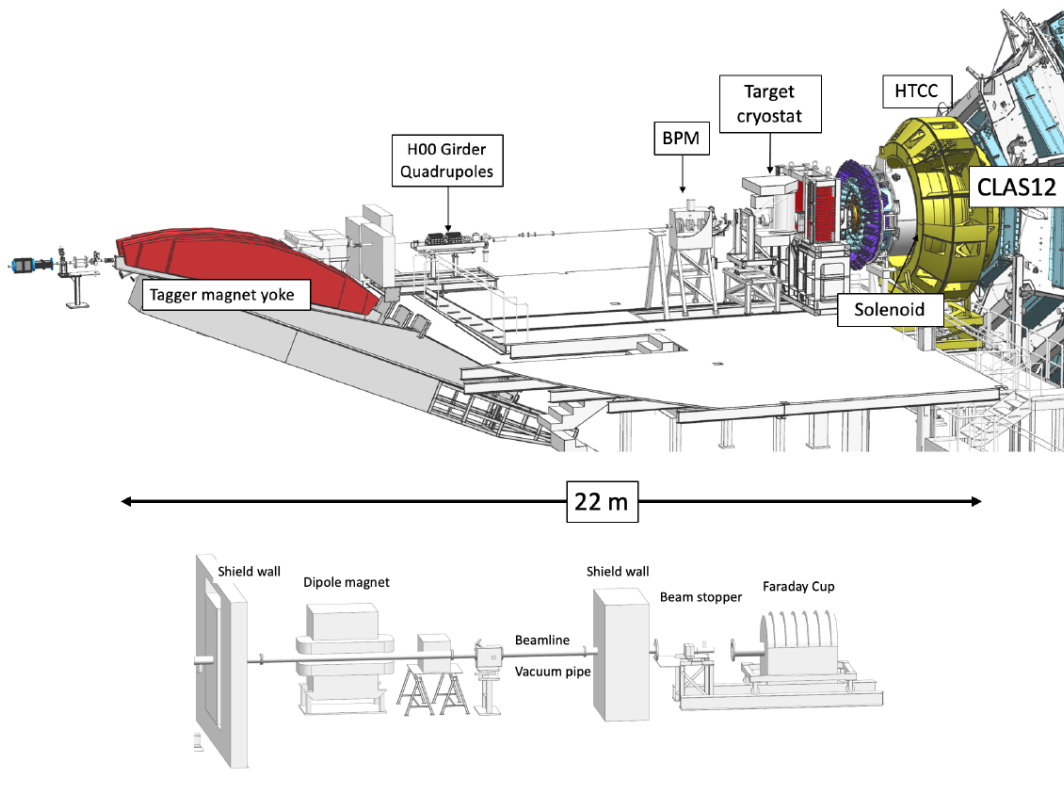


FIGURE 2.3: Top: Hall B beamline upstream of the target, showing the tagger magnet (red) to the left, which is energized during beam tuning and during polarization measurements. The doublet seen downstream of the tagger is a pair of quadrupoles. The beam position monitors (BPMs) are used for beam position and beam current measurements. The main element on the right is the solenoid magnet nearly fully encapsulated by the HTCC (yellow). Several of the torus magnet coils are visible at the far right. Bottom: The part of the beamline that extends from the downstream end of CLAS12 to the Faraday cup, a total absorbing device that is used to integrate the beam current to get the total accumulated charge.

Burkert et al., 2020.

Beam optics, collimators, shielding, profile scanner, and halo monitors, along with the beam position and current monitors compose the beamline instrumentation.

The accelerator operations control reports the beam direction, its profile, and other critical parameters, while Hall B operators control collimators, halo monitors, profile scanners, and viewers. The operators are also responsible for the configuration and activation of the Møller polarimeter located upstream of the tagger magnet. For details of the beamline elements and beam quality, see Baltzell, 2020.

The performance of the electron beam along with all diagnostic elements in the beamline like the status of the beamline vacuum, the rates in all detector systems, and the superconducting magnets; all the other indicators of potential beam quality issues are also directly displayed on a single master screen that is accessible to the shift personnel and other experiment-related experts.

2.2 CLAS12

Hall B at Jefferson Laboratory hosts the CEBAF Large Acceptance Spectrometer for operation at 12 GeV beam energy (CLAS12, displayed in Fig.[2.2] and in Fig.[2.4]), which is used to study electro-induced nuclear and hadronic reactions. As mentioned before, this spectrometer provides the efficiency in detection needed for meson spectroscopy analysis. It can detect charged and neutral particles over most of the full solid angle.

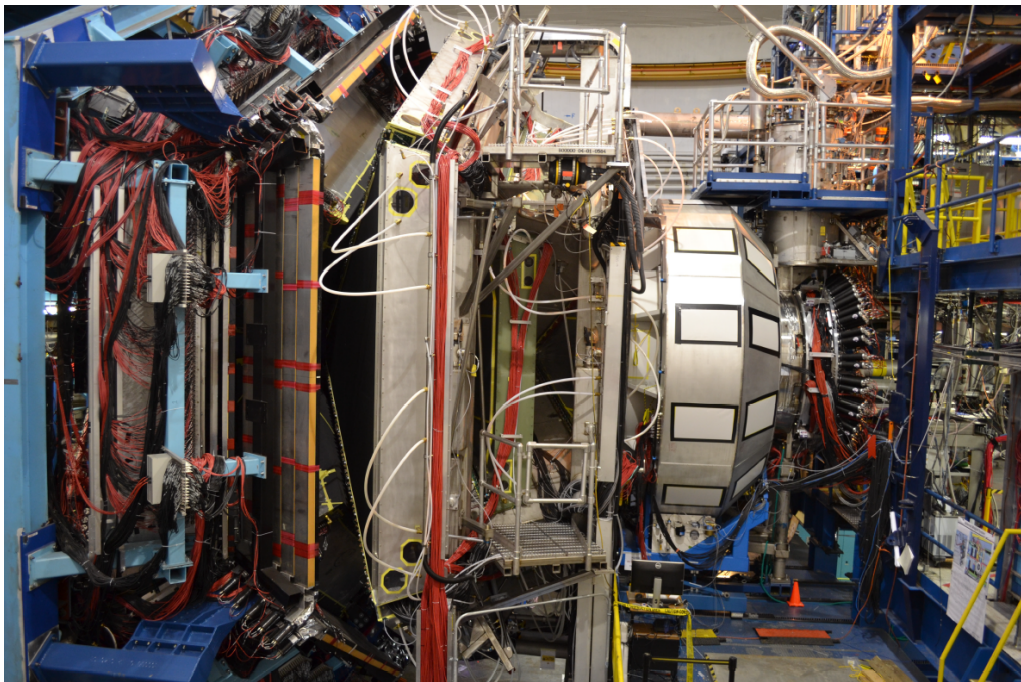


FIGURE 2.4: The CLAS12 detector in the Hall B beamline. The beam enters from the right near the upstream end of the solenoid magnet and the cryogenic service tower, followed by the HTCC and the torus magnet with the drift chambers. The Low Threshold Cherenkov Counter, Forward Time-of-Flight, and electromagnetic calorimeters (PCAL and EC) are seen at the downstream end to the left.

Burkert et al., 2020.

CLAS12, being part of the energy-doubling project of Jefferson Lab's Continuous Electron Beam Accelerator Facility, was funded by the United States Department of Energy, while over 40 international institutions contributed to the design and construction of its hardware and developed the software packages for the complex events simulation.

Based on a dual-magnet system, CLAS12 uses a superconducting torus magnet that provides a largely azimuthal field distribution (forward polar angle range up to 35°), and a solenoid magnet and detector with full azimuthal coverage and extends the detection polar angle from 35° to 125° . A momentum resolution of $< 1\%$ and $< 3\%$ is achieved respectively for trajectory reconstruction results using drift chambers, for the forward direction, and vertex tracker, for the central direction. Good particle identification is achieved thanks to Cherenkov counters, time-of-flight scintillators, and electromagnetic calorimeters. Fast triggering and high data-acquisition rates allow operation at a luminosity of $10^{35} \text{ cm}^{-2} \text{ s}^{-1}$.

This section gives a general description of the design, construction, and performance of CLAS12.



FIGURE 2.5: The CLAS12 magnet systems. Left: The fully assembled solenoid magnet including all cryogenic connections on the beamline at the beginning of cool down, before the detector installation. Right: The torus magnet with all six coils mechanically assembled in a common cryostat. The coil cryostat, which is fabricated from non-magnetic steel, has an outside width of 124 mm. The cross bars provide a cold (4.5 K) cryogenic connection of neighboring coils and counteract the out-of-plane forces to provide mechanical stability to the full magnet. Due to the large physical size of the assembled torus magnet, the final assembly of the magnet had to be completed in Hall B.

Burkert et al., 2020.

2.2.1 Superconductive Magnets

A combination of toroidal and solenoidal magnetic fields build the base of the CLAS12 design: the first one is located at polar angles up to $\approx 35^\circ$, while the second one, with an intensity of $5 T$, covers the central region in the approximate polar angle range of $35^\circ \leq \theta \leq 125^\circ$.

The need to operate a high luminosity for the detector system and still measure charged particles at high momentum with good resolution at forward angles requires an effective shielding of the detector system, and thus the combination of the magnets. This is fundamental because low-energy electrons are produced in the target material due to Møller scattering ($e^- + e^- \rightarrow e^- + e^-$) of the high-energy beam electrons on atomic electrons in the target material. Most part of those electrons curl up in the strong magnetic field and are prevented from reaching the detectors, and are then guided into a bulk tungsten shielding pipe, where they dump their energy.

The fully assembled torus and solenoid magnets are shown in Fig.[2.5].

The Torus Magnet

The symmetrically arranged six magnet coils provide an approximate toroidal magnetic field around the beamline, from 5° to 40° in polar angle (as seen from the target). The six coils are mounted on a common stainless-steel cylinder, which also provides the geometrical symmetry for the alignment of the coils near the magnet center, and inside a central cold hub. This kind of arrangement grants a high placement accuracy of the coil packages in areas where the magnetic field is expected to be at its peak. The open range in azimuthal angle depends on the polar angle of the particle trajectory and ranges from 50% of 2π at 5° to about 90% of 2π at 40° .

Each superconducting coil is made from a two-coil "double-pancake" potted in an aluminum case. The number of windings per pancake is 117. The conductor is a Superconducting Super Collider outer dipole cable soldered into a $20 \text{ mm} \times 2.5 \text{ mm}$ copper channel with turn-to-turn insulation of $75 \mu\text{m}$ fiberglass tape. Operating at a nominal current of $3770 A$, the peak field is $3.58 T$ at the inner turns close to the warm bore.

For symmetry reasons, the field on the beam axis is ideally equal to zero, with a small remnant field present due to imperfections in the magnet assembly and coil positions. The $\int Bdl$ at the nominal current is $2.78 Tm$ at 5° and $0.54 Tm$ at 40° . The inductance of the magnet is $2.0 H$ and the stored energy $14.2 MJ$.

The magnet has liquid- N_2 cooled heat shields. After assembly and cooling down, the magnet reached full field immediately.

For details on the design and operation of the torus magnet, see Fair et al., 2020.

The Solenoid Magnet

Used to generate a field primarily in the beam direction, the solenoid magnet is a self-shielded superconducting magnet that surrounds the beamline.

The nominal field in the center of the magnet is $5 T$. The design is driven by the physics requirements to provide a magnetic field for particle tracking at large angles, act as an Møller electron shield, and provide a highly uniform field at the magnet center for the operation of dynamically polarized proton and deuteron targets.

The magnet consists of four cylindrical coils arranged in two packages at different radial distances to the beamline. A fifth coil is located outside of the 4 inner coils and generates a magnetic field in the opposite direction of the field of the four inner

coils and thus acts as an active magnetic shield. The number of turns in the main coils is 3704 ($2 \times 840 + 2 \times 1012$) and in the shield coil is 1392.

The magnet is powered at a nominal current of 2416 A. At full current, the solenoid generates a 5 T magnetic field at its center. The integrated field length along the magnet center is $\int Bdl = 7.0 Tm$, generating a stored energy of 20 MJ. The magnet has an inner warm bore of 78 cm diameter where all of the central detectors are placed.

For details on the design and operation of the solenoid magnet, see Fair et al., 2020.

2.2.2 Forward Detector

Drift Chamber (DC)

The forward tracking system, which is formed by three independent DCs, is mechanically supported by the aforementioned six coils of the torus magnet. This kind of setup divided the chamber into six different sectors; each of these has a total of 36 layers with 112 sense wires, arranged in 3 chambers (R1, R2, and R3) of 12 layers each. Note that every region is arranged identically to the others.

As displayed in Fig.[2.6], R1, R2, and R3 chambers are located in regions with different magnetic field intensities: while the R1 is located at the entrance, the R2 chambers are located at the magnetic field peak, and the R3 chambers are placed in a low magnetic field space downstream of the torus.

Each of the 3 regions consists of two superlayers, each one formed of 6 single layers; the first of the two superlayers has wires strung at a stereo angle of $+6^\circ$ with respect to the sector midplane while the second has them at an angle of -6° with respect to the sector midplane. This stereo view enables excellent resolution in the most important polar angle (laboratory scattering angle), and good resolution in the less critical azimuthal scattering angle.

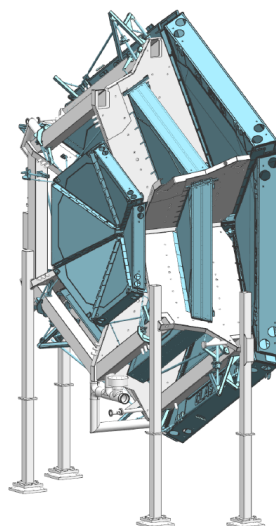


FIGURE 2.6: Drift chamber system in the CLAS12 forward tracking system from the design model. The small-size R1 chambers are located just in front of the torus magnet coils (gray shade). The medium-size R2 chambers are sandwiched between the coils of the magnet, and the large-size R3 chambers are located just downstream of the magnet
Burkert et al., 2020.

For details of the DC construction and performance, see Mestayer, 2020.

High Threshold Cherenkov Counter (HTCC)

The main detector with the role of separate electrons (positrons) with momenta below 4.9 GeV from charged pions, protons, and kaons is the HTCC. This detector has a full coverage of 360° in azimuth and spans from 5° to 35° in polar angle. The detector is located between the solenoid magnet and the torus magnet, downstream of the production target, positioned in front of the FT detector.

The detector provides high rejection of low background noise and charged pions for reliable identification of scattered electrons in a dense electromagnetic background environment.

The HTCC is a single unit operated in dry CO_2 gas at 1 atm pressure. It is constructed using a multi-focal mirror of 48 elliptical mirror facets that focuses the Cherenkov light on 48 photomultiplier tubes (PMTs) with quartz windows of 125 mm diameter. The PMTs are located in a magnetic field of up to 35 G oriented along the phototube axes and are surrounded along their lengths by a multi-layer magnetic shield with active compensation coils.

The HTCC mirror system is constructed using a backing structure of low-density composite material, in order to minimize multiple scattering inside the detector without limiting its resolution. All the materials but the radiator gas in the path of the charged particles had to be kept to a minimum, as the HTCC is located in front of the momentum analyzer. In the actual detector, the density of the solid material seen by charged particles passing through the HTCC volume is 135 mg/cm^2 .

HTCC, operating along with the electromagnetic calorimeters, can also generate a fast signal to be used as a trigger for scattered electrons. Fig.[2.7] shows a cut view of the assembled HTCC detector.

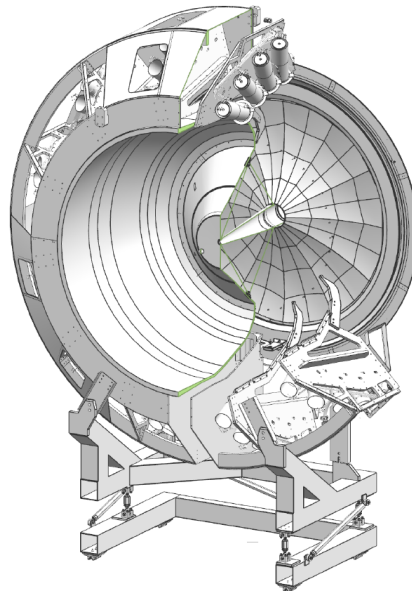


FIGURE 2.7: Cut view of the assembled HTCC detector. The container spans a diameter of about 4.5 m. The mirror is seen at the downstream end to the right. The PMTs are mounted in 12 sectors and in groups of 4 at the outer perimeter of the container. The light collection uses additional Winston cones and PMTs with quartz windows.

Burkert et al., 2020.

For details of the HTCC construction and performance, see Sharabian, 2020.

Low Threshold Cherenkov Counter (LTCC)

The LTCC system is used, at momenta greater than 3.5 GeV , for charged pion detection and consists of boxes shaped like truncated pyramids. Only four of the six sectors of CLAS12 are equipped with one LTCC box, which contains 108 lightweight mirrors with composite backing structures, 36 Winston light-collecting cones, 3 125 mm diameter PMTs, and 36 magnetic shields. The LTCC boxes are filled with heavy C_4F_{10} radiator gas.

The LTCC system has previously been used in the previous CLAS detector, at lower energies, as an electron detector. It has been refurbished (increase of the volume of the radiator gas, new coatings of the mirrors, and the PMT entrance windows) in order to provide higher efficiency for charged pion detection. The components of the LTCC optical mirror system and its arrangement are shown in Fig.[2.8].

For details of the LTCC construction and performance, see Ref. Ungaro, 2020b.

Ring Imaging Cherenkov Detector (RICH)

In some situations, the detection and identification of charged kaons in peculiar momentum ranges is required. These momenta are not accessible with the standard Forward Time-of-Flight system or with the LTCC, having not enough resolution to separate kaons from pions for momenta greater than 3 GeV . For that purpose, an additional detector, called RICH, was built and incorporated into one of the CLAS12 sectors to replace the corresponding LTCC sector.

The RICH detector is designed to work in the momentum range $3 - 8 \text{ GeV}$, improving CLAS12 particle identification. It incorporates aerogel radiators, visible

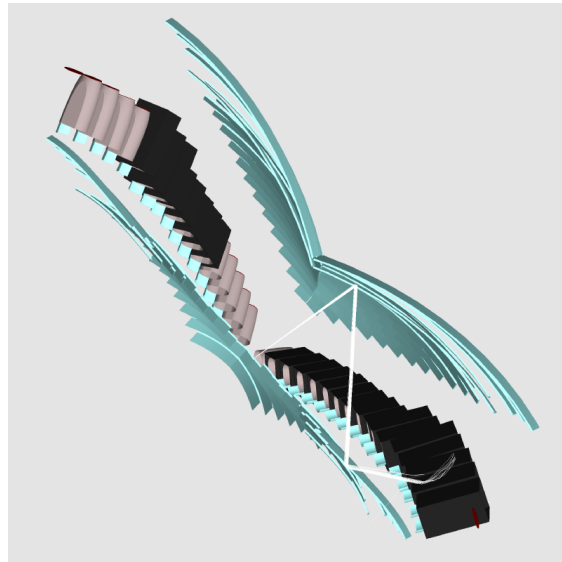


FIGURE 2.8: Perspective representation of the LTCC optical system. A charged particle enters from the bottom left and generates Cherenkov light in the radiator gas volume. The light is reflected off the elliptical mirror array towards the hyperbolic mirror array, from where it is reflected towards the Winston cone and PMT. The large acceptance coverage requires a complex mirror system for efficient light collection.

Burkert et al., 2020.

light photon detectors, and a focusing mirror system that is used to reduce the detection area instrumented by photon detectors to 1 m^2 . Multi-anode photomultiplier tubes (MaPMTs) provide the required spatial resolution and match the aerogel Cherenkov light spectrum in the visible and near-UV region.

For forward scattered particles ($\theta \leq 13^\circ$) with momenta $3 - 8\text{ GeV}$, a proximity imaging method with thin (2 cm) aerogel and direct Cherenkov light detection is used. For larger incident particle angles of $13^\circ \leq \theta \leq 25^\circ$ and momenta of $3 - 6\text{ GeV}$, the Cherenkov light is produced by a thicker aerogel layer of 6 cm , focused by a spherical mirror, and undergoes two further passes through the thin radiator material and a reflection from planar mirrors before detection. Fig.[2.9] shows the RICH mirror system.

For further details of the RICH detector construction and performance see Con- talbrigo et al., 2020.

Forward Time-of-Flight (FTOF)

Often charged particles emerge from the production target during beam operation; the measure of the time-of-flight of this particle is the task of the FTOF detector.

The FTOF includes six sectors of plastic scintillators with double-sided PMT read-out. Each sector is composed of three arrays of counters (panel-1a: 23 counters; panel-1b: 62 counters; panel-2: 5 counters). Excellent timing resolution for particle identification and good segmentation for flexible triggering options is mandatory in this kind of analysis, making the FTOF a crucial component of the CLAS12 detector.

The detectors span a range in polar angle from 5° to 45° , covering 50% in ϕ at 5° and 90% at 45° . The lengths of the counters range from 32.3 cm to 376.1 cm in panel-1a, from 17.3 cm to 407.9 cm in panel-1b, and from 371.3 cm to 426.2 cm in panel-2. The average timing resolution in panel-1a is 125 ps , 85 ps in panel-1b, and 155 ps in panel-2.

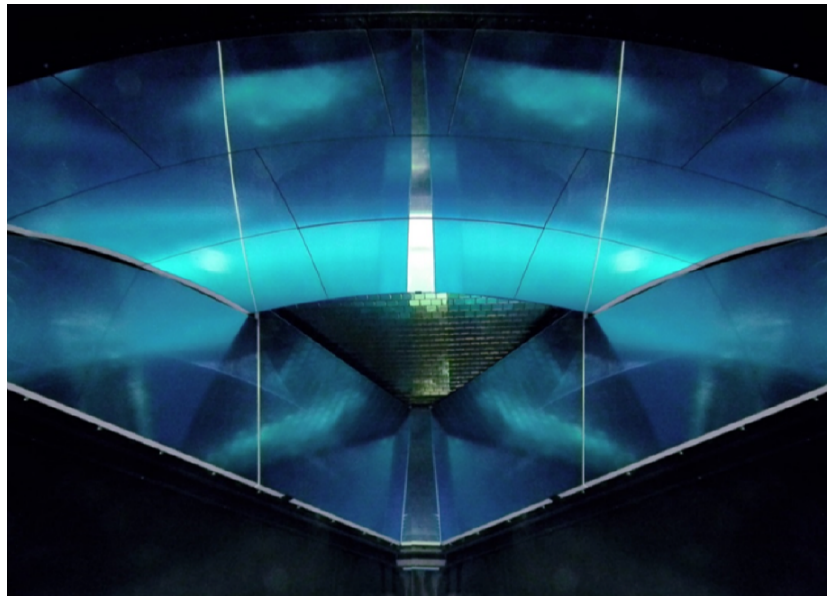


FIGURE 2.9: The RICH mirror system is shown here in a perspective view as seen from the entrance window, with the spherical mirrors above, and the planar mirrors below. The detector array with the MaPMTs is seen in the center. The aerogel radiator is not shown.

Burkert et al., 2020.

The left side of Fig.[2.10] show the FTOF system on the Forward Carriage. For details of the FTOF construction and performance, see Carman, 2020b.

Electromagnetic Calorimeters (ECAL)

The already existing electromagnetic calorimeter (EC) from the CLAS detector, along with a new pre-shower calorimeter (PCAL) installed in front of the aforementioned EC are referred to as the ECAL.

In CLAS12, the identification and kinematical reconstruction of electrons, photons (e.g. from $\pi^0 \rightarrow \gamma\gamma$ and $\eta \rightarrow \gamma\gamma$ decays), and neutrons is a task primarily given to the calorimeters.

The PCAL and EC are both sampling calorimeters consisting of six modules. Along the direction from the target, the EC consists of two parts, read out separately, called EC-inner and EC-outer. They provide a longitudinal sampling of electromagnetic showers, as well as of hadronic interactions to improve particle identification.

Each module has a triangular shape with 54 (15/15/24, PCAL/EC-inner/EC-outer) layers of 1 cm-thick scintillators segmented into 4.5/10 cm (PCAL/EC) wide strips sandwiched between 2.2 mm-thick lead sheets. The total thickness corresponds to approximately 20.5 radiation lengths.

Scintillator layers are grouped into three readout views with 5/5/8 PCAL/EC-inner/EC-outer layers per view, providing spatial resolutions of less than 2 cm for energy clusters. The light from each scintillator readout group is routed to the PMTs via flexible optical fibers.

The right side of Fig.[2.10] shows the PCAL after installation on the Forward Carriage in front of the existing EC from CLAS.

For information about the EC, see Amarian et al., 2001. For details of the construction of the PCAL and the performance of the ECAL, see Asryan, 2020.

Forward Tagger (FT)

The Forward Tagger (FT) extends the capabilities of CLAS12 to detect electrons and photons at very forward polar angles in the range from $2.5^\circ \leq \theta \leq 4.5^\circ$. Being

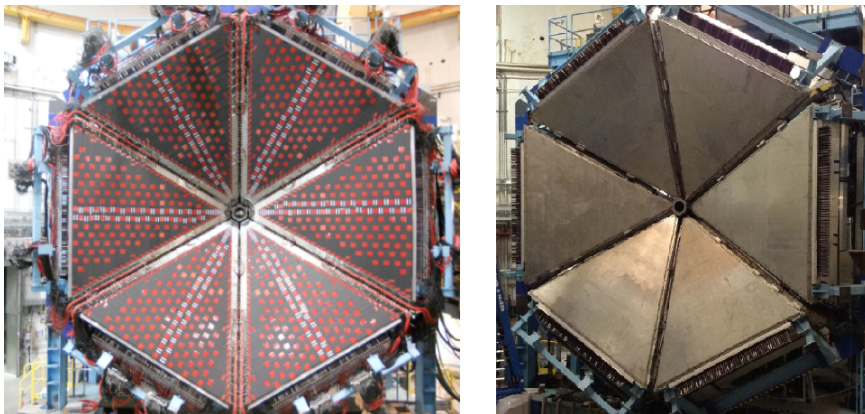


FIGURE 2.10: Left: Photograph of the FTOF panel-1b counters mounted on the CLAS12 Forward Carriage in front of the panel-1a counters and the electromagnetic calorimeters before the installation of the panel-2 counters. Right: PCAL after installation on the Forward Carriage in front of the existing EC.

Burkert et al., 2020.

fundamental in the analysis carried on in this thesis, this detector will be detailed in the following section.

2.2.3 Central Detector

The Central Detector is focused on the detection of particles scattered from the target at polar angles in the range from 35° to 125° . This device has its own particle identification and tracking detectors.

The Central Vertex Tracker (CVT) tracks the charged particles, which are then detected in the full 360° azimuthal coverage Central Time-of-Flight (CTOF) detector. Located radially outside of the CVT and the CTOF, the Central Neutron Detector (CND) provides the detection of neutral particles.

Fig.[2.11] shows the Central Detector from the upstream end.

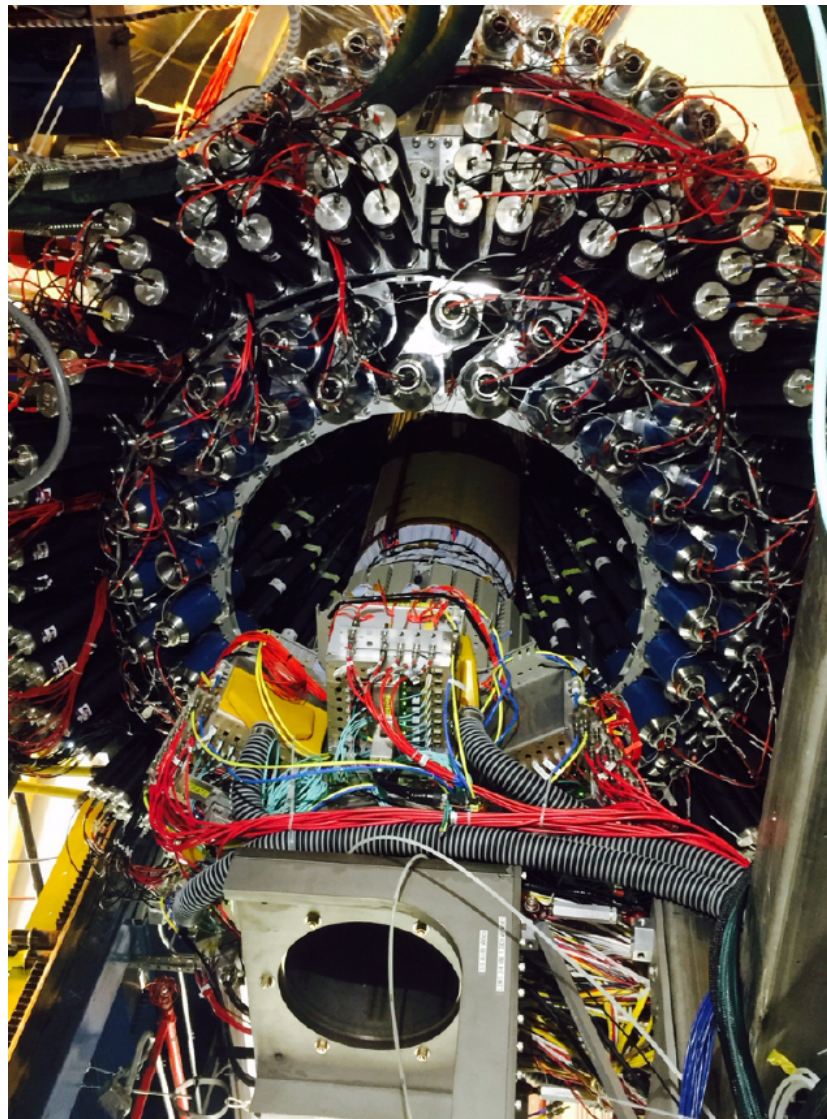


FIGURE 2.11: The Central Detector seen from the upstream end. The central tracker system is shown in a retracted position for maintenance. During operation, it is fully inserted into the warm bore of the magnet.

Burkert et al., 2020.

Central Vertex Tracker (CVT)

Part of the Central Detector, the CVT is used to measure momenta of charged particles, aiming also to the determination of the vertex for the products of the scattering on the production target. It consists of two separate detectors, a Silicon Vertex Tracker (SVT) and a Barrel Micromegas Tracker (BMT).

The SVT system includes three regions with 10, 14, and 18 double-sided modules of silicon sensors instrumented with the digital readout ASIC Fermi-lab Silicon Strip Readout (FSSR2). The readout pitch is $156\ \mu\text{m}$, and the total number of channels is 21504.

The BMT contains three layers of strips along the beamline and three layers of circular readout strips around the beamline, with a total number of 15000 read-out elements. The BMT provides important improvements in momentum resolution and in tracking efficiency. Each layer is arranged azimuthally in three segments of 120° azimuthal coverage each. The system operates at the full design luminosity of $10^{35}\ \text{cm}^{-2}\ \text{s}^{-1}$.

Another component of the CVT is the Forward Micromegas Tracker (FMT), consisting of six layers with 6000 readout elements. It is integrated mechanically with the CVT to provide a compact tracking system but covers the polar angle range from 5° to 35° and provides improved vertex reconstruction for forward-scattered charged particles.

The fully assembled CVT is shown in Fig.[2.12].

See Antonioli, 2020 for more information on the SVT, and Acker et al., 2020b for details on the design, construction, and performance of BMT and FMT.

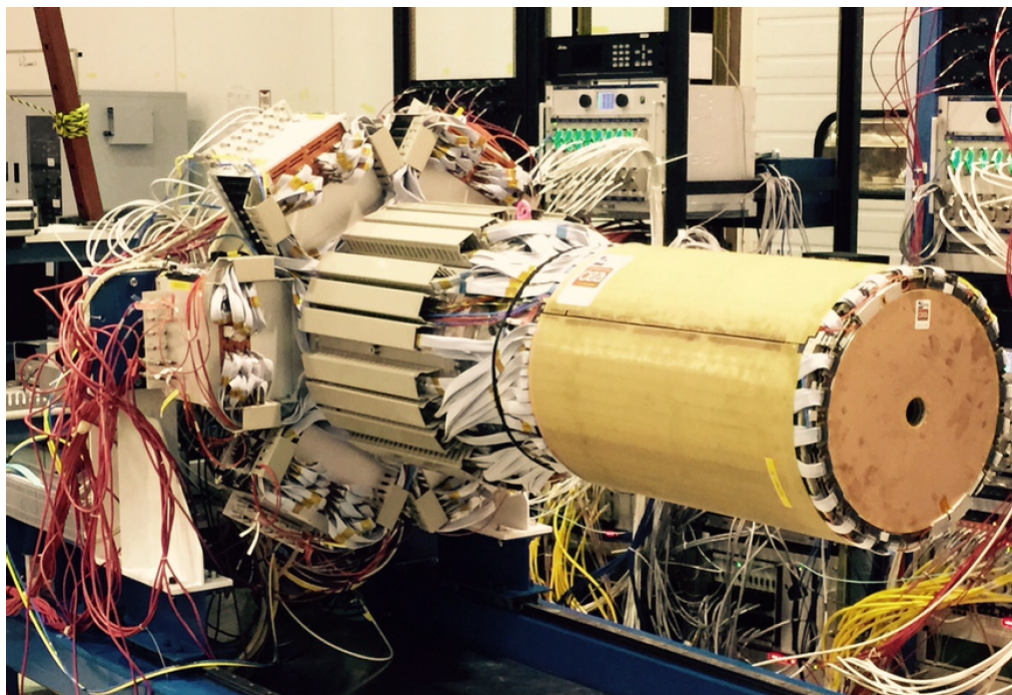


FIGURE 2.12: The fully assembled Central Vertex Tracker with the SVT, BMT, and FMT. The BMT and FMT are shown on the outside. The FMT has a circular opening in the center for the electron beam to pass through. The SVT is encapsulated and hidden from view.

Burkert et al., 2020.

Central Time-of-Flight (CTOF)

If the reaction got charged particles emerging from the target in the momentum range from 0.3 to ~ 1.25 GeV, the time-of-flight measurements for the identification of these particles are made by the CTOF.

This detector includes 48 plastic scintillators with double-sided PMT read-out via, respectively, 1.0 m-long upstream and 1.6 m-long downstream focusing light guides.

The array of counters forms a hermetic barrel around the target and the CVT. The barrel is aligned with the beam axis inside the 5 T solenoid magnet. The PMTs are placed in a region of 0.1 T fringe field of the solenoid and enclosed within a triple layer dynamical magnetic shield that provides less than 0.2 G internal field near the PMT photocathode.

A time resolution of 80 ps for charged particle identification in the CLAS12 Central Detector is provided thanks to the CTOF design.

Fig[2.13] shows the CTOF system from the design model, while Fig.[2.14] shows the CTOF installed inside the solenoid magnet.

Details of the CTOF are described in Carman, 2020a.

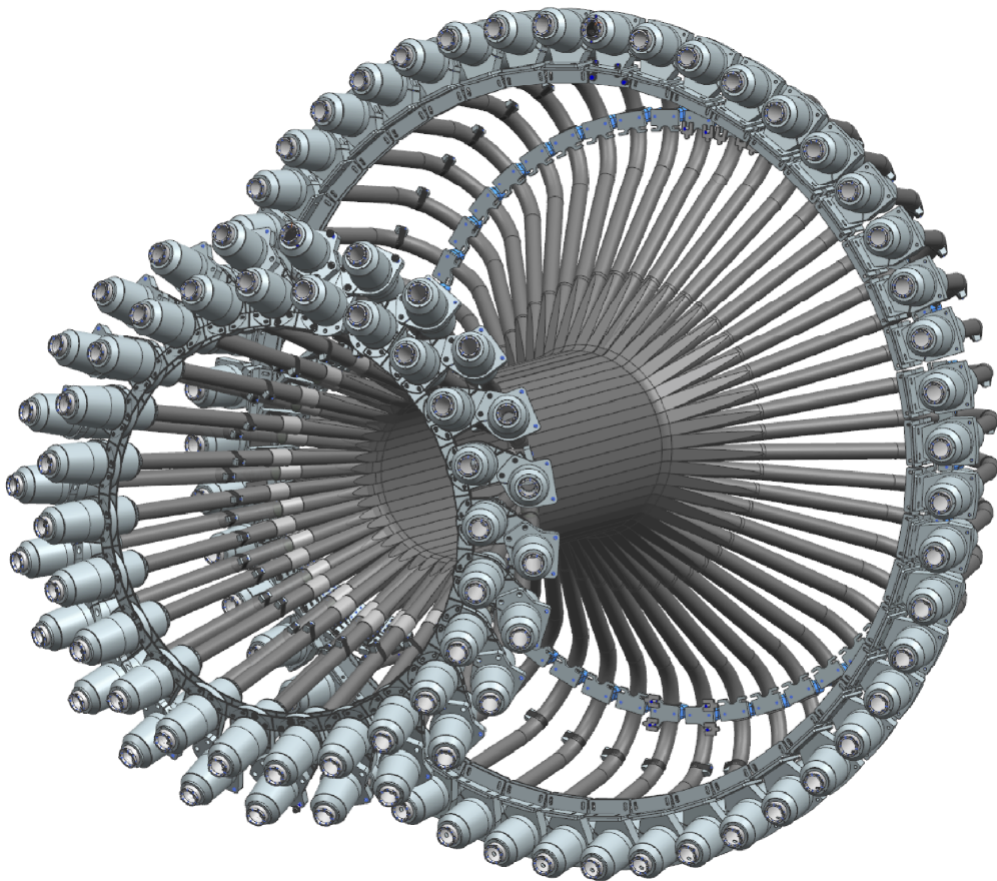


FIGURE 2.13: The CTOF detector with its 48 scintillator bars outfitted with light guides, PMTs, and magnetic shields at both ends of each counter.

Burkert et al., 2020.

Central Neutron Detector (CND)

The CND is positioned radially outward of the CTOF and allows the detection of neutrons in the momentum range from 0.2 to 1.0 GeV .

The detection is made by measurement of their time-of-flight from the target and the energy deposition in the scintillator layers.

The detector is made of three layers of scintillator paddles (48 paddles per layer), coupled two-by-two at the downstream end with semi-circular light guides and read out at the upstream end by PMT placed outside of the high magnetic field region of the solenoid. The scintillators are connected to 1 m -long bent light guides.

Fig.[2.14] shows the upstream readout end of the CND installed in the solenoid.

Details of the CND are described in Chatagnon, 2020.

Back Angle Neutron Detector (BAND)

The BAND detector's role in the CLAS12 apparatus is neutron detection at back angles.

The detector is positioned 3 m upstream of the CLAS12 target; in such way, it can detect backward neutrons with momenta between 0.25 and 0.7 GeV .

It consists of 18 horizontal rows and five layers of scintillator bars with PMT readout on each end to measure time-of-flight from the target. There is an additional 1 cm scintillation layer for vetoing charged particles. The detector covers a polar angle range from 155° to 175° with a design neutron detection efficiency of 35% and a momentum resolution of about 1.5%.

Further details will be provided in Segarra, 2020.

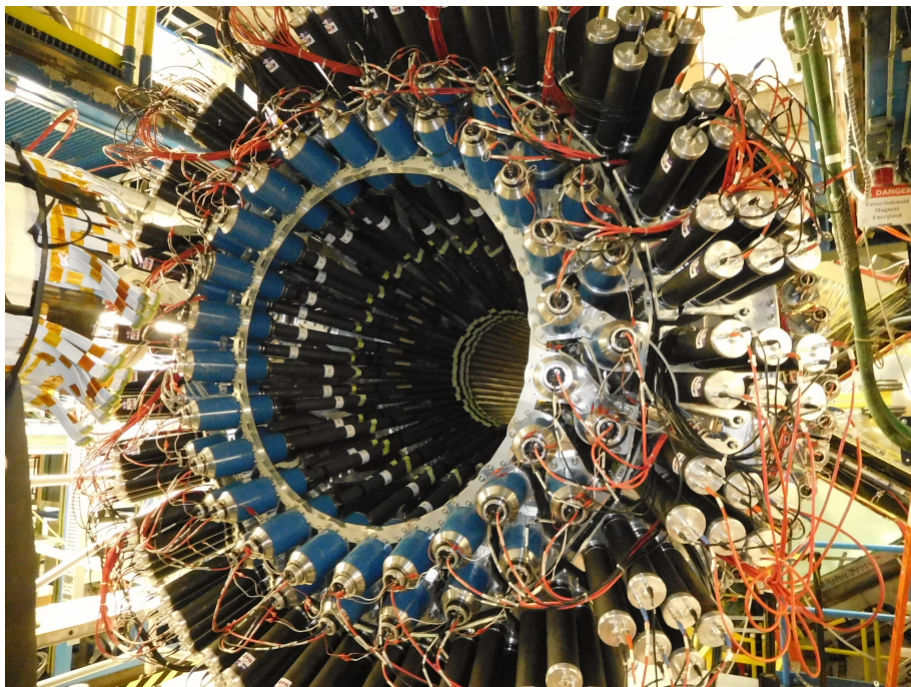


FIGURE 2.14: The fully assembled CD as seen from its upstream end with the 144 CND light guides and PMTs at the three outermost rings, and the 48 PMTs of the CTOF (two inner rings).

Burkert et al., 2020.

2.3 Forward Tagger

The Forward Tagger is a crucial component of the MesonEx experimental program focused, on the research and study of exotics and rare mesons; as previously introduced, this analysis requires measurements of a broad range of final states in order to consolidate the possible evidence of the production of the aforementioned particles. The study has to be carried on by looking at different decay modes and exploring poorly studied reaction channels, as can be seen in Battaglieri, 2005.

The experiment sees an 11 GeV electron beam scattering on a different sample of the target (LH^2 , H^2 , etc.) with multiple particles in the final state; the characteristics of the detector and the trigger conditions studied specifically for this investigation will allow measurements of many final states simultaneously: The produced hadrons will be detected in the CLAS12 spectrometer (previously described in this chapter) and the scattered electrons, when deflected at very small angles (2.5° to 4.5° in polar angle) and with low 4-momentum transfer (Q^2), will be detected in the Forward Tagger (FT). These conditions reflect a kinematic of the reaction of quasi-real photoproduction. In order to have optimal electron detection in this angular range, and to make the production compatible with the high rate of electromagnetic background, strict specifications were defined for the FT.

The reconstruction of the quasi-real photon variables makes it necessary to measure the scattered electron's three-momentum. The relevant quantities are:

- $E_{e'}$ (scattered electron energy), since the photon energy is given by $E_\gamma = \nu = E_{beam} - E_{e'}$ and its linear polarization by $P_\gamma = \epsilon \sim \left(1 + \frac{\nu^2}{2E_{beam}E_{e'}}\right)^{-1}$.
- $\phi_{e'}$ (scattered electron azimuthal angle), in order to determine the polarization plane.
- $\theta_{e'}$ (scattered electron polar angle), since $Q^2 = 4E_{beam}E_{e'} \sin^2(\theta_{e'}/2)$.

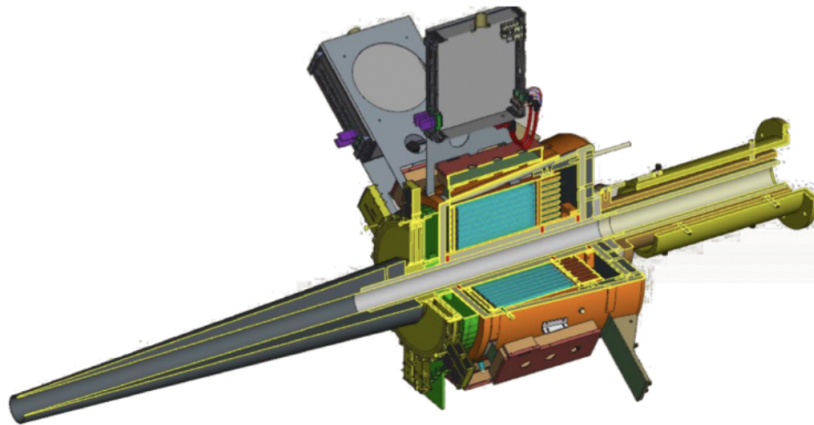


FIGURE 2.15: CAD drawing of the Forward Tagger. The FT calorimeter shown in cyan is located at about 185 cm from the beam-target interaction point and is enclosed in a copper and Rohacell case to provide thermal insulation. The scintillation counter (green) and the tracker (yellow) are located in front of the calorimeter. A tungsten cone (gray) shields the FT from Møller electrons and another electromagnetic background (low-energy photons) created by the beam. The left side of this figure represents the upstream end of the detector.

Acker et al., 2020a

In order to identify the electron in the energy range of $0.5 - 4.5 \text{ GeV}$, the FT is equipped with an electromagnetic calorimeter (FT-Cal), capable of identifying the aforementioned particle by measuring its electromagnetic shower energy. Along with the FT-Cal, the FT can count also on a Micromegas tracker (FT-Trk), which focus is the measure of the scattering angles ($\theta_{e'}$ and $\phi_{e'}$), and a scintillation counter (FT-Hodo), providing e/γ separation. The FT-Cal and FT-Hodo also provide fast signals to trigger the data acquisition (Boyarinov et al., 2020) in coincidence with signals from CLAS12.

Fig.[2.15] and Fig.[2.16] show CAD drawings of the FT.

The calorimeter, hodoscope, and tracker are placed between the HTCC and the torus magnet support, at about 185 cm downstream of the nominal target position. The close proximity to the beamline (2.5° corresponds to $\sim 8 \text{ cm}$ radial distance from the beamline) and the limited space available (at most $\sim 40 \text{ cm}$ along the beam axis), requires a compact calorimeter of small radiation length and with very good radiation hardness. The FT-Hodo is placed in front of the calorimeter and is made of plastic scintillator tiles read out by silicon photomultipliers via wavelength-shifting fibers, while the FT-Trk detector is located in front of the FT-Hodo to extend the acceptance of the FT down to 2.5° . All of these components were designed to have minimal impact on the operation and acceptance of the CLAS12 equipment in the forward direction, fitting within a 5.5° cone around the beam axis.

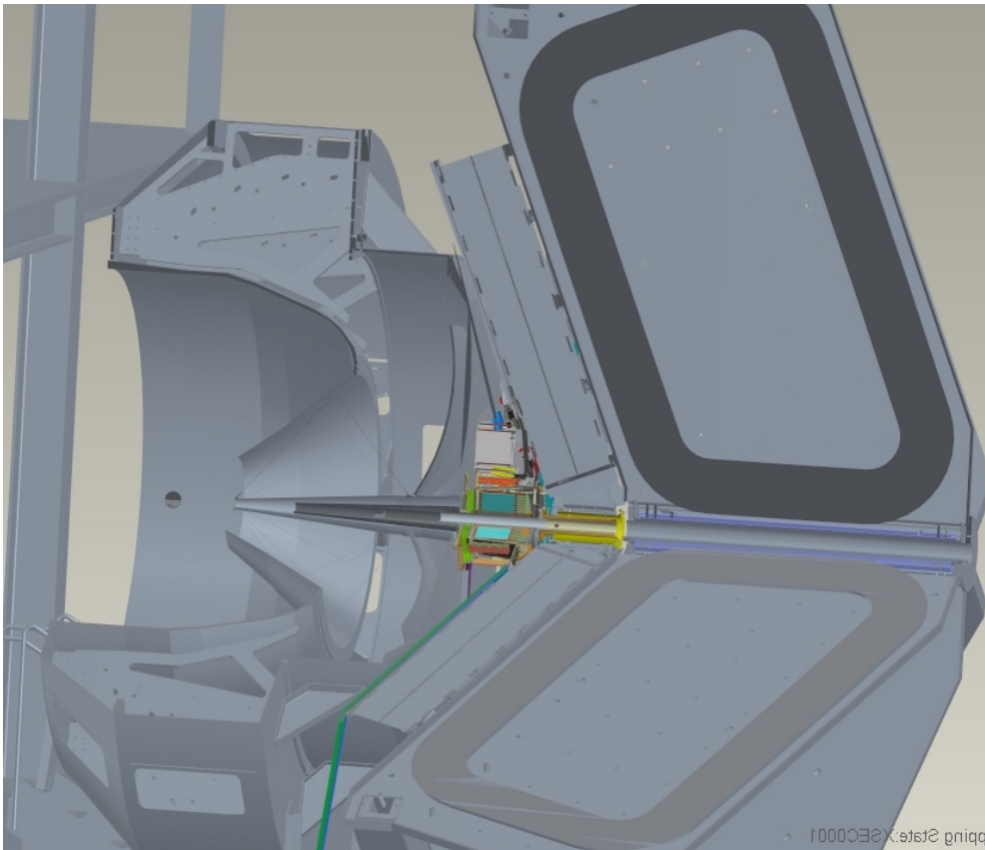


FIGURE 2.16: CAD drawing showing the integration of the FT in CLAS12. The FT is located in the free space between the HTCC and the first DC region.

Acker et al., 2020a

2.3.1 Detector Layout

The Calorimeter (FT-Cal)

Requirements in terms of radiation hardness, shower containment (small radiation length and Moliere radius), light yield, scintillation decay time, and good energy and time resolution are highly demanding, and the FT-Cal is built to fulfill such requests.

In order to determine precisely the photon energy and to ensure the exclusivity of the measured reaction via the missing mass technique, a high electron energy resolution is requested. However, the energy resolution on the latter is significantly better than the resolution of the electron, since we are interested in low-energy electrons and high-energy photons.

It's fundamental for the FT-Cal to reject background and to identify the relevant signals via coincidence with CLAS12; in sight of this, the FT-Cal should have a fast scintillation decay time ($\tau \sim 10 \text{ ns}$) to sustain high rates with small pile-up effects and to provide the scattered electron interaction time with good accuracy ($< 1 \text{ ns}$).

The calorimeter should be highly segmented in the transverse direction, due to the expected high rate from the electromagnetic background ($\sim 120 \text{ MHz}$ at the nominal luminosity of $1035 \text{ cm}^{-2}\text{s}^{-1}$). The size of each detection element should be comparable with the characteristic transverse size of the electromagnetic shower (Moliere radius) to contain the shower produced by incident electrons to a few read-out cells.

The photodetectors for the light readout should also work in a sizable magnetic field and fit within the available space. For this reason, standard photomultipliers

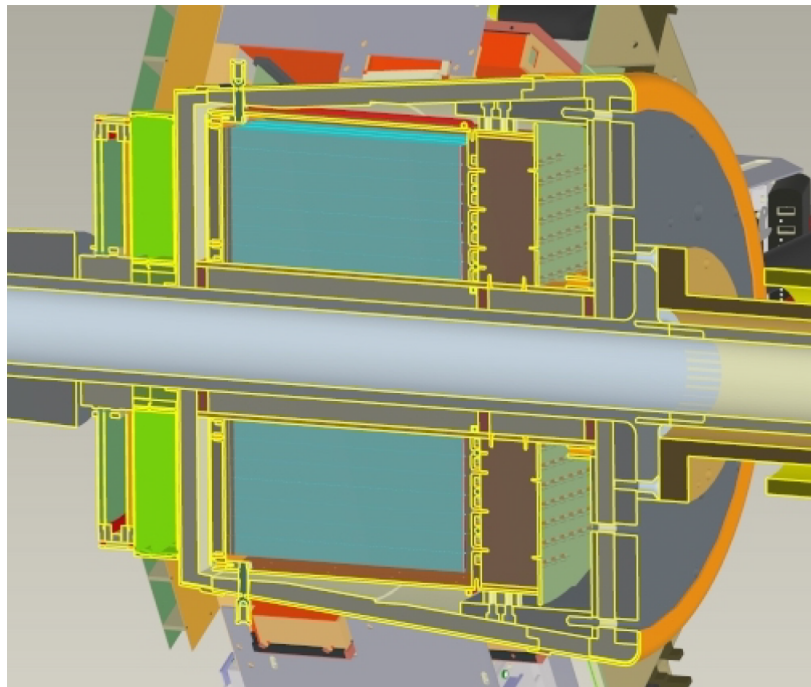


FIGURE 2.17: CAD drawing of the FT-Cal showing a cross-section of the detector. The crystals, in cyan, are enclosed in the copper thermal shield, in orange, surrounded by insulation, and in light gray. On the downstream end of the crystals (right side of the figure), the preamplifiers motherboard is shown in green. The weight of the crystals is supported by the tungsten pipe, in dark gray, which is an integral part of the beamline.

Acker et al., 2020a

(PMTs) cannot be used, while avalanche photodiodes (APDs) have been shown to meet the required criteria.

To match the necessary requirements, lead tungstate ($PbWO_4$) was chosen as the scintillating material, and Large-Area APDs (LAAPDs) as the readout sensors. Lead tungstate has a fast scintillation decay time ($6.5 ns$), a small radiation length ($0.9 cm$), and a small Moliere radius ($2.1 cm$). The drawback of limited light emission (about 0.3% of $NaI(Tl)$) has been mitigated by using cooled $PbWO_4$ Type-II crystals. With this design, based on GEANT simulations, an energy resolution on the order of $(\frac{2}{\sqrt{E(GeV)}} \oplus 1)\%$ is expected.

The FT-Cal is made from 332 $15 \times 15 \times 200 mm^3$ parallelepiped $PbWO_4$ Type-II crystals arranged around the beamline with full azimuthal angular coverage ($0^\circ < \phi < 360^\circ$) and small forward angle acceptance ($2^\circ < \theta < 5^\circ$). The crystals are placed with their long side parallel to the beamline to form a ring. Fig.[2.17] shows a CAD rendering of the calorimeter.

The Hodoscope (FT-Hodo)

The FT-Hodo is designed to discriminate between electrons and photons that produce an electromagnetic shower inside the calorimeter. Specifically, differently from photons, electrons are identified by hits in the hodoscope array that are correlated in position and time while a cluster is observed in the calorimeter.

The FT-Hodo is comprised of an array of 232 plastic scintillators (Eljen-204) tiles segmented in two layers in order to suppress the electromagnetic shower splashback contributions. The showers, created by events depositing energy in the FT-Cal, are reduced in intensity thanks to the scintillator fast timing; also, sufficient resistance to radiation damage is required by the detector, working in the high-rate and high-dose environment of the FT.

The geometry and readout of the hodoscope are constrained by the surrounding apparatus. The device is positioned upstream of the FT-Cal, fitting into a disk of diameter $330 mm$ and $42 mm$ depth. The readout is achieved using $3 \times 3 mm^2$ Hamamatsu S13360-3075PE SiPMs (50% photon detection efficiency for $450 nm$ photons) coupled to $5 m$ -long clear optical fibers (Kuraray clear-PSM with attenuation length $> 10 m$), which are fusion spliced to $\sim 30 cm$ -long wavelength shifting (WLS) Kuraray Y11 fibers (attenuation length of $> 3.5 m$), embedded in the scintillator tiles.

The FT-Hodo, composed of an upstream and a downstream layer, is comprised of 44 $15 mm \times 15 mm$ (P15) and 72 $30 mm \times 30 mm$ (P30) scintillators arranged as shown in Fig. 10. The two layers utilize $7 mm$ and $15 mm$ -thick scintillator tiles, respectively for the upstream and downstream layer. The first one is a thinner layer employed to reduce photon conversion inside the hodoscope, while the second one provides the most accurate timing information for the event.

The number of scintillation photons collected from each tile is maximized thanks to four WLS fibers embedded in the P30 tiles and two in the P15 tiles. These fibers were glued inside diagonal holes to maximize the path length in the scintillator and to allow for the tiles to be arranged without any dead space between the elements. Each tile was polished and painted with two layers of reflective paint for the sides and three layers for the scintillator faces. Then the tile is secured in position on the surface of a $1 mm$ -thick plastic support board.

This, along with a light-proof carbon cover screwed on the front and the back of the system, results in a total detector thickness of $42 mm$.

Typical maximum radiation doses are determined through Geant4 simulations, using realistic beam and target parameters and excluding the shielding effects of the Møller cone. In the discussed case, the hodoscope will experience a 20% light loss in the WLS fibers after 3.5 years, while the plastic scintillators will experience 20% light loss after 300 years (Battaglieri, 2015).

The analog signal from the SiPM is fed directly to a custom-designed preamplifier board designed by the INFN-Genova Electronics Group. The boards host 8 independent channels, each coupled to a SiPM and mounted in pairs in the slots of a custom crate. The 16 SiPMs are mounted on a circuit board that distributes the bias HV to each component and collects their signals.

The first stage of the channel is composed by a low-noise NPN BJT (BRF92) with a high cut-off frequency and good stability, while the second one is built of an OPA694 operational amplifier in a non-inverting configuration. A 100 nF capacitor couples the two stages, removing the DC component of the signal from the second transistor. The amplifier is coupled to the output connector through a 100 nF capacitor and a 50Ω resistor, which removes any DC component from the last stage and matches the impedance of the output cable. If the trigger condition is satisfied, the digitalized signals are stored for further analysis.

Fig.[2.18] shows a CAD rendering of the hodoscope.

The Micromegas Tracker (FT-Trk)

A tracker complements the Forward Tagger detectors, for a precise determination of the electron scattering angle.

Two Micromegas detectors are located in front of the hodoscope, in the space between the FT and the HTCC. The two detectors are indeed a good compromise to achieve an efficient background rejection and track reconstruction with a low material budget.

Each layer is composed of a double-faced Micromegas disk, both covered by detection strips: the downstream strips are oriented perpendicularly to the upstream strips, enabling the determination of the spatial coordinates of a track.

Choosing a pitch of $500\text{ }\mu\text{m}$, the resolution is fixed around $500/\sqrt{12} \sim 150\text{ }\mu\text{m}$. Good efficiency is achieved thanks to a drift space of 5 mm , along an amplification gap of $128\text{ }\mu\text{m}$. Angular acceptance goes from 2.5° to 4.5° , with an active area between a 70 mm and a 143 mm radii. The total number of channels, using this geometrical configuration, is 3072.

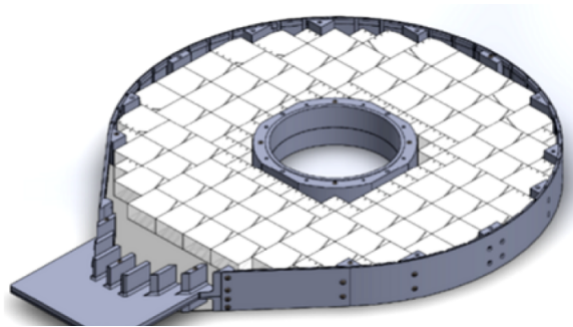


FIGURE 2.18: CAD drawing of the FT-Hodo showing one layer of tiles, the location of the plastic spacers, and the plastic strip that traces the outer contour.

Acker et al., 2020a

The FT-Trk readout consists of a Front-End Unit (FEU) and a Back-End Unit (BEU). The front-end electronics are responsible for signal preamplification and shaping, along with the data digitization and compression and the buffering during the trigger generation process. The non-amplified analog signals transit via the cable assemblies from the chambers to the front-end electronics.

The back-end electronics are responsible for data concentration, providing the interface to the CLAS12 event-building system.

Fig.[2.19] shows a 3D view of the Micromegas Tracker.

2.3.2 Events Reconstruction

The CLAS12 Java reconstruction framework it's in charge of the reconstruction of all the FT detector information and the matching between them, in order to determine the type and three-momentum of the detected particles (Ziegler, 2020). The main steps are briefly summarized in the following list:

- **FT-Cal:** raw data are extracted from the FADC and used for cluster reconstruction. The energy and centroid of the cluster are then used to define the three-momentum of the incident particle.
- **FT-Hodo:** raw data are extracted from the FADC and used for the cluster reconstruction. Two matching clusters in the two layers of the detector are then

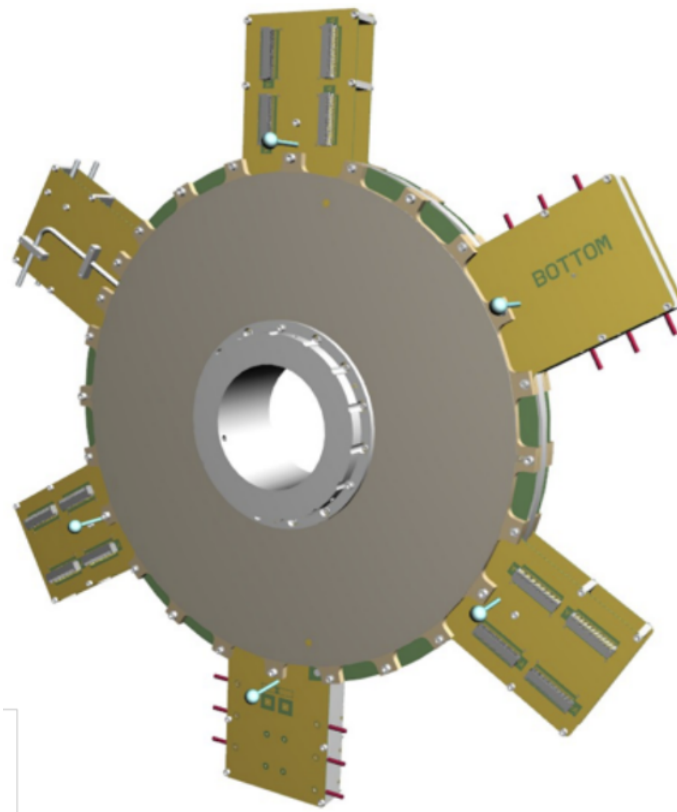


FIGURE 2.19: CAD drawing of the upstream face of the FT-Trk Micromegas Tracker equipped with front-end electronics.

Acker et al., 2020a

compared to the clusters inside the FT-Cal. Charged and neutral particles can be distinguished thanks to this comparison.

- **FT-Trk:** raw data are extracted from the FADC and used for the cluster reconstruction. Combinations of clusters in the X-Y layers of FT-Trk and FT-Hodo are used to define the path of the cluster. This information is then matched to the FT-Cal cluster, improving the determination of the impact point of the particle.

2.3.3 Detector Performance

In order to know the FT performance, different beam energies and trigger conditions have been used to produce data. Results from the studies of the output are detailed below.

Acceptance

The detector acceptance was studied in detail at the maximum beam energy the experiment operated at so far (10.6 GeV). Data were recorded with a minimum-bias trigger based on the FT-Cal alone with a threshold on the measured cluster energy of 100 MeV.

In the offline analysis, events were further selected, requiring a reconstructed electron via the matching of the FT-Cal cluster to FT-Hodo hits, and the associated FT-Cal cluster to have total energy greater than 500 MeV, seed energy greater than 300 MeV, and size greater than or equal to 4 crystals. The resulting event distributions as a function of the electron energy and polar angle are shown in Fig.[2.20].

The energy coverage extends from 500 MeV, as selected in the offline analysis, up to the end-point set by the beam energy where elastic scattering dominates. Close to the energy end-point, the detector resolution is expected to worsen significantly because of the saturation of the FT-Cal preamplifiers and FADCs that are optimized for the design energy range of 0.5 – 4.5 GeV.

The θ range extends from the minimum angle of 2.5° to $\sim 5^\circ$. The two-dimensional distribution shows the effect of the CLAS12 solenoid field on low-momentum electrons starting from $\theta \sim 2^\circ$ that are bent into the detector acceptance. The detector acceptance matches and partially exceeds the design specifications.

Energy Resolution and Electromagnetic Shower Reconstruction

Within the detector acceptance, the energy resolution was studied based on elastic scattering and π^0 decay to two photons, as discussed in Section. 6. The results indicate the currently achieved resolution is larger than the design value by about 1% at 2 GeV. The reasons for this discrepancy can be multi-fold.

First, the energy calibration of individual crystals has shown a significant spread in the energy-to-charge conversion that was not foreseen in the initial estimates. This spread, likely due to the non-uniformity of the crystal light yield, can contribute to a worsening of the resolution because it results in a non-homogeneous detector response.

Second, as a consequence of the crystal non-uniformity, the threshold applied in the cluster reconstruction is for some crystals larger than the 10 MeV used in the simulation studies and prototype analyses.

The shower profile in the FT-Cal was studied and compared to Monte Carlo simulations for different particle species. Fig.[2.21] shows the shower radius, defined

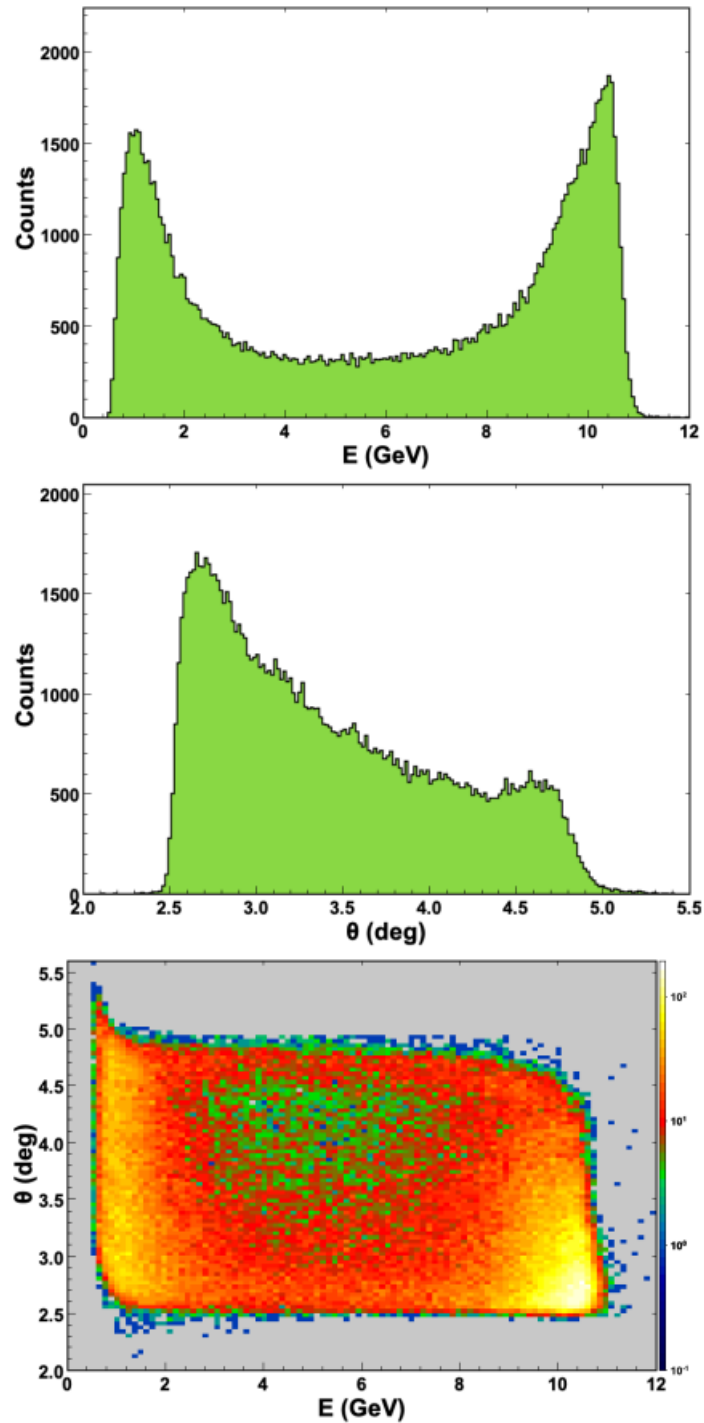


FIGURE 2.20: FT acceptance for electrons as a function of energy (top), polar angle (middle), and of both variables (bottom) at 10.6 GeV beam energy. The energy range goes from 500 MeV, as selected in the offline analysis, up to the end-point set by the beam energy where elastic scattering dominates. The θ range goes from the minimum angle of 2.5° to $\sim 5^\circ$. The two-dimensional distribution shows the effect of the CLAS12 solenoid field on low-momentum electrons that start from $\theta \sim 2^\circ$ and are bent into the detector acceptance.

Acker et al., 2020a

as the square root of the second moment of the shower, for charged particles, i.e. particles associated with a cluster in the calorimeter with matching hits in the hodoscope. A clear peak with a radius of $\sim 1\text{ cm}$ associated with electrons is clearly visible, overlapping a broader distribution associated with hadronic showers. The shower profile and, specifically the cluster radius, can therefore be used to discriminate between different particle types.

Timing Resolution

The timing resolution for electrons and photons was evaluated from beam data by correlating the reconstructed cluster time from the FT-Cal to either the RF signal that is synchronous with the CEBAF accelerator beam bunches or the event start time derived from the CLAS12 FTOF system.

Specifically, the electron time resolution was studied by correlating the FT time projected back to the event vertex to the RF signal time. The difference of these two times for 10.6 GeV data is shown in Fig.[2.22] for electrons with energy greater than 500 MeV , cluster seed energy greater than 300 MeV , and cluster size greater than or equal to 4 crystals: a Gaussian fit to the distribution gives $\sigma \sim 140\text{ ps}$. The tails of the distribution are due to low-energy clusters close to the applied selection threshold and are expected to be reduced by improvements in the time-walk correction that are currently under study.

While this estimate of the time resolution relies solely on the FT reconstruction, an alternative measure can be performed by selecting photons detected in the FT and correlating their time to the event start time determined from other particles detected in CLAS12. This analysis was performed for events with an electron detected in the CLAS12 Forward Detector whose start time is determined based on the FTOF system and a photon detected in the FT with energy greater than 500 MeV , cluster seed energy greater than 300 MeV , and cluster size greater than or equal to 4 crystals.

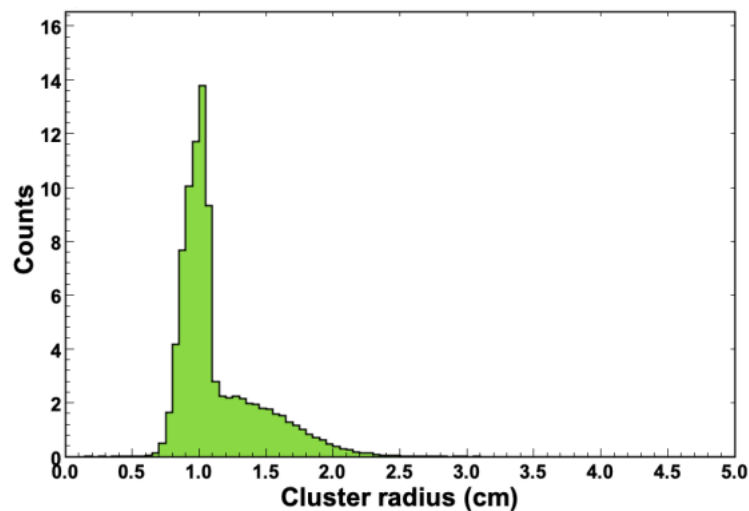


FIGURE 2.21: Radius of the FT-Cal shower for charged particles. A clear peak at $\sim 1\text{ cm}$ associated with electron-induced electromagnetic showers overlaps with a broader distribution due to hadronic showers.

Acker et al., 2020a

The photon FT time projected back to the event vertex was correlated with the event start time as shown in Fig.[2.22]. A Gaussian fit to the distribution gives $\sigma \sim 150$ ps, slightly larger but consistent with the electron timing resolution.

While the FT hit time is determined by the calorimeter since this is the component with the best timing resolution, the time correlation between the individual FT detectors is important to match the signals detected in the three sub-components and minimize accidentals. Fig.[2.23] shows the time difference of the reconstructed calorimeter and hodoscope clusters for detected electrons with $\sigma \sim 0.8$ ns, dominated by the hodoscope resolution. The value is consistent with the design resolution for the hodoscope of < 1 ns.

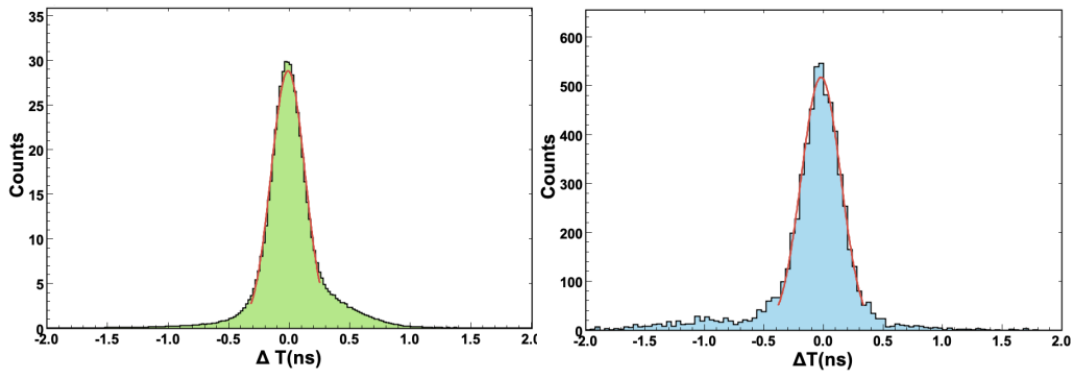


FIGURE 2.22: Time resolution for electrons (left) and photons (right) detected in the FT with energy greater than 500 MeV, seed energy greater than 300 MeV, and cluster size greater than or equal to 4. The histogram shows the time difference between the FT time projected back to the event vertex and the RF signal time (left) or the event start time derived from the CLAS12 FTOF detector for events where an electron is identified in the CLAS12 Forward Detector (right). The Gaussian fit gives a resolution $\sigma \sim 140$ ps (left) and ~ 150 ps (right).

Acker et al., 2020a

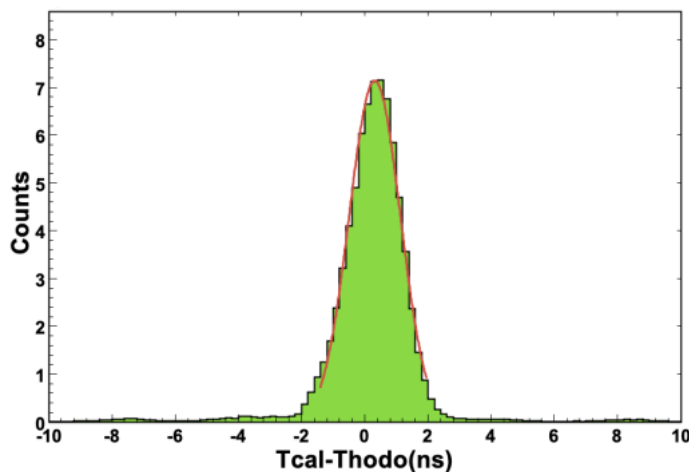


FIGURE 2.23: Time difference between the calorimeter and hodoscope clusters for reconstructed electrons. The Gaussian fit to the distribution gives $\sigma \sim 0.8$ ns.

Acker et al., 2020a

2.3.4 Trigger System

In experimental setups, the quasi-photoproduction trigger is employed when a scattered electron is detected in the Forward Tagger calorimeter and hodoscope. The trigger decision in these experiments is more intricate compared to simple electroproduction experiments. The specific configuration of the trigger detectors relies on the particular reaction being studied and may involve the following components:

- **Forward Tagger calorimeter:** The trigger selects events based on the energy deposition in the calorimeter, satisfying a minimum energy threshold (E_{min}) and a maximum energy threshold (E_{max}).
- **Number of clusters:** The trigger considers the number of clusters formed in the calorimeter as a criterion for event selection.
- **Forward Tagger hodoscope:** The hodoscope is geometrically aligned with the calorimeter cluster position to discriminate between electrons and photons.
- **DC roads:** Information from the DC system, which reconstructs particle trajectories, is utilized in the trigger decision.
- **PCal and ECal energy deposition:** The energy deposition in the PCal (Pre-shower Calorimeter) and ECal (Electromagnetic Calorimeter) is taken into account by the trigger.
- **Coincidence between PCal and FTOF:** The trigger looks for a coincidence between the PCaU (Upper Pre-shower Calorimeter) and FTOF (Forward Time-of-Flight) detectors, ensuring a geometric match.
- **CTOF and CND:** The trigger may involve the CTOF (Central Time-of-Flight) and CND (Central Neutron Detector) detectors or a coincidence between CTOF and CND, depending on the experimental requirements and geometry match considerations.

The combination of these trigger detector components, tailored to the specific reaction under investigation, allows for the selection of relevant events and the discrimination between various particles, such as electrons and photons, within the quasi-photoproduction experiments.

Fig. 2.24 illustrates the dependence of electron trigger rates on the beam current. It is observed that the rates for the inbending configurations of rg-A is not linear with respect to the beam current. However, the situation is more favorable for the outbending configuration, where the rates exhibit a better behavior. To mitigate the issue of accidental coincidences in the inbending Torus configuration, efforts can be made to reduce the coincidence window between the HTCC and calorimeters, which would necessitate improved timing alignment.

At a beam current of 50 nA, corresponding to a luminosity of $L = 0.66 \times 10^{35}$ for the hydrogen target, the inbending electron trigger rate remains below 20kHz. Even at a higher luminosity of $L = 2.0 \times 10^{35}$, the inbending rate does not exceed 20kHz. In comparison, the outbending configuration of CLAS12 consistently exhibits higher electron trigger rates than the inbending configuration. The projected electron trigger rates for luminosities of $L = 10^{35}$ (75nA) and $L = 2 \times 10^{35}$ (150nA) are expected to be 20kHz and 30kHz, respectively. More information about the system trigger are reported in Kubarovsky, 2020.

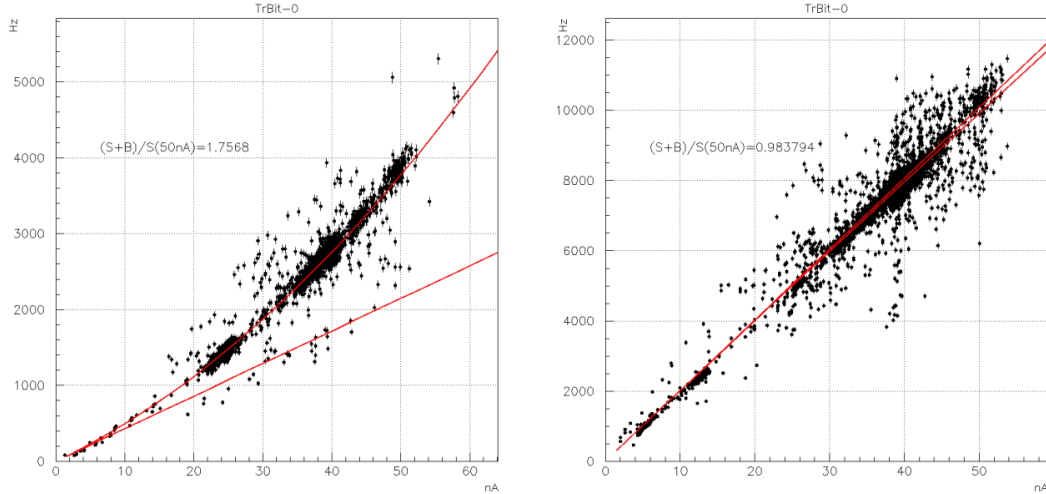


FIGURE 2.24: Electron trigger rate. The left and right panels shows the inbending and outbending configurations, respectively. Kubarovsky, 2020

Forward Tagger Trigger

The Forward Tagger trigger mechanism is specifically devised to identify events in which a scattered electron is detected by the detector within the polar angular range of 2 to 5 degrees. It is important to note that the investigated photoproduction processes involve electron scattering with a low four-momentum transfer $Q^2 = 4E_{beam}E' \sin^2 \theta / 2$.

The trigger logic operates continuously, searching for clusters within the FT calorimeter that correspond to electromagnetic showers. It computes the energy and spatial coordinates of these clusters. The cluster energy is determined as the sum of crystal energies within a 3x3 spatial array that satisfies the time-matching criteria. Once a cluster is identified by the clustering algorithm, the associated data, including the timestamp, energy, and spatial coordinates (centered around the seed crystal), is reported to the subsequent trigger stage. Notably, at this stage, the cluster energy is not corrected for shower leakage effects.

Subsequently, the trigger processor employs additional selection criteria, involving energy thresholds and the number of hits within a cluster, to make the final trigger decision. The trigger can also be configured to select events with a specified number of clusters detected by the calorimeter. Furthermore, the presence of a two-plane scintillating hodoscope located in front of the calorimeter enables discrimination between charged particles and high-energy photons. This functionality also facilitates the selection of reactions featuring an electron and multiple photons in the final state, such as the reaction $ep \rightarrow e'\gamma\gamma X$.

To enhance the trigger system's capabilities, information from the CLAS12 Forward and Central Detectors can be utilized to select events exhibiting coincidences between the electron detected in the FT calorimeter and several charged or neutral particles. The composition of the trigger detectors depends on the specific reaction under investigation.

In the case of charged particles detected by the Forward Detectors, a coincidence is established by cross-referencing data from the Forward Time-Of-Flight (FTOF), Pre-shower Calorimeter (PCAL), and Electromagnetic Calorimeter (EC) with tracks

reconstructed by the Drift Chambers (DC) system. Accurate spatial correlation between all trigger detectors, including the coordinates of tracks intersecting the detector planes, is necessary. The effective matching of hits along the trajectory forms a vital component of background reduction at the trigger level.

Energy deposition thresholds imposed on the trigger detectors play a crucial role in the selection of charged and neutral particles. As mentioned earlier, the minimum energy depositions required in each trigger detector are adjustable parameters tailored to the specific experimental requirements.

The fundamental trigger used for the photoproduction analysis, which can be extracted from the Trigger setup file reported in Appendix A, is reported in the following listing. P.N. The Central Trigger Bit 1, which fire with an FT cluster multiplicity minimum of 2 within 16 nanoseconds of time difference between 500 and 8500 MeV, has been then used as a Global Trigger Bit (#26, as can be seen from the aforementioned file), and used as CLAS12 trigger for photoproduction events.

LISTING 2.1: Central Trigger Bit 1, from Forward Tagger trigger settings.

```

1 | #####
2 | # Central Trigger bit 1      CTRG1:  FT(500-8500) 2 clusters
3 | #####
4 | SSP_GTC_CTRG                1
5 | SSP_GTC_CTRG_EN             1
6 |
7 | SSP_GTC_CTRG_FT_CLUSTER_MULT_EN          1
8 | SSP_GTC_CTRG_FT_CLUSTER_MULT_COINCIDENCE 16
9 | SSP_GTC_CTRG_FT_CLUSTER_MULT_MIN         2
10 |
11 | SSP_GTC_CTRG_FT_CLUSTER_EMIN             500
12 | SSP_GTC_CTRG_FT_CLUSTER_EMAX            8500
13 | SSP_GTC_CTRG_FT_CLUSTER_HODO_NMIN       0
14 | SSP_GTC_CTRG_FT_CLUSTER_NMIN            1
15 | SSP_GTC_CTRG_FT_CLUSTER_WIDTH           0

```


Chapter 3

Data Analysis

As the core sector of the research process, the next chapter will provide an introduction to the frameworks used during the analysis and a step-to-step description of the analysis process. This last topic will be divided into two different subsections: while the first one will show the different cuts applied to the analyzed data, the second one will describe the detector acceptance calculation process.

3.1 RunGroup-A Description

The RG-A configuration, which began in 2018 after the Hall B engineering run, marked the start of a major group of experiments in CLAS12. RG-A comprised a set of experiments that shared a common experimental setup, including the magnetic field setting, target, and beam currents. One of the experiments conducted as part of RG-A focused on π^0 photoproduction, requiring communication and negotiations among different experiments regarding the experimental settings.

The primary objective of RG-A was to conduct simultaneous measurements covering a wide range of physics topics. The group included 13 experiments developed by the CLAS collaboration and approved by Jefferson Lab's Program Advisory Committee (PAC). These experiments fell into five distinct sub-categories:

- **Deep Exclusive Processes:** These studies aimed to access Generalized Parton Distributions (GPDs) that describe correlations between longitudinal and transverse positions of partons. Examples of deep exclusive processes included π^0 production and Deeply Virtual Compton Scattering (DVCS).
- **Deep Inclusive and SIDIS:** This category focused on semi-inclusive deep inelastic scattering (SIDIS) to establish the kinematic region where SIDIS pion production could be connected to next-leading-order QCD in terms of parton distributions and parton fragmentation functions.
- **Quasi-Real Photoproduction:** Experiments in this category utilized photoproduction techniques to study Timelike Compton Scattering (TCS) and π^0 photoproduction.
- **Nucleon Structure:** These studies focused on analyzing the spectrum of N states in electroproduction channels, which provided insights into the structure of N particles.
- **MesonEx Program:** Utilizing the CLAS12 Forward Tagger, this program aimed to study the meson spectrum at low Q^2 values. Of particular interest were exotic hybrid mesons, which are quark-antiquark-gluon bound states that play a crucial role in understanding hadron structure.

To meet the physics requirements of these five categories, specific experimental run conditions were established, including configurations for beam energy, beam current, the data acquisition system (DAQ), and trigger systems. The summary of these run conditions is as follows:

- **Torus Magnet:** The magnet operated at full field strength, with both polarities used for in-bending electrons 75% of the time and out-bending electrons 25% of the time.
- **Solenoid:** The solenoid magnet operated at full field strength.
- **Beam Current Ranges:** The beam current varied from 5 *nA* to 75 *nA*.
- **Target:** Liquid hydrogen was the primary target, with occasional data taking on the empty target cell.
- **Beam Energy:** The beam energy was set to 10.6 *GeV* in the Fall of 2018 and 10.2 *GeV* in the Spring of 2019.

3.1.1 CLAS12 Reconstruction Software

In the field of nuclear and particle physics, having a durable and adaptable software framework for long-term data analysis is crucial. The MesonEx experiment, in particular, required a comprehensive software framework that encompasses a wide range of analysis tools and services for each detector system. This software framework serves several primary objectives, including event reconstruction, calibration, monitoring, CLAS12 physics analysis, detector geometry, and access to the CCDB (CLAS Calibration Database).

At the core of the CLAS12 software framework architecture lies CLARA, a modular design that is based on data-stream processing. CLARA is built by assembling essential services using pipes and is implemented in Java due to its portability and versatility across different systems. During the development of the CLAS12 Event Builder (EB) between 2016 and 2017, it played a crucial role in constructing a software reconstruction package that effectively organizes the relevant information captured by the CLAS12 detector during physics events. The COATJAVA package, which is part of the CLARA analysis framework, is a Java-based reconstruction package comprising a collection of services associated with individual detectors. These services convert the values of Analog-to-Digital Converters (ADCs) and Time-to-Digital Converters (TDCs) into physical quantities such as energy and time. What makes the CLAS12 Event Builder (EB) unique is that it receives data banks as input and utilizes this information to correlate different aspects of the event. The EB provides data analysts with essential event-specific values such as particle identification quantities, event helicity, and accumulated charge, enabling them to filter events during post-processing for specific final states.

The order in which the Event Builder (EB) is utilized is crucial. After other detector services complete their calculations and output their data banks, the EB is called as a service during the data reconstruction stage. This includes hit-based drift chamber tracking, which relies solely on the position of DC wires and does not involve timing information at this stage. The CLAS12 EB utilizes hit-based tracks and matches these track trajectories to hits in other detectors within the Forward Detector (FD). A trigger assignment algorithm is used, where a trigger particle, typically an electron, is employed to calculate the event start time. This event start time is then used in hit-based tracking, and the entire process is repeated using refined tracks.

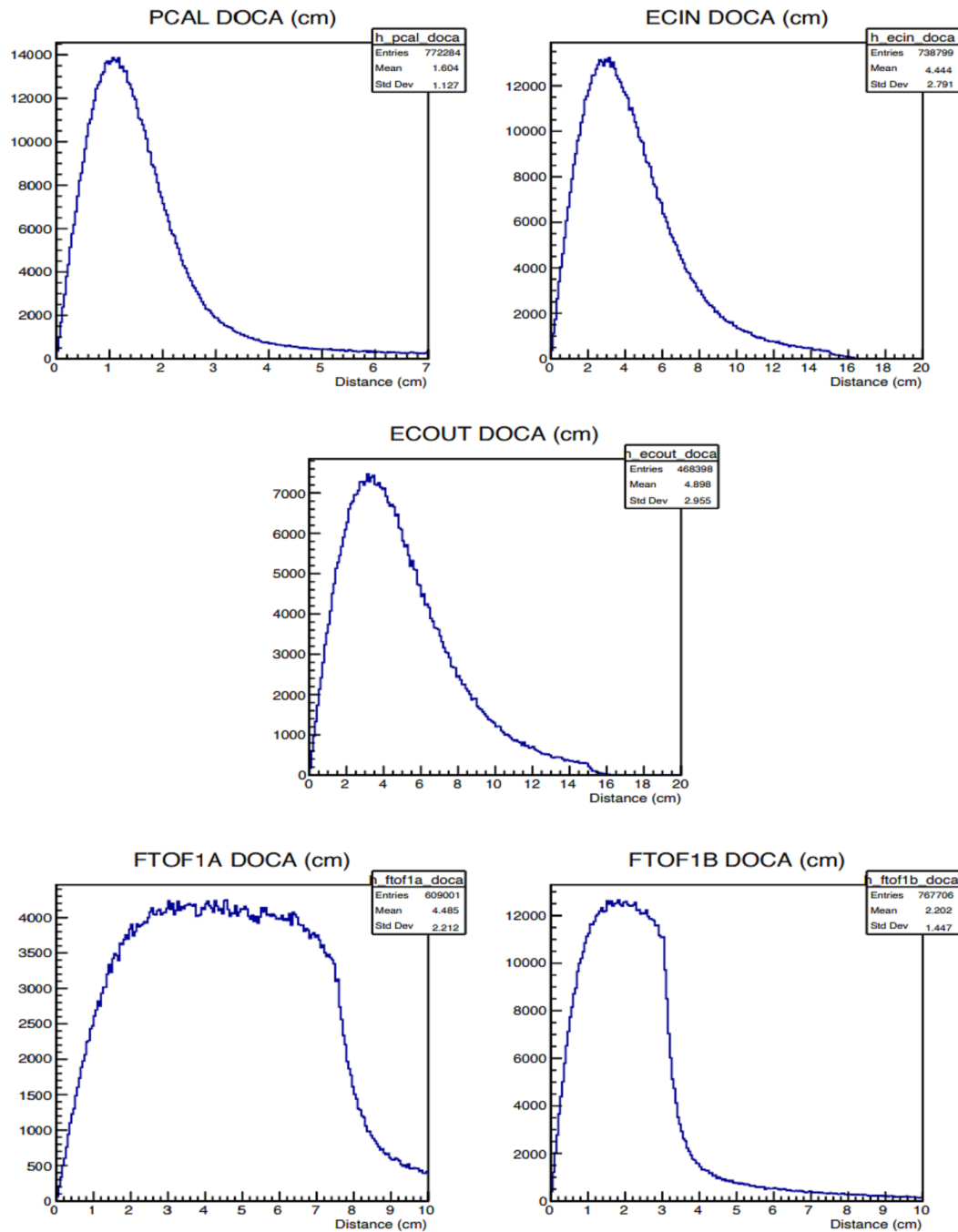


FIGURE 3.1: Illustration of the Distance of Closest Approach (DOCA) in CLAS12 detector layers. The DOCA represents the minimum separation between the particle trajectory and the detector hit position. It plays a crucial role in determining particle characteristics beyond momentum and vertex information. The DOCA values are calculated by geometrically matching track trajectories with hits in individual detector layers, providing valuable insights into particle behavior and interaction within the detector. This figure visually demonstrates the significance of DOCA in understanding particle trajectories and their proximity to detector hits. Newton, 2021

One of the key aspects of organizing event information is geometrically matching track trajectories with hits in individual portions of the CLAS12 detector. For example, when an electron emerges from the target vertex, it follows a curved path due to the combined magnetic fields of the Torus and Solenoid. The curvature of this path is quantified as momentum in the Drift Chamber (DC). Beyond the DC, where the magnitude of the magnetic field diminishes significantly, the particle trajectory becomes more linear towards the detector material. The Event Builder (EB) calculates the Distance of Closest Approach (DOCA) for hits in all layers of detectors. This geometric matching process plays a crucial role in determining the characteristics of the particle beyond momentum and vertex information. Fig. 3.1 illustrates the DOCA values of simulated electrons in all layers of the forward calorimeters, and Fig. 3.2 provides a visual representation of a particle's trajectory approaching the proximity of detector hits. The magnitude and resolution of the DOCA values depend on the hit position resolutions of the detectors. In the EB code, cut thresholds based on spatial resolutions are applied. The EB output banks display the results of the hit association between particles and detector responses.

Accurate reconstruction of time-based tracking and particle identification relies on understanding the timing values within events. The timing reported by detector responses represents absolute values from a DAQ (Data Acquisition) trigger clock. To utilize the TDC information reported by detectors, the time of the interaction that generated the event must be determined. Thus, calculating the event start time is

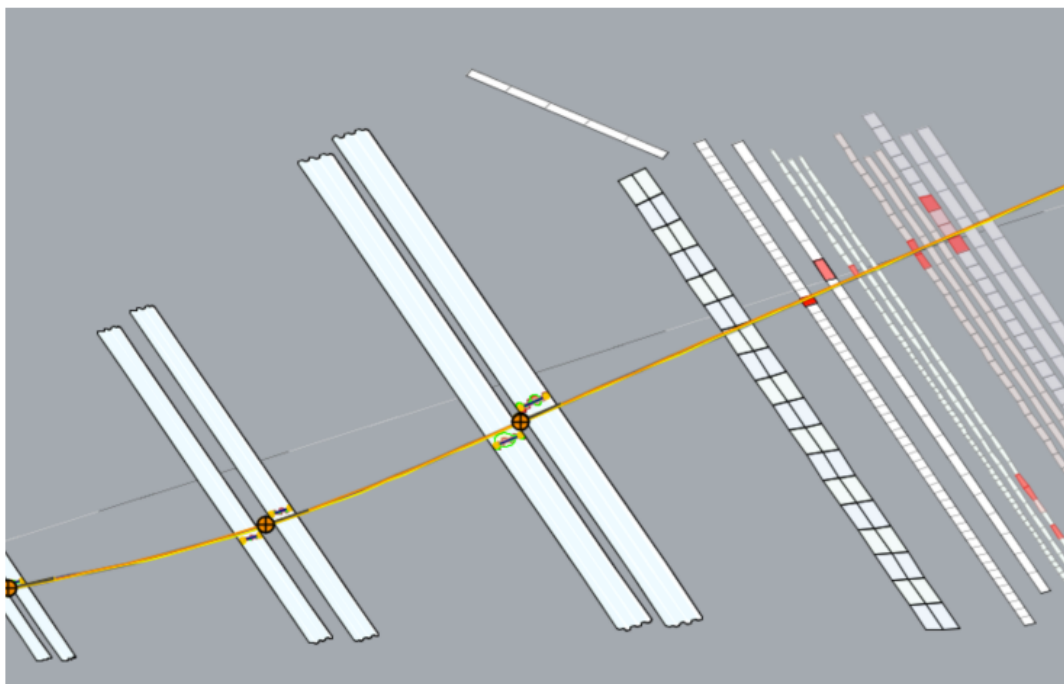


FIGURE 3.2: CED display showcasing a charged particle track traversing the material of the CLAS12 forward detector. The Charged Particle Event Display (CED) provides a visual representation of the particle's path as it interacts with and penetrates the various layers of the forward detector. This visualization offers valuable insights into the particle's trajectory, highlighting its interaction points and the energy deposition pattern along its path. The CED display serves as a powerful tool for studying charged particle behavior within the CLAS12 detector, aiding in the analysis and understanding of particle interactions and detector responses. Newton, 2021

a crucial step that enables the utilization of absolute timing values for tracking reconstruction and particle identification in various CLAS12 detectors. As mentioned earlier, the EB is called after hit-based tracking, and information collected at this stage is used by the EB. During hit-based tracking, a trigger candidate is identified to calculate the event start time. Electrons are suitable trigger candidates due to their nearly constant and known velocity, and their identification does not depend on detector times but rather on values such as the sampling fraction in the ECAL and the number of photoelectrons in the HTCC. The EB incorporates an algorithm that searches for electron candidates and ranks them based on particle characteristics, such as momentum. Once an electron candidate is selected, the absolute timing value from a layer of the Forward Time-of-Flight (FTOF) detector and the electron's path length to the FTOF are used to calculate the event start time, which corresponds to the electron's vertex position. The electron vertex time is defined as $t_0^r = t_r - t_{tof}$, where t_r represents the absolute time reported by an FTOF component, and t_{tof} denotes the calculated time-of-flight based on the reconstructed path length from the interaction point to the detector hit position divided by the speed of light. Although t_0^r is a good approximation for the time of the beam-target interaction, uncertainties associated with its calculation necessitate corrections to enhance timing-based particle identification. The correction method utilizes the RF (Radio Frequency) accelerator signal to further refine the calculation. The RF time, t_{RF} , measured in the TDC, includes a trigger jitter term, t_j . It is expressed as:

$$t_{RF} = M \times \delta t + t_j$$

where M is a large integer, δt is the separation time between CEBAF beam bunches, and t_j is the time jitter. A new term, Δt , is defined to quantify the difference between the vertex time, t_0^r , and the reported RF time, t_{RF} . By combining the previous formulas, Δt is expressed as:

$$\Delta t = (t_0^r - t_j) - M \times \delta t + C$$

where C represents the RF offset. As part of the calibration process, the C value is measured to ensure synchronization between the arrival of the beam bunch at the target and the TDC detection of the RF signal. Once the RF offset is subtracted, the extension of the production vertex must be considered due to the fact that the interaction point for each event is not a point-like target. This production vertex shift is accounted for in the term Δt_r as:

$$\Delta t^r = t_0^r - t_{RF} - \frac{z_t - z_0}{c} + m \times \delta t$$

where z_t and z_0 refer to the track production vertex and the center of the target, respectively. After quantifying Δt^r , the RF-correction term, Δt_{RF}^{corr} , can be calculated and subsequently used to finalize the event start time, t_0 :

$$\Delta t_{RF}^{corr} = \text{Mod}(\Delta t^r, \delta t) - \delta t/2;$$

$$t_0 = t_0^r - \Delta t_{RF}^{corr}.$$

This event start time, t_0 , is utilized by time-based tracking in the Drift Chamber (DC) to improve the reconstruction of charged particles. It is also incorporated in time-based particle identification for particles constructed in the event builder.

The identification of charged particles in the CLAS12 EB relies on various combinations of measured physical quantities from different subsystems. For electrons and positrons, the following conditions must be satisfied:

- Correct charge of the track
- Presence of clusters in the ECAL and the HTCC
- Minimum energy threshold in the PCAL (60 MeV)
- Number of photoelectrons greater than 2 in the HTCC
- ECAL sampling fraction falling within 5σ of the expected mean, which is energy-dependent

The identification of charged hadrons involves comparing the expected and measured vertex times when the mass of the particles is assigned. The deviation of the particle's vertex time from the event start time is calculated, and if it falls within 5σ of the expected value, the particle is identified accordingly. The calculation is described by the following equation:

$$\Delta t(i) = t_0 - \left[t_{TOF} - \frac{L}{\beta_i(p)} \right]$$

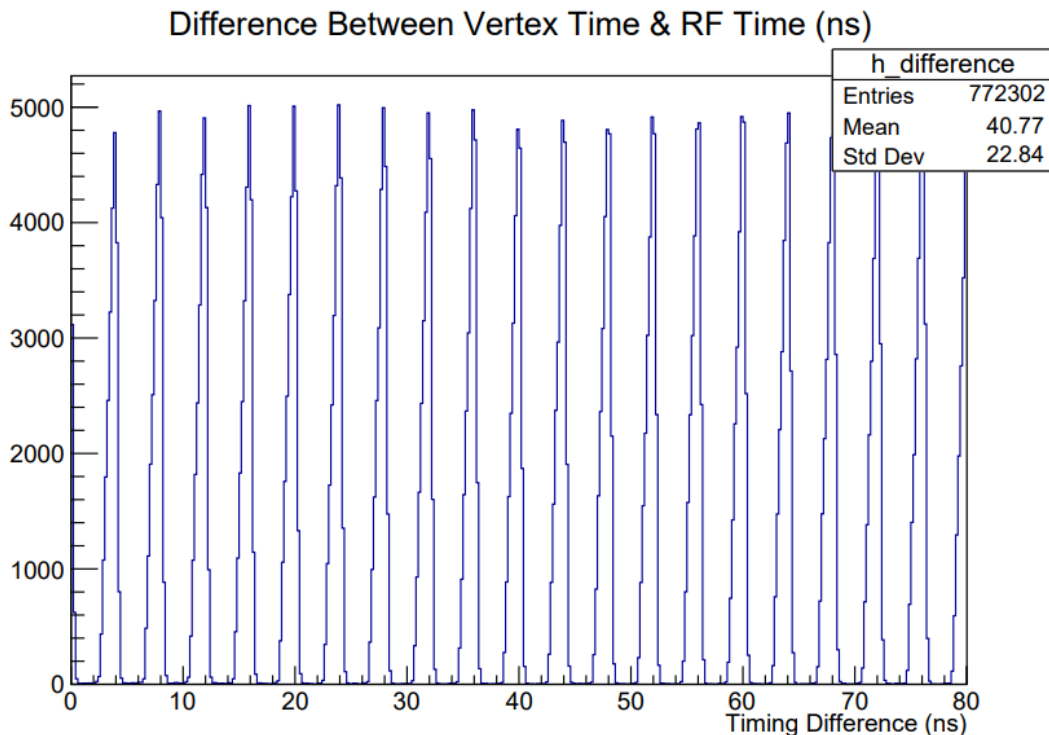


FIGURE 3.3: Comparison of Electron Vertex Time and Reported RF Time in the Fall 2018 RG-A dataset. This figure illustrates the comparison between the electron vertex time (t_0^e) and the reported RF time (t_{RF}) in the CLAS12 experiment. The electron vertex time represents the calculated time of the beam-target interaction, while the reported RF time serves as a reference for event timing. Understanding and addressing the differences between these two values are crucial for precise timing-based tracking and particle identification in CLAS12. Newton, 2021

where t_{FTOF} represents the time at which the particle intersects the time-of-flight detector plane.

Neutral particles, such as photons and neutrons, are also identified in the EB. For photons in the forward detector, the EB searches for clusters in the three layers of the ECAL that are not associated with any charged track in the DC. These clusters are assumed to originate from either neutrons or photons. To identify neutral particles, the distance from the production vertex to the cluster position in the ECAL and the cluster time are used to calculate the speed of the neutral particle. The EB assigns the photon ID to clusters with β greater than 0.9, while clusters with β less than 0.9 are assumed to be neutrons.

The CLAS12 EB heavily relies on the CCDB (CLAS Calibration Database) because several run-dependent variables affect particle identification. The CCDB provides constants specific to various detectors and subsystems, such as electron sampling fraction fit parameters, photon sampling fraction, user-determined software trigger, PID hypotheses, target position, detector hit position resolutions, detector timing resolutions, and Cherenkov counter photoelectrons.

In the COATJAVA reconstruction service within the CLARA framework, data is stored in the form of HIPO output banks. Each major subset of banks corresponds to an individual reconstruction service engine. The EB contains a specially designed network of banks that enable data analysts to associate particles, whose tracks can originate in the DC, Central Vertex Tracker (CVT), or Forward Tracker (FT), with their associated detector hits. This organization and association of data provide valuable insights into the characteristics of particles and their interactions in the CLAS12 experiment.

3.2 Analysis Framework

The research described in this thesis made use of different software that will be now briefly presented. The first part of this section will be centered on CLAS12 Offline Software and its tools, while in the second half, the focus will move to CLAS12ROOT and BruFit, two ROOT-based tools.

A description of the use of this software in the analysis process will be also shown in the following section.

3.2.1 CLAS12 Offline Software

CLAS12 Offline Software is a package developed by JLab and CLAS12 collaboration, composed of four different parts: GEMC, ClaRA, and COATJava software, along with the HIPO file format.

Using this package, it's possible to easily manage the simulation, reconstruction, and analysis processes of our data; more in detail:

- **Simulation:** GEMC, based on Geant4.
- **Reconstruction:** ClaRA, HIPO, COATJava.
- **Analysis:** COATJava.

P.N. COATJava description will be focused solely on the part of the tools useful for our analysis, leaving the references to the reader for further information.

For a full description of every aspect of the CLAS12 Offline Software, refer to De Vita, 2018 and Baltzell, 2018.

CLAS12 Monte-Carlo Job Submission Portal

Logged in as lbiondo

Configuration	<input type="text" value=""/>
Magnetic Fields	<input type="text" value=""/>
LUND File(s) (.txt) Location	<input type="text" value=""/>
Example: https://userweb.jlab.org/~ungaro/lund/	
Make sure to end the address with a "/"	
Background Merging	<input type="text" value="Not Available"/>
<input type="button" value="Submit"/> The submission will launch one job per LUND file.	

FIGURE 3.4: GEMC interface at JLab computer center webpage (https://gemc.jlab.org/web_interface/index.php). The configuration field is related to the selected run (Fall2018), while the following one refers to the usage of an in-bending or out-bending magnetic field.

GEANT4 & GEMC

In the last years, the demand for large-scale, accurate, and comprehensive simulations of particle detectors has sharply increased. This demand is driven by the always-growing size, complexity, and sensitivity of the detectors along with the availability of high-capacity and moderate-cost computer systems.

In response to this, the object-oriented simulation toolkit Geant4 has been developed, providing a wide-ranging set of software components that can be used in a variety of settings, from simple one-off studies of basic geometries to full-scale detector simulations.

In defining and implementing the software components, all aspects of the simulation process have been included:

- Geometry of the system
- Materials
- Fundamental particles
- Generation of primary particles
- Tracking of particles through materials
- Tracking of particles through electromagnetic fields
- Physics processes governing particle interactions
- Response of detector components
- Generation of event data
- Storage of events and tracks

LUND quantities description		
#	Header	Particles
1	No. of Particles Type	Index
2	Target Mass No.	Lifetime (ns)
3	Target Atomic No.	type (1 = Active)
4	Target Polarization	Particle ID
5	Beam Polarization	Parent ID
6	Beam Type (11/22)	First Daughter ID
7	Beam Energy	Momentum X (GeV)
8	Interacted Nucleon ID	Momentum Y (GeV)
9	Process ID	Momentum Z (GeV)
10	Event Weight	Particle Energy (GeV)
11		Particle Mass (GeV)
12		Vertex X (cm)
13		Vertex Y (cm)
14		Vertex Z (cm)

TABLE 3.1: LUND files value description. Please note that this is the CLAS12 convention, and users can reassign any of the following values.

- Visualization of the detector and particle trajectories
- Capture for subsequent analysis of simulation data

Geant4 was designed and developed by an international collaboration, formed by cooperating institutes, universities and experiments. For a more detailed description of Geant4, please refer to Agostinelli et al., 2003.

The introduction of this tool was necessary, as GEMC, a Geant4-based software, has been widely used in the analysis process presented in this thesis.

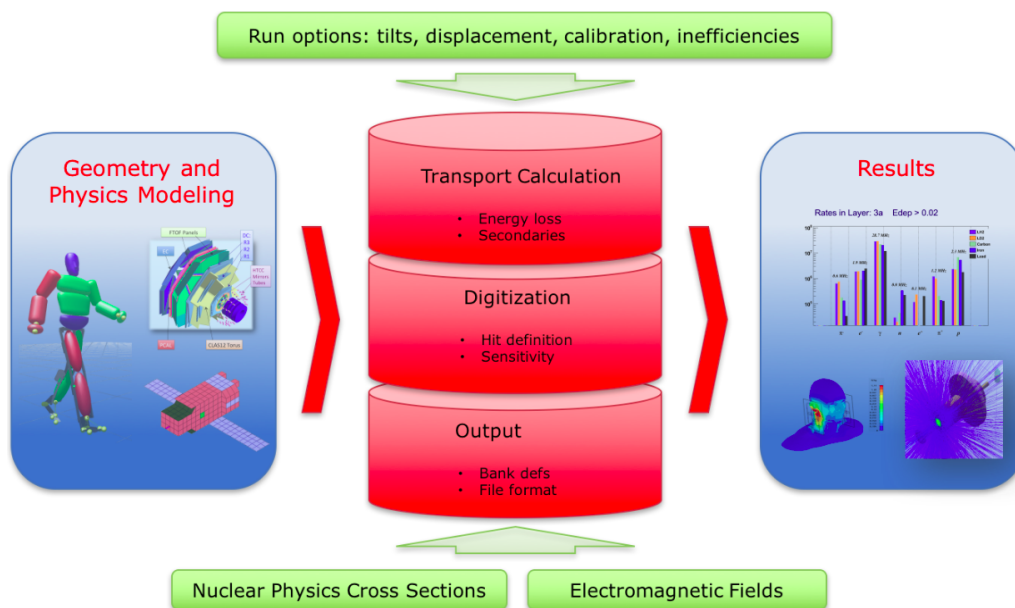


FIGURE 3.5: GEMC architecture. Ungaro, 2020a

GEMC (GEant4 MonteCarlo) is a C++ framework that uses Geant4 to simulate the passage of particles through matter. It provides the independent geometry description and the digitization algorithms for all the CLAS12 detectors, an easy interface to build and run experiments, and the possibility to import CAD and GDML projects.

It also supports background merging based on real data recorded from random triggers, in order to study efficiency/resolution as a function of luminosity.

GEMC provides multiple levels of accuracy, depending on how much time can be spent on the process: 200-500 ms/event it's the speed achieved for a remote single core processing requesting multi-particle final states with full transport and digitization.

During the analysis described in this thesis, GeMC has been widely used to obtain multiple simulated datasets comparable with the reconstructed data thanks also to the web interface provided by JLAB (https://gemc.jlab.org/web_interface/index.php), as seen in 3.4, which gives a fast and easy solution for GeMC usage. Further description of GEMC will be given in the next section.

In order to be understood by GeMC, input data should be in LUND format; an example of the latter can be seen in the following extract.

```

1 | 4 1 1 0 0 11 10.6 1 1 0.24E-2
2 | 1 -1 1 11 0 0 -0.983 0.0981 9.6502 9.7007 0.0005 0 0 -0.8072
3 | 2 1 1 2212 0 0 0.7333 0.1126 0.6391 1.356 0.938 0 0 -0.8072
4 | 3 0 1 111 0 0 0.2498 -0.2107 0.2808 0.4515 0.1349 0 0 -0.8072
5 | 4 0 1 22 0 0 -0.0001 0 0.0299 0.0299 0 0 0 -0.8072

```

LUND is a text format composed of a header and N lines (one for each particle of the event), describing the event and particle property. Each one of these quantities is reported in Table 3.1. For more detailed information about the LUND file, please refer to Ungaro, 2019.

GEMC Detailed Description

The Geant4 Monte-Carlo (GEMC) package is a powerful tool used to simulate the behavior of particles as they pass through the various detectors of the CLAS12 experiment which, as previously stated, it's composed of multiple detector subsystems and two superconducting magnets, providing wide coverage for detecting charged and neutral particles resulting from the interaction between the electron beam from the JLab CEBAF accelerator and a target positioned at the center of the spectrometer.

As explained in chapter 2, Forward Detector in CLAS12 comprises six sectors and includes Drift Chambers for tracking charged particles, as well as other detectors for particle identification, such as threshold Cherenkov Counters and Ring-Imaging Cherenkov Counters, scintillator-based time-of-flight hodoscopes, and electromagnetic calorimeters. In the target region, there is a 5 T superconducting solenoid that surrounds a central tracker composed of silicon and Micromegas detectors, along with subsystems for particle identification, including a time-of-flight scintillation counter barrel and a neutron detector. This configuration is known as the Central Detector. Additionally, the CLAS12 Forward Tagger extends the kinematic coverage for detecting electrons and photons at specific polar angles.

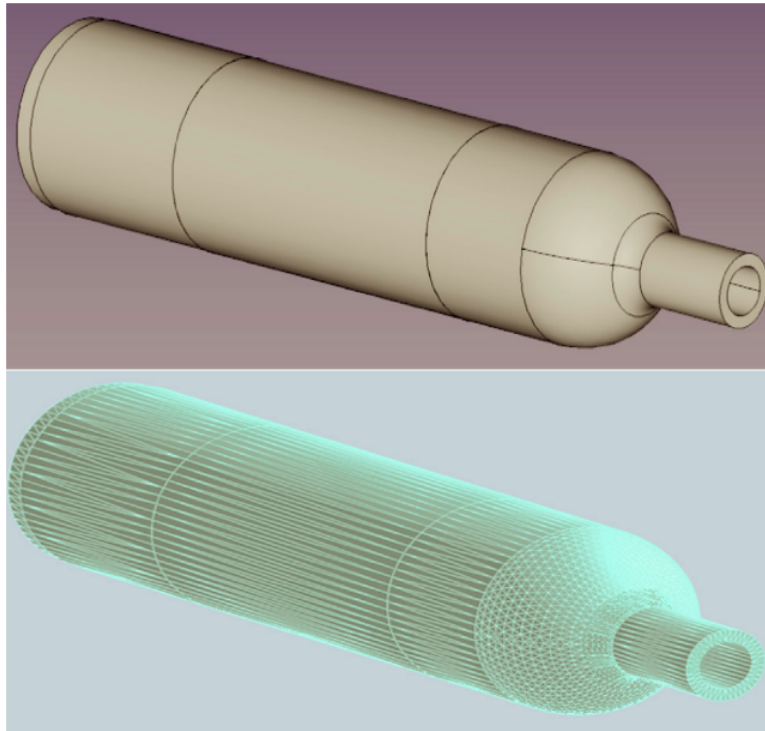


FIGURE 3.6: Illustration of a geometric volume derived from a STEP file and tessellated in GEMC. The depicted volume corresponds to the target scattering chamber. The upper part showcases the Computer-Aided Design (CAD) representation as seen in the engineering model, while the lower part displays the resulting tessellation achieved through GEMC. Ungaro, 2020a

To accurately simulate the passage of particles through the CLAS12 detectors, the GEMC package is utilized. GEMC is a C++ framework built upon Geant4, a versatile toolkit used for simulating particle interactions with matter. GEMC provides an application-independent description of the experiment's geometry and offers an intuitive interface for constructing and running simulations. It supports the importation of CAD or GDML files to define the geometry of the detectors.

Simulation parameters, such as geometry, materials, mirrors, physics lists, database constants, digitization settings, and electromagnetic fields, are stored in external databases and are utilized to construct Geant4 objects dynamically during runtime. This enables the flexible configuration of the simulation. The GEMC framework organizes these parameters and facilitates the simulation of particle trajectories through materials and sensitive regions of the detectors. Hits produced by the particles interacting with the detector materials are digitized using user-defined plugins and collected in customizable outputs.

GEMC incorporates the implementation of various CLAS12 systems into the simulations. These systems include different CLAS12 target configurations (liquid hydrogen, liquid deuterium, and solid targets), trackers such as the Silicon Vertex Tracker (SVT) and Micromegas Tracker (MM), time-of-flight systems like the Central Time-of-Flight System (CTOF) and Forward Time-of-Flight System (FTOF), particle identification detectors including the High Threshold Cherenkov Counter (HTCC)

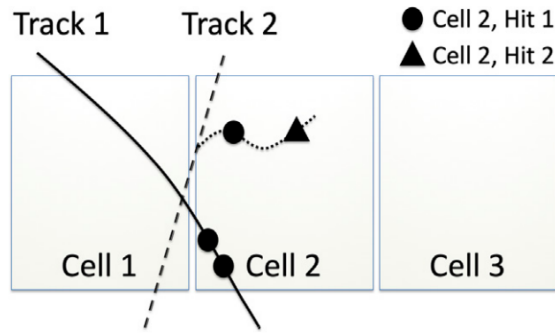


FIGURE 3.7: The algorithm employed for defining GEMC hits is depicted in the figure. In this scenario, the sensitive element Cell 2 experiences a hit from three particles, comprising two primary particles and one secondary particle. The Geant4 steps are explicitly represented using circle and triangle symbols. Notably, the circle steps originating from both primary track 1 and the secondary particle from track 2 fall within the defined time window, consequently belonging to the same GEMC hit denoted as 'Cell 2, Hit 1'. Conversely, the lone triangle step generated by the secondary particle from track 2 occurs after the time window, rendering it part of a distinct GEMC hit designated as 'Cell 2, Hit 2'. Ungaro, 2020a

and Ring Imaging Cherenkov Detector (RICH), calorimeters such as the Electromagnetic Shower Calorimeter (EC) and Pre-Shower Calorimeter (PCAL), and other essential detectors like the Central Neutron Detector (CND) and Drift Chamber System (DC). The simulation also accounts for the CLAS12 Forward Tagger, the beamline, and the superconducting magnets.

While the simulation may not incorporate certain elements of the CLAS12 mechanical design, such as electronics, support structures, and additional hardware, it does include all elements necessary for accurately tracking particles along their trajectories within the detectors. Moreover, the simulation accounts for selected hardware to reproduce beam-related rates in the detectors, prioritizing volumes near high background areas and sensitive detectors.

To enhance the predictive capability of the simulation, hits generated by simulated events can be merged with real random trigger data, which includes the actual background rates observed in experimental data. This merging process allows for a more accurate representation of beam data and improves the simulation's ability to make predictions.

The CLAS Collaboration has extensively used GEMC for the design, optimization, calibration, and performance evaluation of the CLAS12 detectors. GEMC has played a vital role in assessing the performance of detector components, determining rates, current values for photomultiplier tubes, radiation doses, and ensuring the survivability of detectors throughout the spectrometer's expected operational lifetime. Furthermore, GEMC enables the calculation of CLAS12 acceptance, accounting for detector response, geometrical acceptance, and tracking efficiency, which are crucial for achieving the experiment's scientific objectives. For a better understanding of the processes behind this evaluation, please report to Ungaro, 2020a.

The geometric information and system materials are stored in external databases, which can be in the form of MySQL tables or text files that mimic MySQL tables. The databases can be created using different methods, including the GEMC native API (Perl or Python), JAVA algorithms used by both simulation and CLAS12 event reconstruction software, CAD (STL, PLY formats), and GDML, C++ plugins (not utilized in CLAS12). The repositories for GEMC native API and CLAS12 geometry

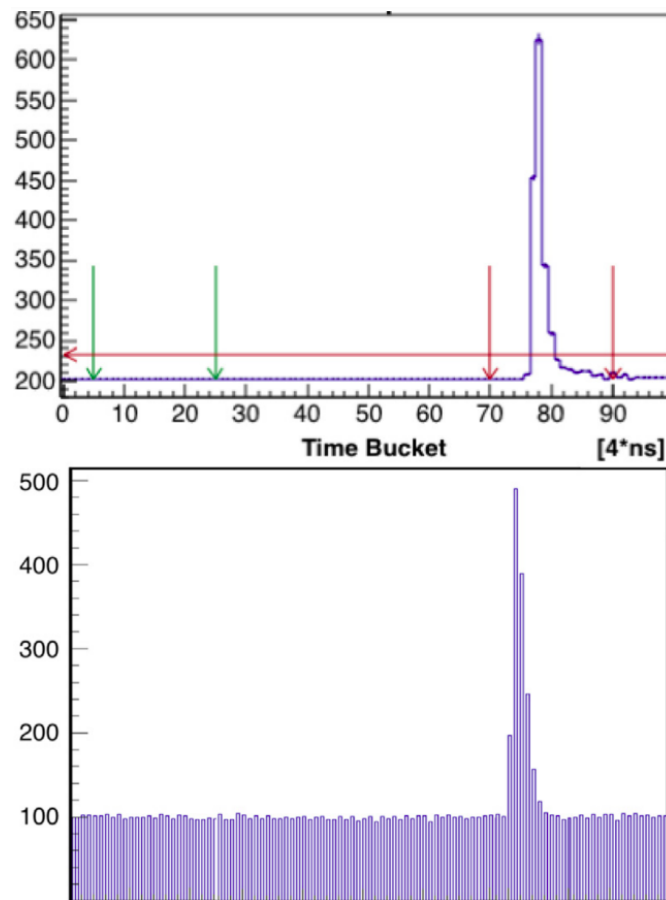


FIGURE 3.8: Top: An illustrative example of the FADC digitized output obtained from the CLAS12 EC PMTs during the Spring 2018 data run. The CLAS12 DAQ system plays a critical role in capturing and preserving relevant information. The 400 ns time window is saved if at least one signal sample exceeds the predefined threshold (horizontal line). The integral signal ADC is calculated by summing the output within the indexes marked by the right arrows, strategically positioned before and after the threshold crossing. The pedestal, essential for baseline characterization, is computed by averaging the signal between the left arrows. The DAQ parameters, including the acquisition limits for the pedestal and the relative position of the signal integration limits, are meticulously adjusted before each run.

Bottom: Simulation of the EC FADC signal for optimizing the CLAS12 trigger system. Signal shape is generated by summing pulse functions from Geant4 steps, weighted by the energy deposition parameters estimated from experimental data. These simulated signals serve as a powerful tool for tuning the trigger system FPGA algorithms, maximizing the efficiency of the CLAS12 trigger electronics.

This comprehensive study provides insight into the intricate intricacies of the CLAS12 data acquisition process and the optimization of the trigger system. The detailed analysis of the FADC digitized output and parameter adjustments showcases the adaptability of the DAQ system to experimental conditions, enabling precise data acquisition. Additionally, the integration of simulated EC FADC signals demonstrates their significance in refining the trigger system algorithms, resulting in enhanced performance and efficiency for the CLAS12 experiment. Ungaro, 2020a

code source can be found on the CLAS12 tags portal.

The Geant4 sensitive volumes are linked to GEMC identifiers that contain hierarchical information such as mother volumes and volume copy numbers. Each detector is associated with a time quantity to simulate the readout electronic time window. A GEMC hit comprises a series of Geant4 steps within the designated time window and identifier. A process ID method can be implemented to modify or add GEMC identifiers to each Geant4 step. This is used in cases where multiple outputs are generated from a single hit, such as when a paddle is hit with two outputs produced due to the presence of a PMT at each end of the scintillator. The algorithm is illustrated in Fig. 3.7.

GEMC supports the emulation of the CLAS12 data acquisition system (DAQ). The CLAS12 data is expressed as specific collections of numbers called "banks." Each detector channel can be associated with banks containing information such as the Flash Analog-to-Digital Converter (FADC) signal, Time-to-Digital Counter (TDC) value, and extrapolated values of ADC and TDC for each hit. The FADC and TDC signals are programmed into Field Programmable Gate Arrays (FPGA) to generate triggers for events. An example of a simulated vs. data FADC signal is given in Fig. 3.8.

The detectors are associated with C++ digitization routines at runtime, allowing independent development from the core code. Different types of digitization output structures are implemented, including integrated (one bank per hit), step-by-step (one bank per Geant4 step), voltage (analog signal vs. time), and FADC (simulating the CLAS12 data acquisition system).

The GEMC output is available in two formats: text (ASCII) and EVIO, which is the Jefferson Lab data acquisition format. Utilities are used to convert the EVIO format into ROOT for data analysis. The output includes various banks such as header, generated particle information, generator extras, detector truth information, detector digitized information, detector voltage vs. time, and ancestors (hierarchy of primary and secondary particles).

The performance of CLAS12 simulations is measured by comparing predicted background rates with actual experimental rates. Benchmarks are conducted for each detector geometry and digitization routine. The drift chamber hit occupancy and rates in other CLAS12 detectors have been compared with data, showing good agreement.

The event simulation rate in GEMC varies depending on the type of track. For single meson tracks in the forward region, the event rate is around 10 Hz, while electron simulation takes longer due to additional simulations in the EC and PCAL calorimeters and Cherenkov photon production in the HTCC and LTCC, resulting in an average rate of approximately 5 Hz.

A quantitative study was performed to determine the event rate for three particles: a 7 GeV electron between polar angles 15° and 25°, a GeV photon between polar angles 15° and 25°, and a 2 GeV proton at $\theta = 90^\circ$. The final event rate for these three particles in the complete CLAS12 setup is 1.7 Hz. Simulations that include complete beam-target interactions using the nominal luminosity of $10^{35} \text{ cm}^{-2} \text{ s}^{-1}$ utilize 124000 electrons per event and take between one and two minutes to complete, depending on the CPU type and available memory.

GEMC Forward Tagger Digitization

As detailed in chapter 2, the FT is an essential component of the experimental setup, designed to enhance particle identification capabilities and facilitate the detection of

specific particles in the CLAS12 detector. This section focuses on the implementation in Geant4 Monte Carlo simulation (GEMC) of the FT subsystems, namely the tracker (FT-Trk), hodoscope (FT-Hodo), and calorimeter (FT-Cal), along with their integration of the CAD engineering model. For the Forward Tagger (FT) system, accurate digitization of signals is crucial for extracting meaningful information from energy depositions. This section focuses on the digitization process for the FT-Trk, FT-Cal, and FT-Hodo subsystems, detailing the conversion of energy depositions into ADC values, timing information, and the incorporation of smearing effects to ensure realistic simulations.

- **FT-Trk Digitization:** The digitization process for FT-Trk aims to provide the ADC value by calculating the total energy deposited after considering hit sharing effects. However, it is important to note that the FT-Trk output does not include timing information. The conversion from energy deposition to ADC value in the FT-Trk subsystem relies on accurately quantifying the total deposited energy.
- **FT-Cal Digitization:** For FT-Cal hits, the energy deposited by particles in the crystals undergoes a two-step conversion process. Firstly, the energy deposition is converted to charge at the end of the electronics chain, which consists of an avalanche photodiode (APD) and a preamplifier. This conversion is based on the measured charge resulting from cosmic rays that deposit a known energy in the crystals. Subsequently, the charge is converted to an ADC value using the FADC conversion factor.

To account for uncertainties and variations inherent in the digitization process, a smearing effect is applied to the final ADC values. This smearing incorporates the Poisson distribution of photoelectrons produced by the photosensor, as well as the Gaussian noise of the photosensor and preamplifier. Notably, all relevant parameters, such as the number of photoelectrons per MeV of energy deposited, the RMS width of the APD noise, and the preamplifier input noise, have been meticulously tuned to match the experimental data.

- **FT-Hodo Digitization:** A similar approach is adopted for processing FT-Hodo hits. The digitization of FT-Hodo hits involves the conversion of deposited energy to charge, followed by the conversion of charge to ADC values using silicon photomultipliers (included in the simulation). In this case, the smearing effect accounts solely for the Poisson distribution of the measured number of photoelectrons. This distribution dominates due to the relatively small number of photoelectrons per MeV of energy deposition.
- **Timing Information:** The TDC (Time-to-Digital Converter) values for FT-Cal and FT-Hodo hits are determined based on the timing of energy depositions. For FT-Cal hits, the TDC calculation takes into account the speed of scintillation light in the crystal and the distance to the photosensor. This calculation assumes a known time-to-TDC conversion factor. A Gaussian smearing effect is added to the resulting TDC values, considering a fixed RMS resolution derived from experimental measurements.

Similarly, the TDC values for FT-Hodo hits are derived from the timing of specific energy depositions. A fixed offset is applied before the conversion from time to TDC, and Gaussian smearing is introduced. As with previous cases, all relevant parameters have been tuned to match the observed detector response.

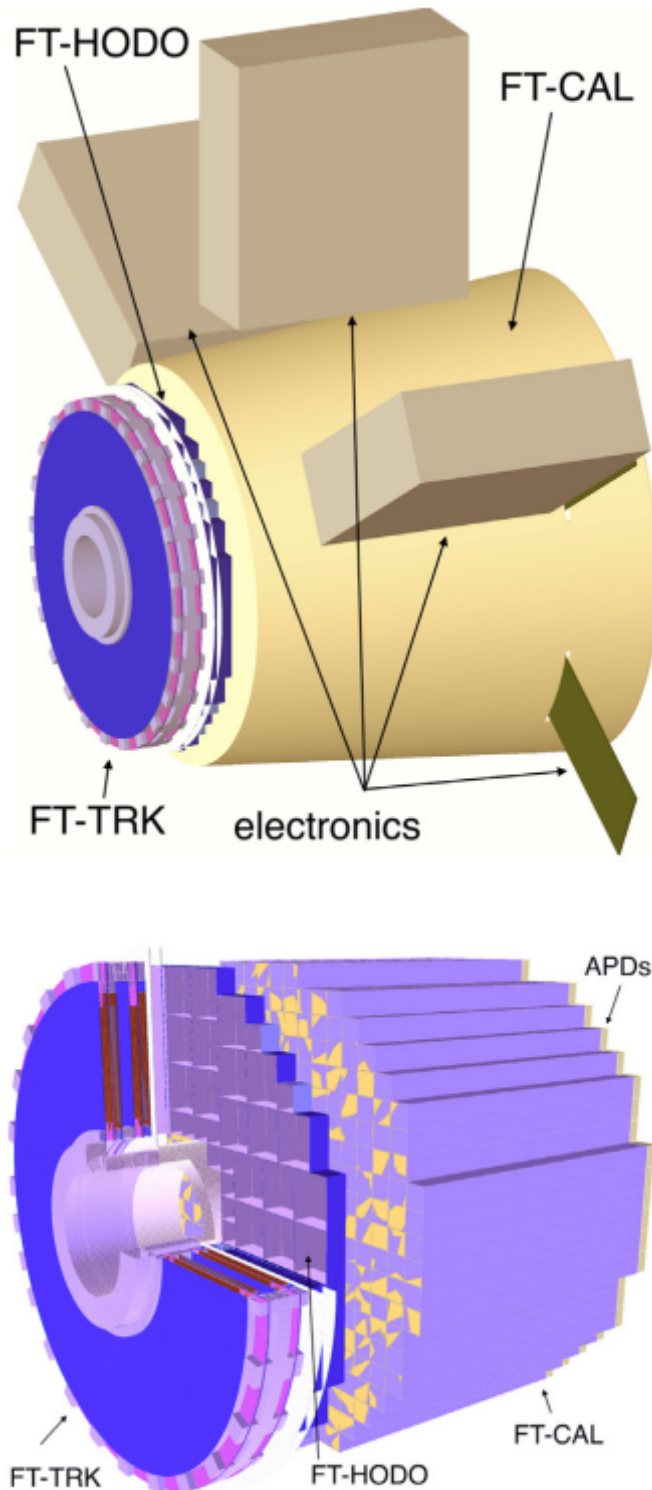


FIGURE 3.9: Top: The implementation of the Forward Tagger (FT) detector in the Geant4 Monte Carlo simulation framework (GEMC). The boxes surrounding the FT-Cal represent the electronics associated with the detector. Bottom: A detailed view of the three subsystems comprising the FT detector. When viewed from the perspective of the incident beam (coming from the left), the FT-Trk subsystem is represented by the disks, followed by the FT-Hodo scintillators located just behind the tracker. Finally, the FT-Cal crystals are observed as the last component in the sequence. This illustration provides an overview of the FT detector's arrangement and helps visualize the positioning and roles of its individual subsystems in the context of particle detection and analysis within the CLAS12 experiment. Ungaro, 2020a

HIPO Files Benchmarks and Comparison			
Data Format			Read Time
Format	Data Type	Size	Seconds
ROOT	DST Summary	1.0 GB	38.75
ROOT	Full Data	1.6 GB	65.92
HIPO	DST Summary	1.0 GB	6.12
HIPO	Full Data	1.8 GB	5.82

TABLE 3.2: Benchmarks and comparison of ROOT and HIPO files. *DST Summary* refers to 10^7 simulated events, while *Full Data* is data from a detector containing both RAW and reconstructed data banks. In the *Full Data* sample, a single event is much larger in size if compared to other formats, so larger portions of the file are being copied at once, resulting in smaller reading time. In *DST Summary* sample, 10^7 small summary tables are being copied resulting in longer processing time. Gavalian, 2018

- **Time Windows:** The time window for the FT-Trk subsystem is set to 132 ns. Within this time window, all Geant4 steps occurring in the same strip and time window are collected as one hit. On the other hand, the time windows for the FT-Hodo and FT-Cal subsystems are both set to 400 ns. Within these time windows, all Geant4 steps occurring in the same paddles and time window are collected as one hit for each system.

By meticulously implementing the digitization process and incorporating appropriate smearing effects, the simulated ADC values, timing information, and other relevant variables closely resemble the behavior observed in real experimental conditions. These realistic simulations provide a solid foundation for further analysis and interpretation of FT system data.

HIPO files

HIPO files are developed with the focus of providing structured data for physics analysis. The first step in the production of a HIPO is starting with a specific type of file, called File: this kind of format, formed by segmented chunks of data that are grouped and compressed depending on the desired workflow, keeps growing in size sequentially until the group of data reaches predefined chunk size (set as default at 8 MB, but can be switched to any value).

The chunk, which is called *record*, is then indexed in order to speed up the reading process, compressed, and written to output. After this, the LZ4 algorithm is used to compress the records.

The HIPO file format can be used with various data serialization formats and got also a huge increase in reading speed if compared to the ROOT files usually used in this kind of analysis, as shown in Table 3.2. More information about the HIPO files benchmarks, production, and applications can be found at Gavalian, 2018.

Data Structure and Banks

Data inside the HIPO files are organized in a way that every piece of information can be easily accessed via the given software (CLAS12ROOT, CoatJava, etc.), and stored in what so-called *Banks*. Every HIPO file stores a non-fixed number of recorded events, each of which is filled with the Banks, carrying the knowledge of what happened in the registered occurrence.

There are many different Banks, and every one of them got its functions and options that may be related to the detector providing the information, to a fixed particle or a run, etc.

Some examples will be briefly presented in Listing 3.1, showing some of the Banks and functions used in the analysis; an exhaustive list of the Banks and their functions can be found in Baltzell, 2019.

Information from the Banks can be accessed by selecting the desired particle (numbered by the i index), detector, subdetector, and physical quantity; an example of this process is shown in line 11 of the previously cited listing.

It's important to note that not every option used in the last case has to be always used, as can be seen in lines 15 and 19 of the same code. The example shows that there are some information that may be accessed without the declaration of a specific particle, and particle property that could be requested without declaring a precise detector.

Where needed, the detector will be automatically selected according to the particle detection region (FT, FD, CD); in more precise detail:

- **FT:** *Time* and *Path* of the particle comes from FTCAL, while *DeltaEnergy* from FTHODO.
- **FD:** *Time*, *Path* and *DeltaEnergy* of the particle comes from FTOF1B, FTOF1A, FTOF2 or PCAL, in a given order of preference.
- **CD:** *Time*, *Path* and *DeltaEnergy* of the particle comes from CTOF, or from the CND if the aforementioned is not available.

A description of the commands and functions shown in Listing 3.1 and not related to the Banks will be given in section 3.2.3. Note also that every option and Bank presented in the reference can be also used to access the data by CoatJava, as will be briefly shown in the dedicated section.

LISTING 3.1: CLAS12 Banks and Banks options examples.

```

1 //Opening file.
2 clas12reader c12("my/hipo/file.hipo");
3
4
5 //Looping over events.
6 while(c12.next())
7 {
8     // Defining a std::vector of particles from the current event.
9     auto particles = c12.getDetParticles();
10
11     //Requesting #i particle detection time (ns) from the Forward
12     //Tagger Calorimeter and energy (GeV) from the Forward Tagger
13     //Hodoscope.
14     double FTCTime = particles[i]->ft(FTCAL)->getTime();
15     double FTHEnergy = particles[i]->ft(FTHODO)->getEnergy();
16
17     //Requesting start time and event number for the current event.
18     double StartTime = c12.event()->getStartTime();
19     int EventNo = c12.runconfig()->getEvent();
20
21     //Requesting #i particle detection time (ns) and released energy
22     //(GeV).
23     double PartTime = particles[i]->getTime();
24     double dE = particles[i]->getDeltaEnergy();

```

```
22 ||  
23 || }
```

CoatJava

CoatJava is a framework developed by JLAB and CLAS12 collaboration, and used during reconstruction and analysis processes; it includes detectors geometry, CCDB (Calibration Constant Database) and other database, input/output interfaces, FastMC (a fast Monte Carlo simulator that uses only the part of detector object of interest instead of simulating the whole apparatus), etc. More in detail:

- **Input/Output.**
 - Raw data reader and decoder (from EVIO format with composite bank structure).
 - HIPO file production (record based and compressed).
 - Interface for EVIO and HIPO files reading.
 - Data processing interface for calibration and monitoring.
- **Database.**
 - Calibration constants and geometry definitions.
 - Caching algorithm of database constants for reconstruction and calibration.
- **Geometry.**
 - Geometry package used by simulation, reconstruction and event display.
 - Ability to import CAD files (linked with Geant4).
 - Detector visualization package, with callbacks and automated occupancy display.
- **Reconstruction.**
 - Reconstruction engine class to develop ClaRA reconstruction services.
 - Automatic detector initialization from database.
- **Analysis Tools.**
 - Event selector.
 - Fiducial cut provider.
 - Fast-MC.
- **Plotting Packages.**
 - Full plotting package based on gRoot library.
 - Integrated freehep-jminuit library for fitting.

Using the CoatJava command "*eviodump*" on a terminal, is possible to investigate and process the data written inside the HIPO files. As can be seen from Fig. 3.10, every single event can be visualized and, from there, it is possible to access all the available banks.

```

***** EVENT # 3 *****
at      16 : goup =      300, item =   31, type =  11, size =   473
at     497 : goup =      300, item =   40, type =  11, size =   748
at    1253 : goup =    10000, item =   11, type =  11, size =    38
at    1299 : goup =      300, item =   32, type =  11, size =  1261
at    2568 : goup =      300, item =   38, type =  11, size =   128
at    2704 : goup =      300, item =   35, type =  11, size =   440
at    3152 : goup =    21800, item =   12, type =  11, size =   189
at    3349 : goup =      300, item =   36, type =  11, size =    30
at    3387 : goup =      300, item =   34, type =  11, size =   200
at    3595 : goup =      300, item =   42, type =  11, size =   198
at    3801 : goup =      300, item =   41, type =  11, size =    12
at    3821 : goup =      300, item =   30, type =  11, size =    42

Choose (n=next,p=previous, q=quit), Type Bank Name or id : n

```

FIGURE 3.10: CoatJava event visualization example. More information on the usage of the software can be found at Baltzell, 2018.

3.2.2 ROOT

ROOT is an Object Oriented framework for large-scale data analysis, and was the most used software during the research; it is written in C++ and composed of a C++ interpreter, an efficient hierarchical OO database, advanced statistical analysis and visualization tools, and other useful instruments. ROOT can be used via a graphical user interface or the command line and its command and scripting language is C++ (using the interpreter). More information about it can be seen in detail in Brun and Rademakers, 1997 or at the webpage root.cern.

3.2.3 CLAS12ROOT

CLAS12ROOT is a specific tool developed for the CLAS12 analysis and based on C++ and ROOT; it can analyze files of a peculiar file extension (.hipo) and adds custom-made commands to the basic ROOT libraries, in order to streamline the analysis process. CLAS12ROOT has been developed at Jefferson Laboratory and more information about it can be found at Glazier, 2019b.

Custom Classes and Methods

CLAS12ROOT custom classes and their methods have been widely used to interact with data, being intuitive and powerful tools capable of rapidly extracting the required information. A better description of these is given in appendix C.

3.2.4 RooFit

RooFit library is a toolkit for physics analysis, used for modeling the expected distribution of events with the aim of creating plots, performing unbinned maximum likelihood fits, or generating "toy Monte Carlo" samples.

RooFit can model the 'event data' distributions, where each event is a discrete occurrence in time, and has one or more measured observables associated with it.

Density functions (PDF) are the modeling language for such distributions, and describe the probability density of the distribution of the observables x in terms of

function in parameter p . Unit normalization with respect to all observables and positive definiteness is the defining property of PDFs, which, thanks to an intuitive coding language, are capable of introduce and describe complex correlations between observable.

BruFit

BruFit is an event-based maximum likelihood fitting package built on RooFit; information and tools about it can be found at Glazier, 2019a. The purpose of this package is to add to the RooFit package a way to allow an analysis of hadronic physics scattering reactions.

The main BruFit feature is the PDF class *RooHSEventsPDF*, which calculates the normalization integrals from CLAS12 detectors simulations. This also allows the correction of detector acceptances necessary for the extraction of the requested observables.

Another custom class, *RooComponentsPDF*, provides the caching of these integrals for fast evaluation when the PDF is a sum of products.

Weights extracted in this way can be used in the fits and can be created using the *RooStats sPlot* class.

sPlot

sPlot is the core BruFit feature in the presented analysis. This feature offers a novel approach for investigating a composite data sample composed of multiple sources of events merged into a single dataset. The events in the kind of sample that may be investigated with sPlot are characterized by a set of variables, which can be divided into two distinct components. The first component comprises variables for which the distributions of all event sources are known, collectively referred to as the "discriminating variable." The second component consists of variables for which the distributions of certain event sources are either truly unknown or assumed to be so, collectively referred to as the "control variable."

The proposed technique enables the reconstruction of the distributions of the control variable for each individual event source, independently and without relying on any prior knowledge of these distributions. The objective is to utilize the available information regarding the discriminating variable to infer the behavior of the individual event sources in relation to the control variable. A fundamental prerequisite for the successful application of the sPlot technique is that the control variable is uncorrelated with the discriminating variable.

The development of the sPlot technique is contextualized within the framework of a data sample analyzed using a maximum likelihood method that leverages the discriminating variable. By leveraging this methodology, the sPlot technique offers a valuable tool for disentangling the contributions of different event sources and obtaining insights into the behavior of each source with respect to the control variable.

A common method used to extract parameters from a data sample, and used in sPlot, is the maximum likelihood method.

An extended likelihood analysis is conducted on a composite data sample that merges multiple event species, comprising both signal components of interest and background components that are irrelevant to the analysis. The logarithm of the likelihood function, denoted as L , is expressed as follows:

$$L = \sum_{e=1}^N \ln \left\{ \sum_{i=1}^{N_s} N_i f_i(y_e) \right\} - \sum_{i=1}^{N_s} N_i \quad (3.1)$$

where:

- N is the total number of events in the data sample,
- N_s represents the number of event species present in the data sample,
- N_i denotes the expected average number of events for the i th species,
- y represents the set of discriminating variables,
- f_i is the Probability Density Function (PDF) corresponding to the discriminating variables for the i th species,
- $f_i(y_e)$ indicates the value taken by the PDF f_i for event e , associated with the set of values y_e for the discriminating variables,
- x denotes the set of control variables, which are not included in the aforementioned expression for L .

The logarithm of the likelihood function, L , is a function of the yields N_i for each species, as well as any implicit free parameters that are employed to adjust the PDFs according to the data sample. By maximizing the log-likelihood function, the optimal values for these parameters, as well as the event yields N_i , are determined.

To ensure the reliability of such a data sample analysis, it is crucial to utilize a comprehensive list of event sources and accurately describe all the Probability Density Functions (PDFs) denoted as f_i . While assessing the goodness-of-fit based on the maximum value obtained for L is one approach, it is often insufficient. A complementary method involves exploring the data sample further by examining the distributions of control variables. If the distributions of these control variables are known for at least one event source, it becomes possible to compare the expected distribution for that specific source with the distribution extracted from the data sample. However, in order to do so, it is necessary to disentangle the contribution from the source under scrutiny from the overall distribution of the entire data sample.

In some cases, the PDF may be known for all event sources associated with a control variable. This control variable can be obtained, for example, by removing one of the discriminating variables from the set y and performing the maximum likelihood fit again, treating the removed variable as a control variable x . Alternatively, a discriminating variable may have known distributions for all event sources, yet it may not significantly improve the accuracy of the fit and is therefore not included in the set y for the sake of simplicity.

To access the distributions of control variables, a common method involves applying cuts designed to enhance the contributions of specific event sources (typically signal species) to the data sample. By enforcing this enhancement, the distribution of x for the reduced data sample can be compared to a Monte Carlo simulated distribution to evaluate the quality of the fit. However, this approach often yields unsatisfactory results for two reasons. Firstly, it can only be applied if the signal exhibits distinct features that can be distinguished from the background. Secondly, due to the applied cuts, a substantial fraction of signal events may be lost, while a significant portion of background events may still remain. Consequently, the resulting

data distribution pertains to a reduced subsample, where statistical fluctuations or true anomalies cannot be unambiguously attributed to either the signal or the background. Misinterpretation of an anomaly in the distribution of x , originating from the signal, as a benign background fluctuation is a possible pitfall.

The sPlot formalism here shown, which is further explained in Pivk and Le Diberder, 2005, aims to provide a convenient method for deconvolving the overall distribution of a mixed sample of events in a control variable x into sub-distributions representing the various event species composing the sample. It is a statistical technique that enables the retention of all signal events while eliminating all background events, while simultaneously preserving the statistical uncertainties per bin.

Considering a variable x that depends on the discriminating variables y used in a fit, it is possible, by performing a fit to determine the yields N_i for all species, knowing the probability density functions (PDFs) f_i and the values of N_i , to naively define a weight for all events, denoted as $P_n(y_e)$ described as follows:

$$P_n(y_e) = \frac{N_n f_n(y_e)}{\sum_{K=1}^{N_s} N_k f_k(y_e)}. \quad (3.2)$$

Using this weight, we can construct the x -distribution \tilde{M}_n by summing over the events e that fall within the x -bin centered on \bar{x} with a total width of δx . Specifically, $N_n \tilde{M}_n(\bar{x}) \delta x$ is obtained by histogramming the events and assigning them weights according to equation 3.2.

On average, this procedure reproduces the true distribution $M_n(x)$. By incorporating the weights based on the PDFs and yield values, it is possible to obtain an estimate of the x -distribution that accounts for the underlying physics and statistical fluctuations of the data.

In the following described processes, the sPlot method has been crucial to separate the background and the proton missing mass peak resulting from the π^0 exclusive electroproduction. For further clarification about this process, please refer to the following section.

3.3 Analysis Process

The analysis shown in this thesis has been carried out using all the tools presented so far and applied on the *Fall2018* dataset.

The Fall2018 data are part of the result of the first CLAS12 experiment fulfilled by *RG-A* (Run Group - A) during the spring and fall of 2018; the experiment gathered data directing a 10.56 GeV electron beam on a liquid hydrogen target and using two different magnetic field configurations for the torus (*in-bending* and *out-bending*).

Data are located on the JLab server and can be accessed via ssh; treating such a huge amount of data, though, it's a problem itself, and finding a solution to it was the first step of the analysis process.

The solution was achieved via a remotely launched bash script, whose purpose was to run a series of C++ code on every file of the dataset. The aim of the codes was to build a series of smaller files, following different filtering conditions; more in detail:

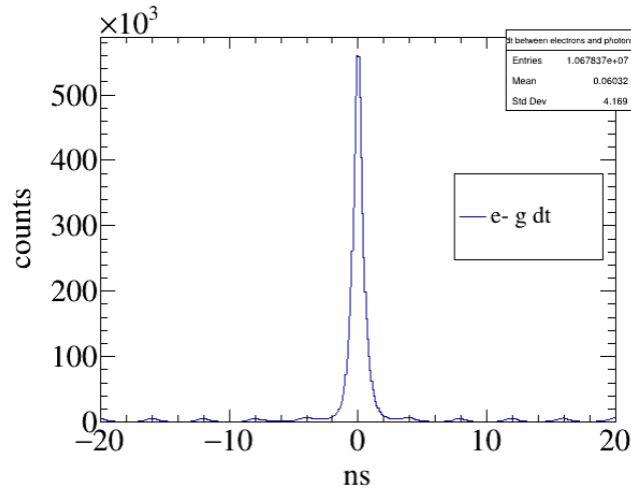


FIGURE 3.11: Electron-photon time correlation. The peak of the events is located at 0 ns with $\Delta = \pm 2$ ns, describing a complete time correlation for most of the events of interest. It's possible to discriminate the Forward Tagger trigger time window, referring to all the minor peaks; each of them is located 4 ns apart one from another, reflecting exactly the detector trigger time.

- Identified Particles: 3 different topologies can be identified regarding the identified particles.
 - 1 Electron in FT; 2 Photons in FT.
 - 1 Electron in FT; 2 Photons in FD.
 - 1 Electron in FT; 1 Photon in FT; 1 Photon in FD.
- Time Correlation: 2 ns time difference (Δt) between the electron and photons detection. This specific condition, related to Fig. 3.11, will be explained in the next subsection.
- Kinematic Regions: Q^2 and virtual photon energy inside the boundaries of the kinematic regions of interest.

Please note that only FT electron cases are here listed and presented; however, the codes for the production of FD electron cases were also used, and the statistic of the resulting events wasn't noteworthy and was therefore neglected.

Note also that every constraint here presented has been already introduced in 1 or will be discussed in the next sections.

The filtering code used in this process is the one presented in Listing C.1; any function not explained in the listing will be further analyzed in the following subsections.

In order to focus on a more manageable amount of data and simplify the analysis process, a reduction process (*skimming*), realized directly at JLab, was applied to the Fall1028 data, leading to the production of the *Fall2018_skim2* set of data. The detection, inside the Forward Tagger, of 1 electron and 2 photons is the condition necessary for the event to be included in the skim2 reduction. This skimmed data were widely used in the first sections of the analysis and later replaced with the aforementioned more refined ones.

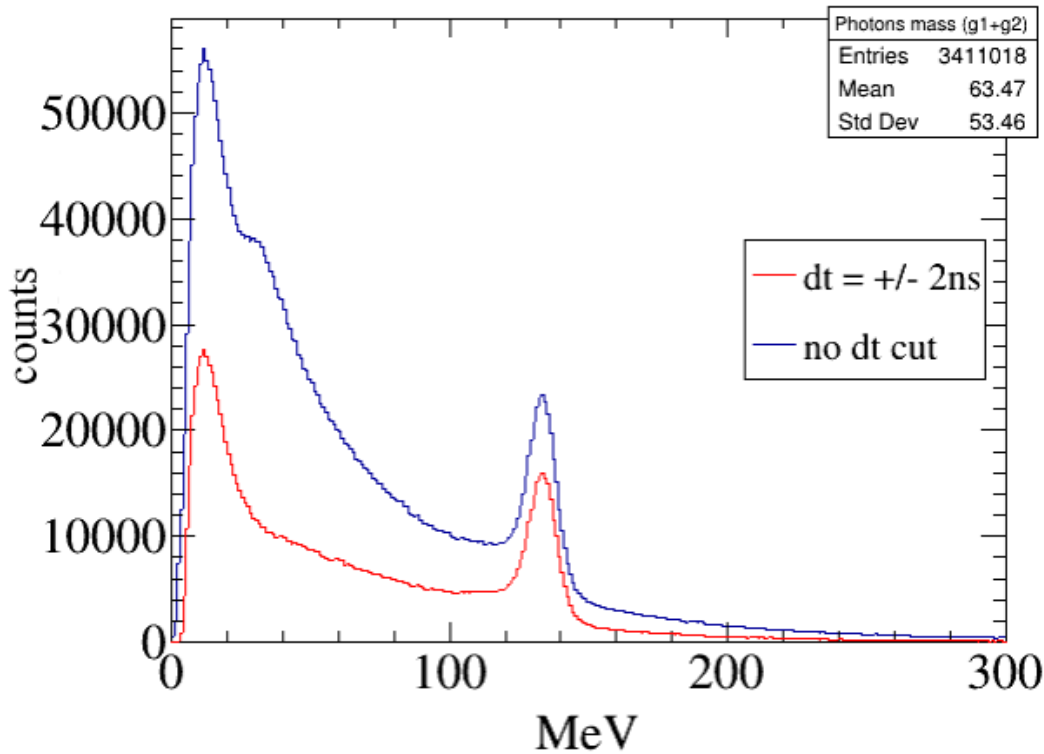


FIGURE 3.12: π^0 invariant mass comparison, pre and post-time coincidence cut, highlighted in blue and red, respectively. Most of the excluded events belong to the low energy region: these pions may be related to photons belonging to previous reactions, with energy that may match our case of interest, but with missing time coincidence.

3.3.1 The Missing Mass Method

The missing mass method allows for the determination of the properties of particles participating in a scattering reaction by utilizing the conservation laws of energy and momentum. A brief introduction of this method, as has been used in the presented analysis, is fundamental for the understanding of the following processes.

The missing mass method relies on the principle of conservation of energy and momentum. By measuring the energies and momenta of all detected particles before and after the scattering event, it is possible to deduce the properties of the particles involved, even if some particles escape undetected.

This procedure involves comparing the total energy and momentum of the detected particles before and after the scattering event. The missing mass, denoted as M_{miss} , is calculated as the difference between the total mass of the initial particles and the total mass of the detected particles after the interaction. This can be expressed mathematically as:

$$M_{miss} = (\sum E_{initial} - \sum E_{detected})^2 - (|\sum p_{initial}| - |\sum p_{detected}|)^2 \quad (3.3)$$

Here, $\sum E_{initial}$ and $\sum E_{detected}$ represent the total energies of the initial and detected particles, respectively, and $|\sum p_{initial}|$ and $|\sum p_{detected}|$ represent the magnitudes of the total momenta of the initial and detected particles, respectively.

In our case, the missing particle is the proton scattered during the reaction; finding the peak of the proton mass inside the energy distribution it's sign of a clearly detected reaction.

3.3.2 Applied Cuts and Filters

Time Coincidence

During the first step of the analysis, the focus was pointed on the difference in time detection between the electron and photons of each event; as can be seen from Fig. 3.11, the Δt peaks between the value of ± 2 ns.

Notice the peculiar shape of the signal, where all the subsequent peaks are set each every 4 ns on the x-axis: this pattern is a clear consequence of the Forward Tagger trigger time window, which is exactly equal to 4 ns.

This introduces the aforementioned first selection rule, cutting out all the events with $\Delta t > 2$ ns.

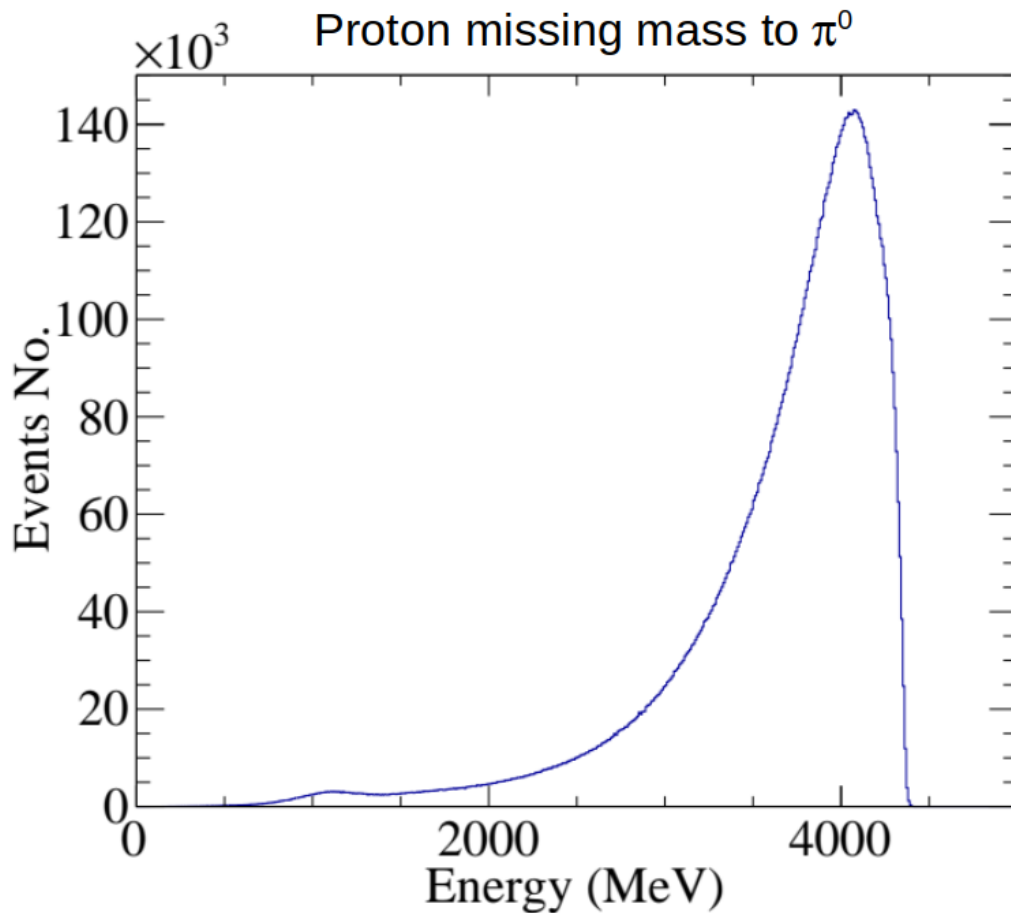


FIGURE 3.13: Proton missing mass to π^0 for the investigated reaction. The small bulge around 1 GeV represents the proton mass peak, which is the object of interest of the carried-on study.

Invariant Mass M_{π^0}

The difference between before and after the previously introduced cut is presented in the following histogram in Fig. 3.12, showing π^0 invariant mass from the given dataset.

The π^0 invariant mass, which can be described as the portion of the total mass of the particle that is independent of the events occurring in the considered system, is reflected by the clearly discriminated peak around 130MeV ; this introduces the second cut applied on the used dataset, which takes in account only the events with $120 < M_{\pi^0} < 150\text{MeV}$. This brings the analysis to the production of the proton missing mass histogram presented in Fig. 3.13.

Although this may lead to thinking that the peak is entirely composed of valid events for the thesis project, this is not true. It's fundamental to take into account all the different cases where the π^0 may belong to a previous different reaction, or it may be just part of a multiple π^0 production where the remaining part of the product is detected by the Forward Detector.

We can see the results of what has been said by looking at the previously cited figure, where the proton missing mass histogram is shown. The graph is dominated by a huge background component, linked to the undiscriminated multiple production events; a faint peak located around the proton mass value (938 MeV) shows the presence of the searched reaction and, so, the urge to apply cuts that may help in the improvement of the shot/noise ratio.

Please note that the shifting of the proton missing mass peak is caused by an error that occurred during data reconstruction. This effect is lightly compensated by a correction function, reported in section 3.3.3.

Sum of Photons Momenta $P_{\gamma_1} + P_{\gamma_2}$

In order to find new cuts, the investigation proceeded through the production of MonteCarlo simulations Pilloni, n.d. based on the Regge model of Ref. Mathieu, 2015. The code simulated a dataset composed of 10^7 exclusive pion electroproduction events reflecting the experiment conditions; after that, the data were processed using GEMC, applying the detector and reconstruction effects.

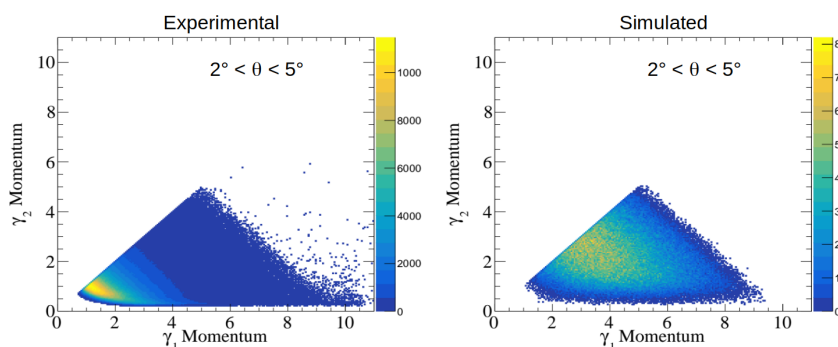


FIGURE 3.14: Detected photons momenta comparison between experimental and simulated data. The experimental dataset, on the left, shows a peak of the signal at low momenta. MonteCarlo simulations Pilloni, n.d. based on the Regge model of Ref. Mathieu, 2015 and processed through GEANT4 are reported in the right panel. The distributions are widely different. In the latter panel, the events are centered in an average value for the momenta, and slowly decrease moving away from the center of the distribution.

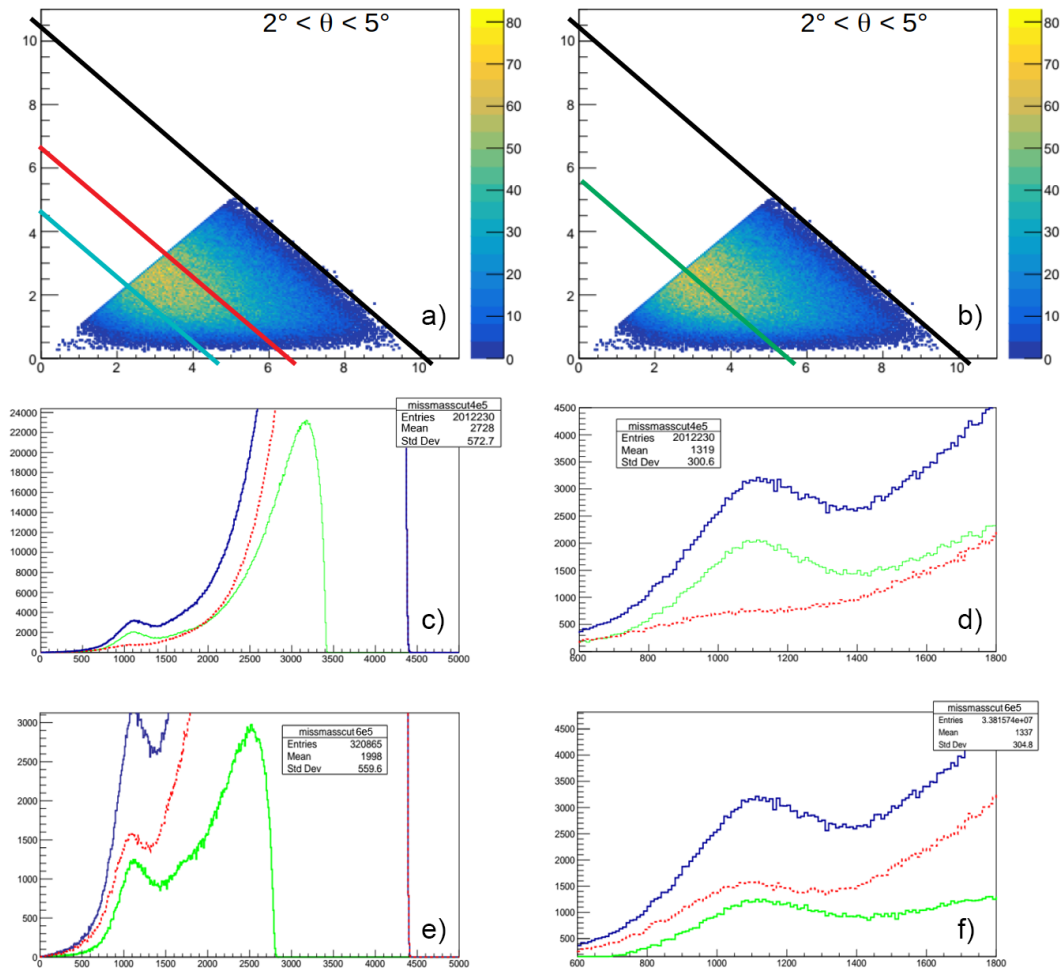


FIGURE 3.15: Cut efficiency tests to evaluate the correct option for the momenta cut. The two example values, 6.5 and 4.5 GeV are highlighted on panel a in blue and red, respectively. The effect on data of the two cuts is reported on panels c and d for the first one, and on e and f for the second one. In the latter four panels, the blue and green line highlights the distribution of the events before and after the cut, respectively. The red line, instead, represents all the events excluded from the dataset after the cut. It's clear that the first two histograms show a low data loss of good events if compared to the second case, but also a weaker reduction of the noise. In the second case, the noise is strongly reduced, but the loss of good events is not negligible. Comparing the two different cases and other intermediate ones, the best compromise between data loss and signal refinement is obtained using the cut expressed in panel b, at 5.5 GeV.

The resulting events were detailed, discovering a correlation between the detected photons momenta P_{γ_1} and P_{γ_2} ; this kind of relation, as can be deduced by the comparison shown in Fig. 3.14, implies that the detected particles of interest are primarily low-energy pions.

Still referring to the previously quoted Figure, it's clear that a sharp cut located around 5GeV should be the right solution, but it should be considered that the noise and signal areas overlap in a broad region, making not trivial the extraction of the right value for the cut boundary.

To better clear the signal while avoiding the loss of a large number of good events, a series of tests have been carried out, cutting around the edge of the limit value. Some examples are presented in Fig. 3.15. In panel *a* is possible to see the two different cuts located at 6.5 and 4.5 GeV , which will be used to produce the plots shown in panels *c* and *d*, for the first one, and *e* and *f* for the latter.

In the previously cited panels, both selected and removed data are plotted in blue and red, respectively.

The first case, where a wider cut is applied and more noise events are included for a higher signal events preservation, shows clearly a less defined cleaning of the peak if related to the second case, with a sharper cut not taking into account any kind of signal smearing and preferring a higher data loss in exchange of a better peak definition.

Clearly, the case representing the best compromise between signal clearing and data preservation is an average between the two presented solutions: the value chosen for the cut is $P_{\gamma_1} + P_{\gamma_2} < 5.5\text{GeV}$ and the results are presented in Fig. 3.16.

Please note that the black line reported in the first panels of Fig. 3.15 it's an additional constraint added as a higher limit: every event located in an area above the black line has a high chance of being the product of instrumental misdetection or signal.

Proton Missing Mass Refinishing

As can be seen in the histogram presented in panel *a* from the previously quoted Figure, the signal is still not clear enough and cannot be used for the ongoing analysis. The histogram required the application of the BruFit software presented in the sections above.

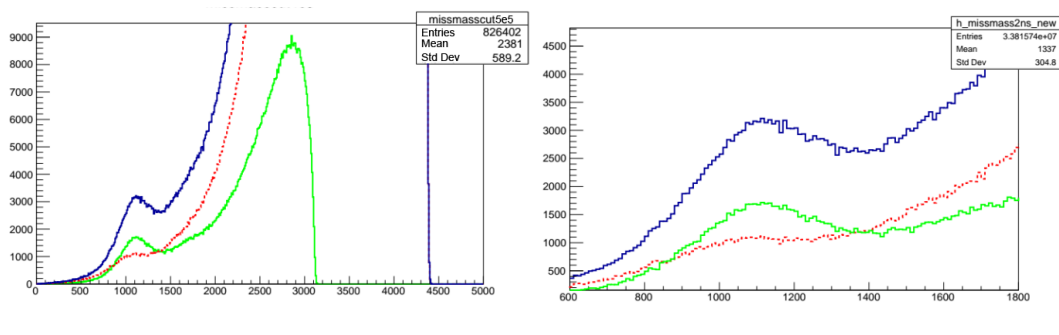


FIGURE 3.16: Missing mass plot for 5.5 GeV cut for photons momenta. The missing mass before and after the cut is plotted in blue and green, respectively, while the excluded data are plotted in red. As can be seen comparing the two figures with the ones exposed in Fig. 3.15, this case shows the best compromise, giving a good signal resolution without losing too many events from the researched region.

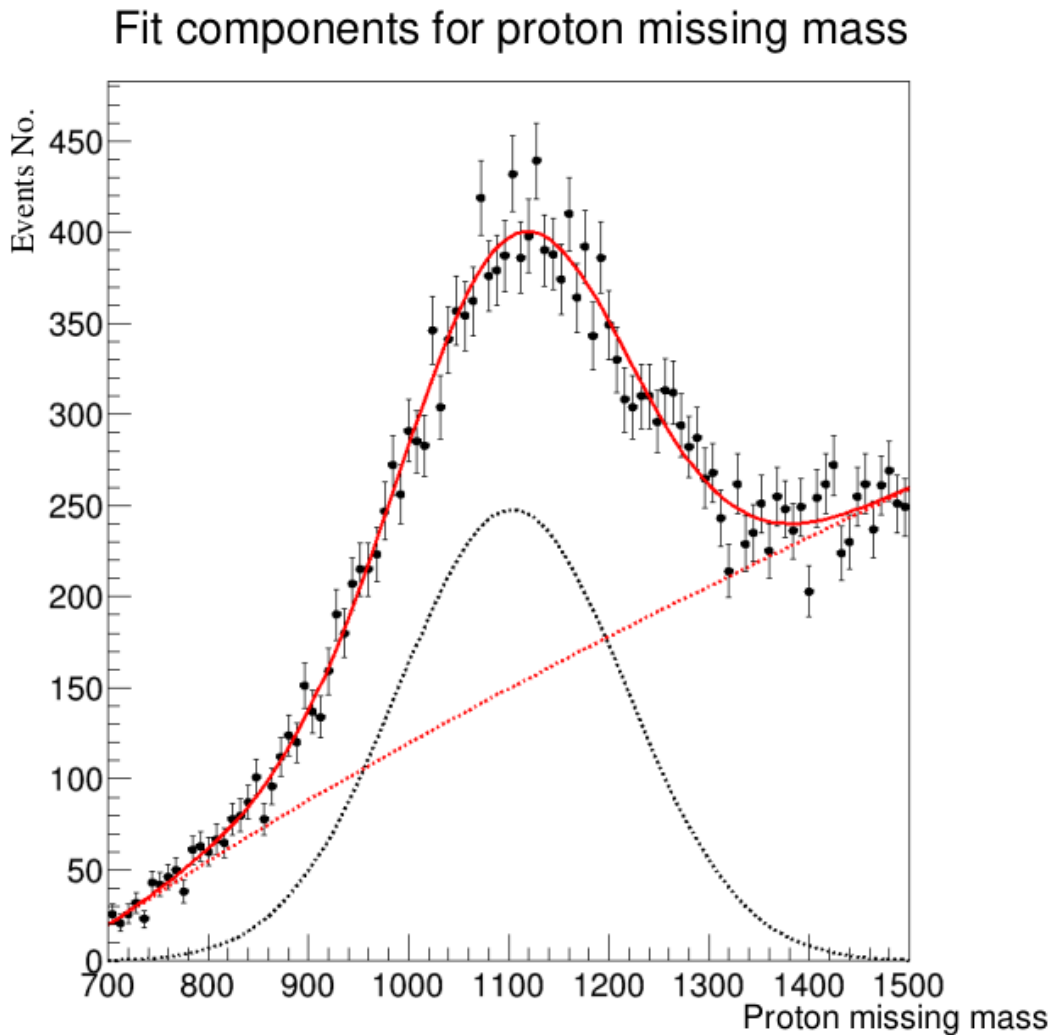


FIGURE 3.17: SPlot brufit feature application on the dataset. The big black dots, along with the red full line, shows the original missing mass distribution. After the sPlot application, using a Gaussian shape for the peak and a Chebyshev polynomial for the background, each event is correlated to a weight that can span between $+$ and -1 . The red dotted line shows the weighted background, while the black dotted one the weighted signal. Taking into account the calibration errors, the peak is located around the proton mass value.

Applying the sPlot feature of the aforementioned software on the missing mass histogram is possible to correlate each event with a statistical weight that can vary between -1 , for the events considered as background, and $+1$, for the ones labeled as part of the proton peak. The cleared signal is reported in Fig. 3.17.

The shapes used for the sPlot feature are the following:

- **Signal:** Gaussian distribution $\frac{1}{\sqrt{2\pi}\sigma} e^{-\frac{x-\mu}{2\sigma^2}}$, with peak centroid $\mu = 1103.7 \pm 3.7$ and $\sigma = 113.5 \pm 5.2$.
- **Background:** Chebyshev polynomials of the third kind, with $a = 0.825 \pm 0.033$, $b = -0.0352 \pm 0.057$ and $c = 0.005 \pm 0.024$.

As can be seen from the example Fig. 3.19 the cut is efficient in the cleaning of the unwanted events revealing also peculiar features, like the drop at $t' = 0.5$, which may be investigated in future analysis.

Please note that t' in here represents the normalized Mandelstam variable t with equation $t' = -2P_{\gamma^*}P_{\pi^0}(1 - \cos\theta_{\gamma^*\pi^0})$.

3.3.3 Energy Correction

As seen in all the previous missing mass images, the proton peak is shifted from its position at 938 MeV . This effect, which is currently under investigation, is related to an error in the FT-Cal information reconstruction.

A first correction formula, already used in the previously shown analysis, has been developed, reducing signal deformation and shifting. Although the research for an additional correction is still ongoing, the correction mentioned above, described by the following equation, has been considered sufficient for the presented analysis; the shape of the function is presented in figure 3.18

$$E_{new} = -0.03689 + 1.1412E_e - 0.04316E_e^2 + 0.007046E_e^3 - 0.0004055E_e^4. \quad (3.4)$$

3.3.4 Kinematic Regions Boundaries Selection

It's crucial for the analysis to choose the correct kinematic region to study. As can be seen in Fig. 3.20, it's possible to detect four regions in the $(\nu; Q^2)$ space (where $\nu = E_{\gamma^*}$ and $Q^2 = -q^2$, each of which is again divided into 0.1 GeV^2 -wide t' subregions in order to better discriminate the peculiar feature of the Σ drop shown in Fig. 1.9 presented in chapter Mathieu, 2015. Low virtual photon energy and squared mass can be signals of a correct quasi-real π^0 photoproduction, setting so the boundary values for the cuts.

These last cuts are clearly introduced to compare the obtained results with the GlueX and SLAC experiments, being crucial to better explain the selection applied for the virtual photon energy and mass.

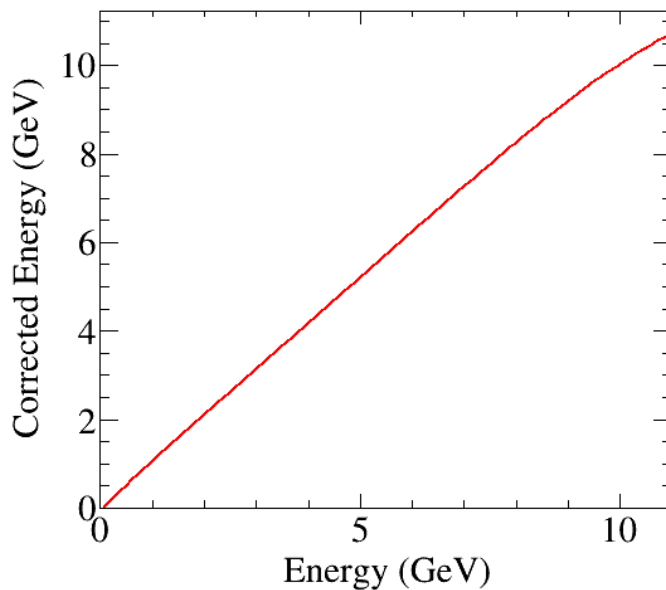


FIGURE 3.18: Energy correction with equation $E_{new} = -0.03689 + 1.1412E_e - 0.04316E_e^2 + 0.007046E_e^3 - 0.0004055E_e^4$.

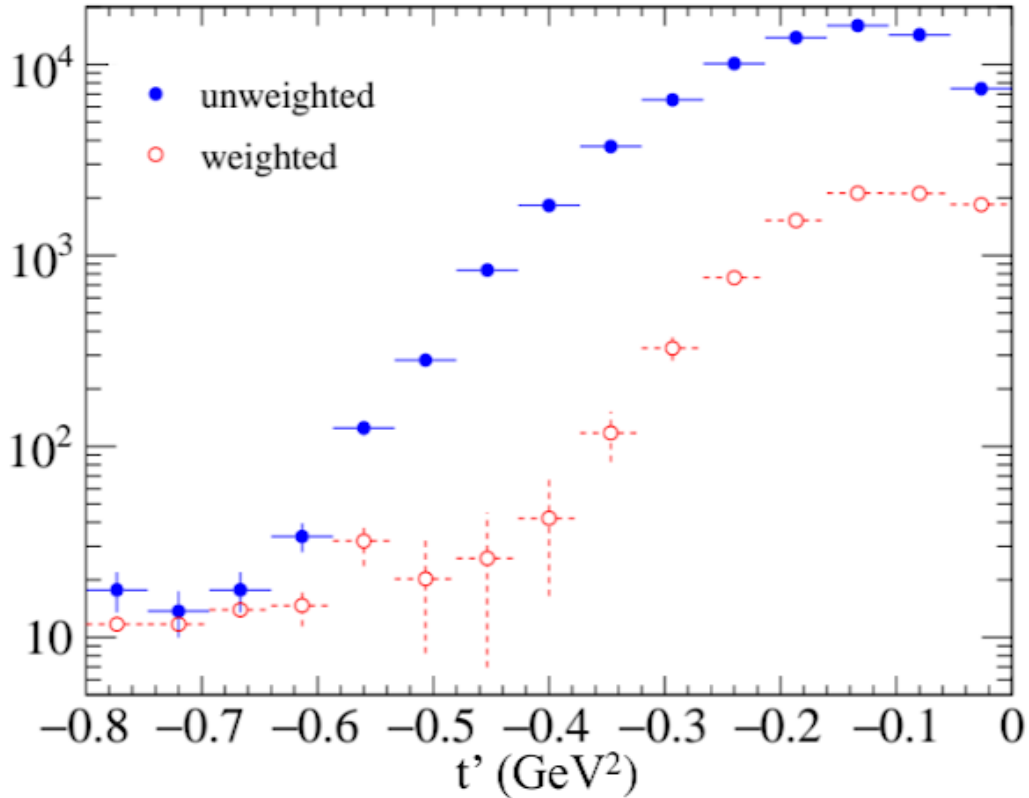


FIGURE 3.19: t' distribution comparison before and after the sPlot application on the missing mass histogram. The two distributions are reported in blue and red, respectively. As can be seen from the peculiar feature at -0.5 , the cleaning can make some peculiar features, not visible in the first instance, appear clearly.

In order to do this, a brief description of the identified subregions will be now presented:

- **Region A1:** low Q^2 and high ν . The region goes from 7 to 9 GeV and from 0 to 0.15 GeV².
- **Region A2:** high Q^2 and high ν . The region goes from 7 to 9 GeV and from 0.15 to 0.5 GeV².
- **Region B1:** low Q^2 and low ν . The region goes from 5.5 to 7 GeV and from 0 to 0.15 GeV². This is the chosen region for the carried-on analysis.
- **Region B2:** high Q^2 and low ν . The region goes from 5.5 to 7 GeV and from 0.15 to 0.5 GeV². This region, having a higher Q^2 and so a more massive photon, strives from the searched reaction which requires a quasi-real photon.

3.3.5 Beam asymmetry Σ preliminary extraction

After the cuts application and the selection of the best kinematic region, the analysis followed the now presented step:

- Average polarization calculation ($\bar{\epsilon}$), calculated and then mediated all over the data thanks to the equation (1.35).

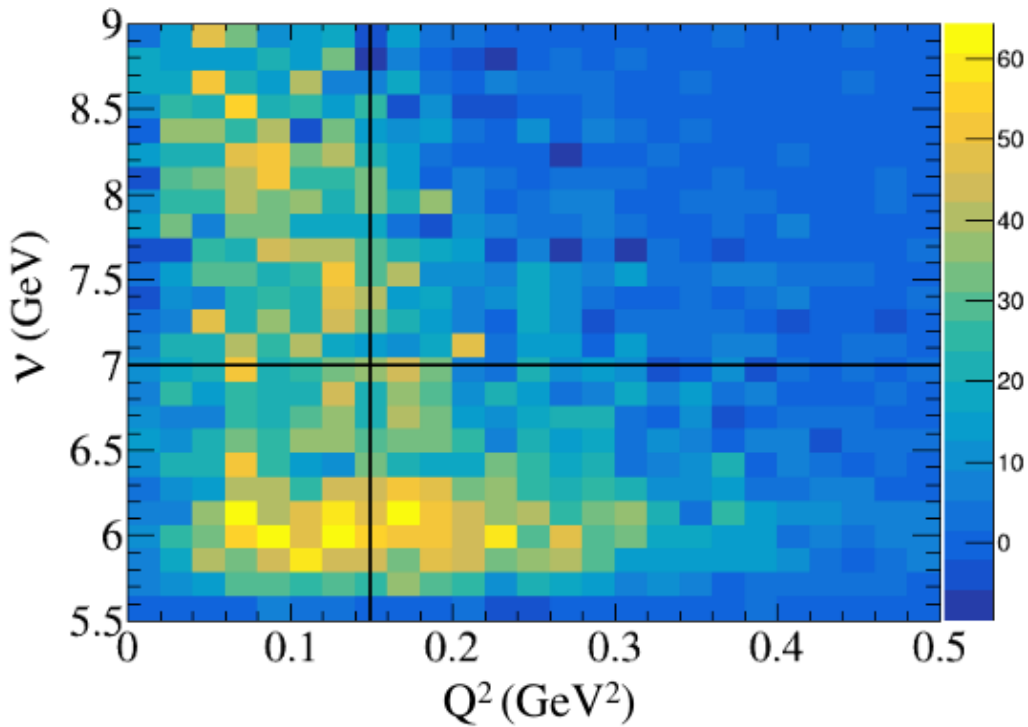


FIGURE 3.20: Kinematic region of interest selection. The areas here presented are, from top left to bottom right: A1 ($0 < Q^2 < 0.15$; $7 < \nu < 9$), A2 ($0.15 < Q^2 < 0.5$; $7 < \nu < 9$), B1 ($0 < Q^2 < 0.15$; $5.5 < \nu < 7$) and B2 ($0.15 < Q^2 < 0.5$; $5.5 < \nu < 7$). The area selected for the analysis is the B1.

- Plot of the weighted scattering angle related to the reaction plane (ϕ).
- Fit of the aforementioned plot using the equation 1.41, where $\epsilon = \bar{\epsilon}$.

The result of what has been summarized is presented in Fig. 3.21.

It's crucial to outline that the result here presented, although resembling the correct shape and being near to the predicted result, points to an incorrect evaluation of Σ . For a better extraction of the researched result, an acceptance correction must be applied to the analyzed data.

3.3.6 Detector Acceptance Analysis

Acceptance calculation for the presented analysis made use of the GEMC software and the MC simulations discussed above, processing the simulated data and applying the detectors and reconstruction effects.

An acceptance map can be completely reproduced by comparing the pre- and post-GEMC processing datasets; the acceptance describes the signal deformation for each kinematic section and each t' interval. This correction can be applied to data to extract the correct shape of the signal.

In Fig. 3.22 and 3.23 some of the acceptance corrections calculated with test $\Sigma = 0$ are shown; ongoing analyses are directed at the calculation of acceptance correction for different Σ values, in order to investigate better any kind of discrepancy in detector acceptance linked to the beam asymmetry variation.

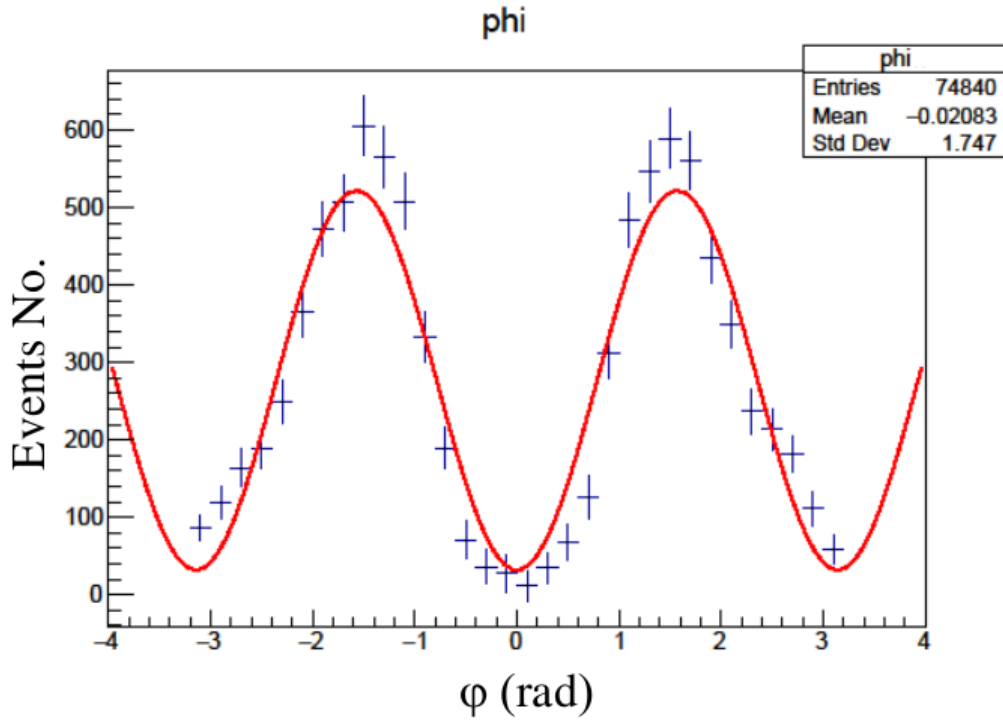


FIGURE 3.21: Scattering angle ϕ of the selected data. The red line shows the fit for the ϕ function reported in equation 1.41.

Some crucial issues appear clear from the presented results; the drop in detector acceptance around $\phi = 0$ makes the extrapolation of the correct value difficult for $0 < -t < 0.2$. The histogram of reference showing the best fit is represented in Fig. 3.24. It is possible to refine the measure by proceeding with additional acceptance studies.

Moving at higher $-t$ values, the number of events drops significantly and the acceptance hole is still present, although gradually decreasing.

Investigations have been carried out on events at angles higher than the FT ranges, including the Forward Detector events, in order to analyze $0.2 < -t < 0.8$ sectors. Though the π^0 exclusive electroproduction process was slightly detectable in the FT dataset, as can be seen in Fig. 3.13, it's completely undetected in the FD area, giving no results for this analysis.

Two possible solutions for the encountered issues may be:

- Development of new simulated datasets with $-1 < \Sigma < +1$; analyzing the detector behavior at the variation of the beam asymmetry may lead to a better understanding of the acceptance shape.
- Development of a specific trigger for FD, with a higher sensitivity for the researched reaction. This solution may give a higher number of events in the region of interest.

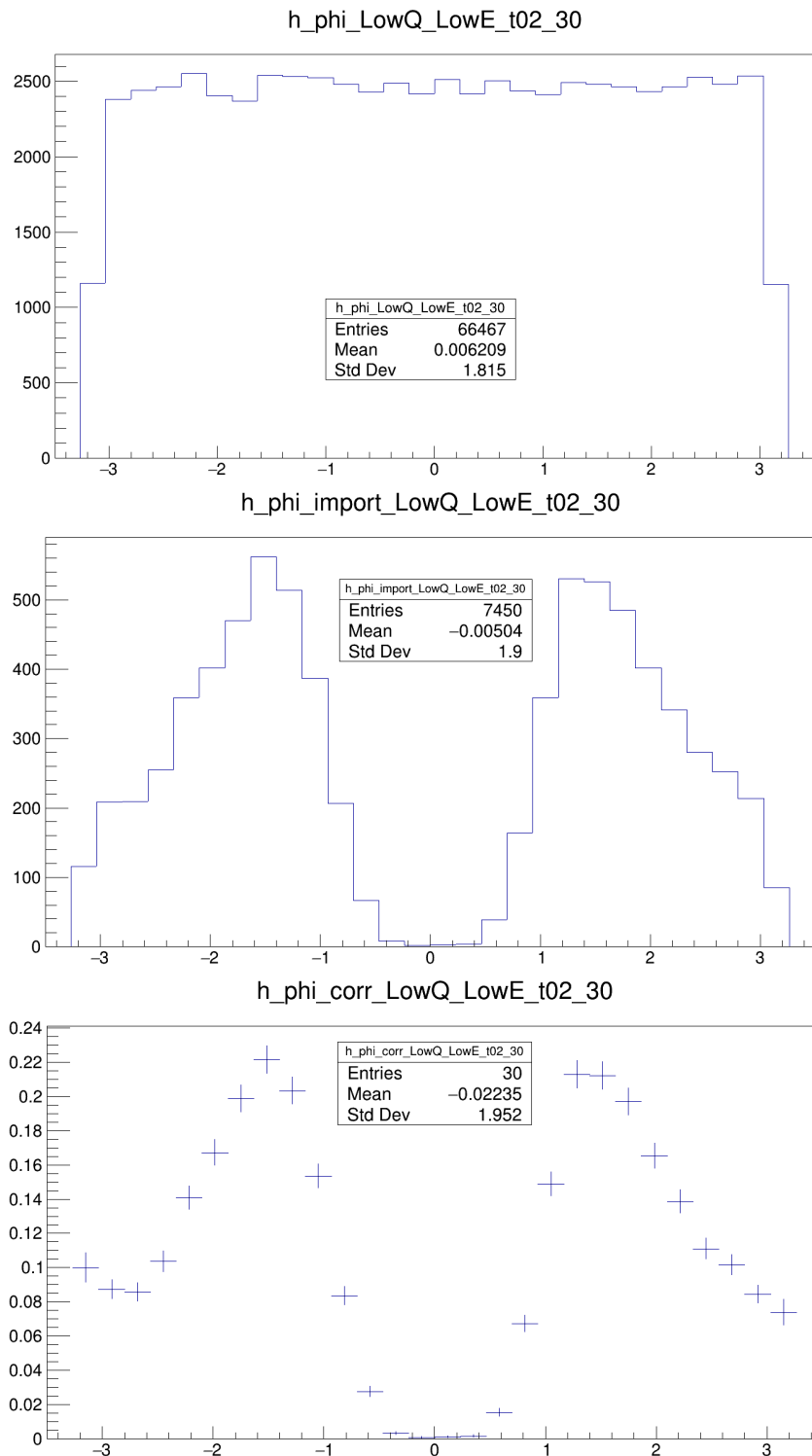


FIGURE 3.22: Acceptance calculation example. The plots in the first two panels show the scattering angle ϕ calculated for simulated data before and after the GEMC processing. The last plot shows the acceptance correction comprehensive of the error on the calculation.

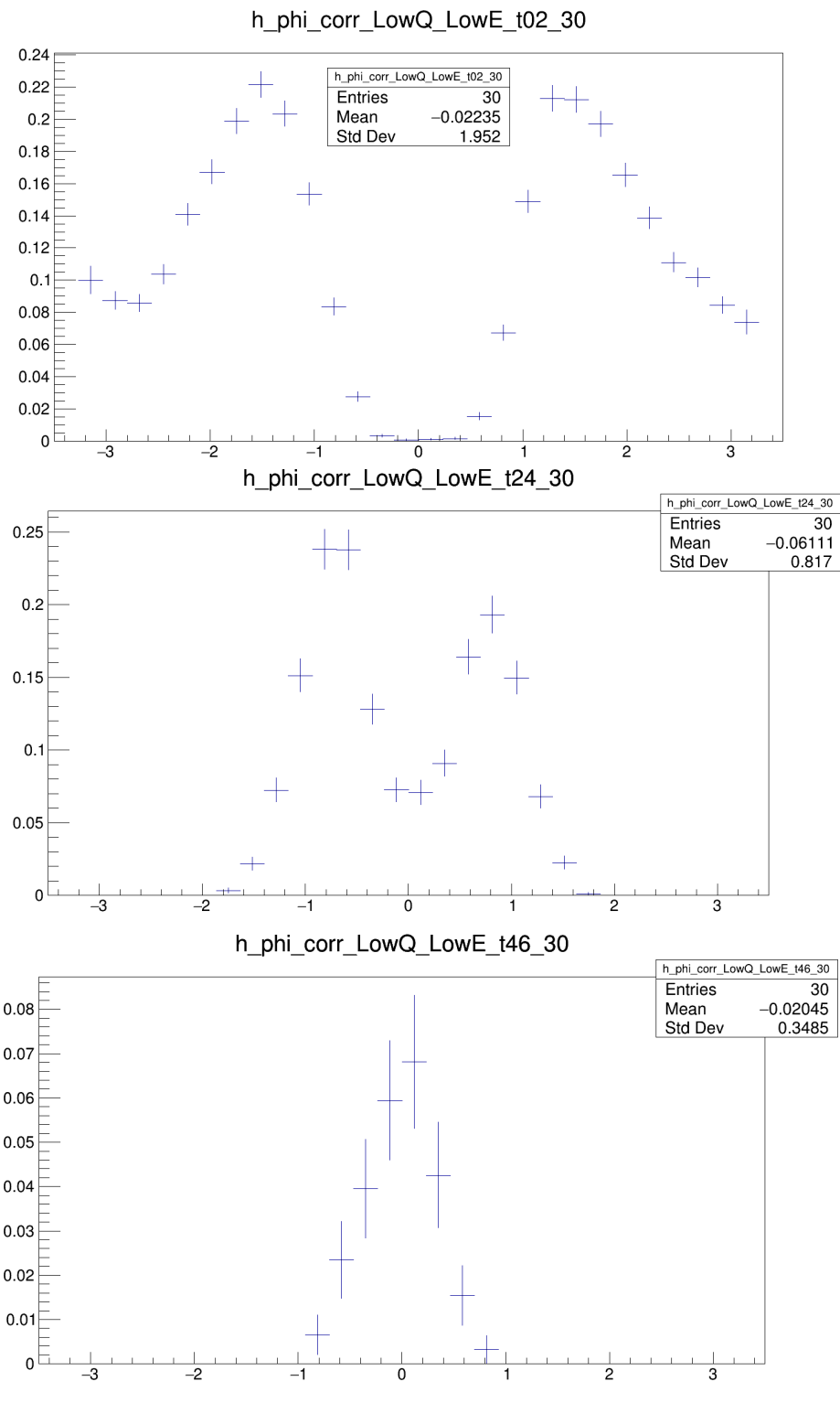


FIGURE 3.23: Acceptance calculation for different range of t . The three panels, from top to bottom, show $0 < -t < 0.2$, $0.2 < -t < 0.4$, and $0.4 < -t < 0.6$ which cover all the regions of interest of the presented measurements. Fig. 3.25 is reported for easier consultation.

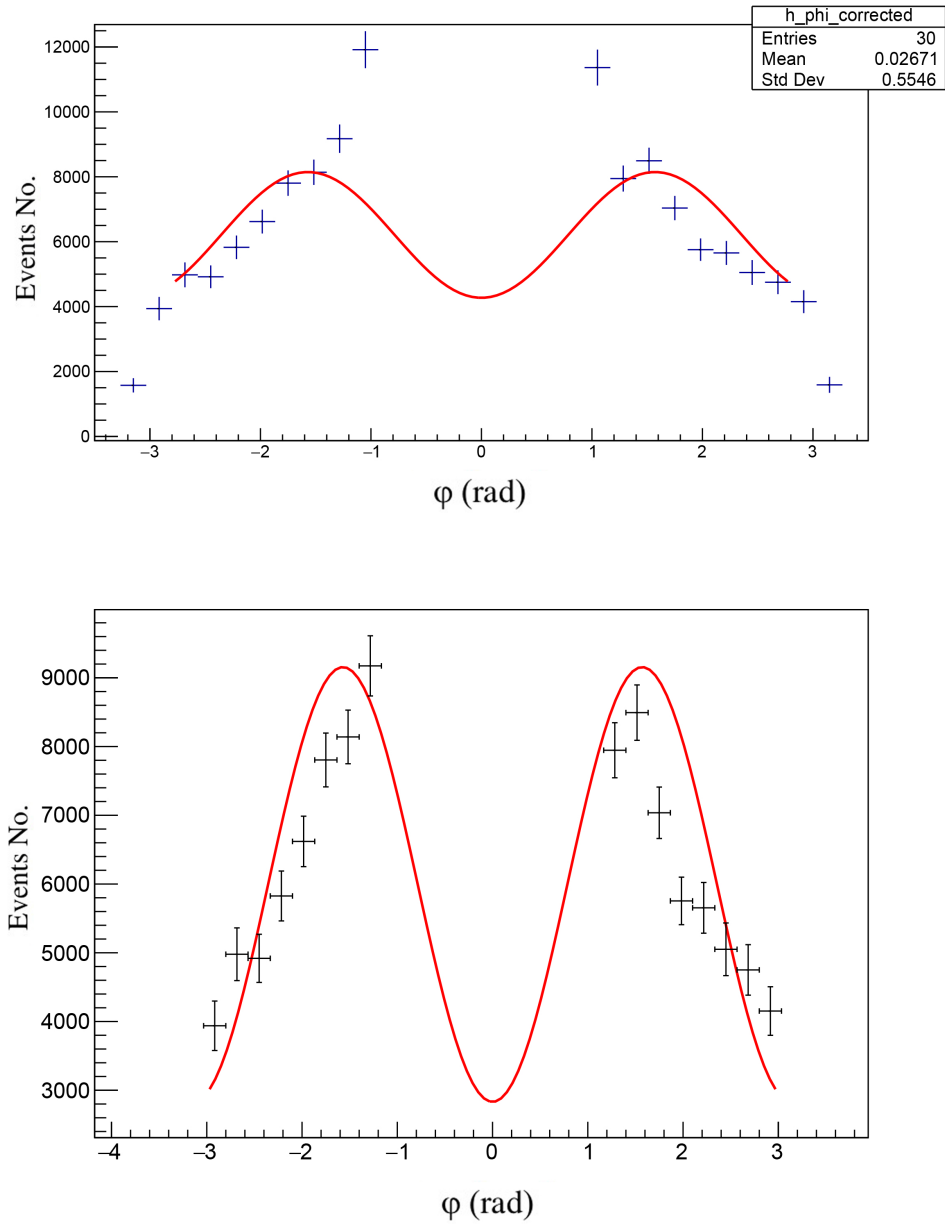


FIGURE 3.24: Acceptance corrected beam asymmetry calculated in the previously chosen kinematic region, for $0 < -t < 0.2$. The left panel shows a preliminary fit, while the right panel is the best fit available, reached by removing non-physical points caused by the detector acceptance features.

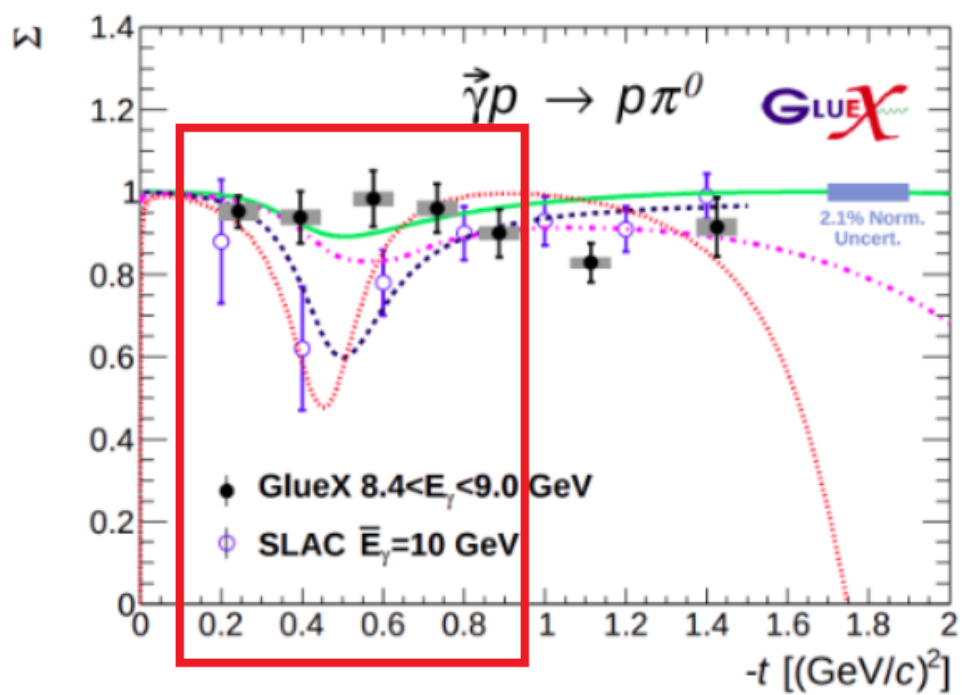


FIGURE 3.25: Highlight of the studied $-t$ regions. A better description of this graph is reported in Fig. 3.13.

Chapter 4

Results and Conclusions

Thanks to the *Fall2018* dataset, produced by CLAS12 and especially thanks to the Forward Tagger detector, it has been possible to carry on the analysis on the searched reaction, confirming the detector performance and applicability.

The π^0 from $e + p \rightarrow e + p + \pi^0$ reaction has been fully reconstructed thanks to the detection of $2\gamma + e$ in FT. The study of this reaction may have fundamental consequences in the confirmation of the Regge theory for high energies and for the clarification of the discrepancy in Beam Asymmetry extraction between SLAC and GlueX analysis, as can be seen from Fig. 1.9 (see Al Ghouli et al., 2017).

Aiming at the aforementioned results, the extraction of the proton missing mass has been carried out, bringing to the application of different cuts in order to clean the signal. The information about the range of the cuts has been obtained thanks to the use of different simulation instruments, such as GEANT4.

The application of the constraints on time coincidence, invariant mass, and sum of photons momenta, reported in Fig. 3.11, 3.12, 3.14, was yet effective but not enough to completely clean the searched information. The remaining background, presented in Fig. 3.16, has been removed thanks to Brufit software, giving the final shape of the proton missing mass peak, reported in 3.17.

After the signal cleaning and the kinematic channel selection, a plot for the scattering angle ϕ has been used for the extraction of the Beam Asymmetry Σ . In order to achieve the fit necessary for the extraction, a simulation for $\Sigma = 0$ data has been produced and used for detector acceptance calculation.

In conclusion, the analysis demonstrates that, though the apparatus is capable of detecting the researched reaction, it's not possible to extract further information from the currently available dataset. In order to proceed with the analysis it's necessary to produce a dedicated trigger for the Forward Detector, capable of a better event selection, and generate more simulated data at different Σ , expanding the detector acceptance study.

By the application of this solution, a better resolution of the signal in the interested region, presented in 3.25, can be achieved, along with the researched results.

Appendix A

Forward Tagger Trigger Settings

LISTING A.1: Forward Tagger trigger settings.

```

1
2 #####
3 # CLAS12 daq/trigger default config file #
4 #####
5
6 #####
7 # TI settings (TI master only)
8 #####
9
10 #####
11 # FADC settings (detector-related)
12 #####
13
14 # Common settings
15
16 FADC250_CRATE all
17 FADC250_SLOT      all
18
19 # compression: 0-no compression, 1-compression, 2-both (verify mode)
20 FADC250_COMPRESSION 1
21
22 FADC250_MODE      1
23 ##FADC250_W_OFFSET 7900
24 FADC250_W_OFFSET 7650
25 FADC250_W_WIDTH  384
26 FADC250_CRATE end
27
28 TDC1190_CRATE all
29 TDC1190_SLOT all
30 TDC1190_W_WIDTH 800
31 TDC1190_W_OFFSET -8450
32 TDC1190_CRATE end
33
34 TDC1190_CRATE tdcctof1
35 TDC1190_SLOT all
36 TDC1190_W_WIDTH 800
37 TDC1190_W_OFFSET -8250
38 TDC1190_CRATE end
39
40 TDC1190_CRATE adccnd1
41 TDC1190_SLOT all
42 TDC1190_W_WIDTH 800
43 TDC1190_W_OFFSET -8200
44 TDC1190_CRATE end
45
46

```

```

47
48 VSCM_CRATE all
49 VSCM_SLOT all
50 ##VSCM_TRIG_WINDOW      96      1064      16
51 ##VSCM_TRIG_WINDOW      96      1032      16
52 ##VSCM_TRIG_WINDOW      96      968      16
53 ##VSCM_TRIG_WINDOW      80      976      16
54 #VSCM_TRIG_WINDOW       80      980      16
55 #VSCM_TRIG_WINDOW       80      978      16
56 #VSCM_TRIG_WINDOW       80      979      16
57 VSCM_TRIG_WINDOW        64      979      16
58 VSCM_CRATE end
59
60 DCRB_CRATE all
61 DCRB_SLOT all
62 ##DCRB_W_OFFSET  7900
63 DCRB_W_OFFSET    7650
64 DCRB_CRATE end
65
66
67
68 #does not work yet !!!!!!!
69 #SSP_CRATE      rich4
70 #SSP_SLOT       all
71 #SSP_RICH_W_WIDTH    300
72 #SSP_RICH_W_OFFSET  7980
73 #SSP_CRATE end
74
75
76
77 #####
78 #
79 #####
80
81 # ECAL settings
82 #include trigger/EC/ecal_default.cnf
83 include trigger/EC/ecal_newgain_prod.cnf
84
85 # PCAL settings
86 #include trigger/EC/pcal_default.cnf
87 include trigger/EC/pcal_newgain_prod.cnf
88
89 # FTOF settings
90 include trigger/FTOF/ftof_default.cnf
91
92 # LTCC settings
93 include trigger/LTCC/ltcc_default.cnf
94
95 # CTOF/HTCC settings
96 include trigger/CTOF_HTCC/ctof_htcc_newgain_prod.cnf
97
98 # CND settings
99 include trigger/CND/cnd_prod.cnf
100
101 #FT CAL AND HODO
102 include trigger/FT/ft_default.cnf
103
104 #SVT
105 include trigger/SVT/svt_prod.trg
106
107 #####
108 # Trigger stage 1 (crates with FADCs) #
109 #####

```

```
110
111 # ECAL
112 VTP_CRATE adcecal1vtp
113     include trigger/VTP/ecalvtp_low_thres.cnf
114 VTP_CRATE end
115
116 VTP_CRATE adcecal2vtp
117     include trigger/VTP/ecalvtp_low_thres.cnf
118 VTP_CRATE end
119
120 VTP_CRATE adcecal3vtp
121     include trigger/VTP/ecalvtp_low_thres.cnf
122 VTP_CRATE end
123
124 VTP_CRATE adcecal4vtp
125     include trigger/VTP/ecalvtp_low_thres.cnf
126 VTP_CRATE end
127
128 VTP_CRATE adcecal5vtp
129     include trigger/VTP/ecalvtp_low_thres.cnf
130 VTP_CRATE end
131
132 VTP_CRATE adcecal6vtp
133     include trigger/VTP/ecalvtp_low_thres.cnf
134 VTP_CRATE end
135
136 # PCAL
137 VTP_CRATE adcpcal1vtp
138     include trigger/VTP/pcalvtp_low_thres.cnf
139     include trigger/VTP/pcuvtp_default.cnf
140 VTP_CRATE end
141
142 VTP_CRATE adcpcal2vtp
143     include trigger/VTP/pcalvtp_low_thres.cnf
144     include trigger/VTP/pcuvtp_default.cnf
145 VTP_CRATE end
146
147 VTP_CRATE adcpcal3vtp
148     include trigger/VTP/pcalvtp_low_thres.cnf
149     include trigger/VTP/pcuvtp_default.cnf
150 VTP_CRATE end
151
152 VTP_CRATE adcpcal4vtp
153     include trigger/VTP/pcalvtp_low_thres.cnf
154     include trigger/VTP/pcuvtp_default.cnf
155 VTP_CRATE end
156
157 VTP_CRATE adcpcal5vtp
158     include trigger/VTP/pcalvtp_low_thres.cnf
159     include trigger/VTP/pcuvtp_default.cnf
160 VTP_CRATE end
161
162 VTP_CRATE adcpcal6vtp
163     include trigger/VTP/pcalvtp_low_thres.cnf
164     include trigger/VTP/pcuvtp_default.cnf
165 VTP_CRATE end
166 #
167 # HTCC
168 #
169 VTP_CRATE adcctof1vtp
170     include trigger/VTP/htcc_prod_2phe.cnf
171 VTP_CRATE end
172
```

```

173 #FT (3 VTPs inside the file)
174 include trigger/VTP/ftvtp_prod.cnf
175
176 # FTOF
177 VTP_CRATE adcftof1vtp
178     include trigger/VTP/ftofvtp_prod.cnf
179 VTP_CRATE end
180 VTP_CRATE adcftof2vtp
181     include trigger/VTP/ftofvtp_prod.cnf
182 VTP_CRATE end
183 VTP_CRATE adcftof3vtp
184     include trigger/VTP/ftofvtp_prod.cnf
185 VTP_CRATE end
186 VTP_CRATE adcftof4vtp
187     include trigger/VTP/ftofvtp_prod.cnf
188 VTP_CRATE end
189 VTP_CRATE adcftof5vtp
190     include trigger/VTP/ftofvtp_prod.cnf
191 VTP_CRATE end
192 VTP_CRATE adcftof6vtp
193     include trigger/VTP/ftofvtp_prod.cnf
194 VTP_CRATE end
195
196 # CTOF
197 VTP_CRATE adcctof1vtp
198     include trigger/VTP/ctofvtp_prod.cnf
199 VTP_CRATE end
200
201 # CND
202 VTP_CRATE adccnd1vtp
203     include trigger/VTP/cndvtp_prod.cnf
204 VTP_CRATE end
205
206
207 #####
208 # Trigger stage 2 (crate trig2) #
209 #####
210
211 SSP_CRATE trig2
212 SSP_SLOT all
213
214 SSP_W_OFFSET 7650
215 SSP_W_WIDTH 400
216
217 # 'SSP_GT_' - sectors trigger logic
218
219 SSP_GT_LATENCY          5000
220
221 SSP_GT_HTCC_DELAY      1164
222 SSP_GT_ECAL_CLUSTER_DELAY 1024
223 SSP_GT_PCAL_CLUSTER_DELAY 1024
224 SSP_GT_CTOF_DELAY      1236
225 SSP_GT_CND_DELAY       1244
226 SSP_GT_FTOF_DELAY      1104
227 SSP_GT_PCAL_PCU_DELAY  1068
228
229
230 # if use this, add 1024 to all above and SSP_GTC_FT_CLUSTER_DELAY
    below,
231 # subtract same from VTP_GT_LATENCY and VTP_W_OFFSET
232 SSP_GT_DC_SEG_DELAY    0
233
234

```

```

235
236 #pcu
237 SSP_GT_FTOFPCU_FTOF_WIDTH      32
238 SSP_GT_FTOFPCU_PCU_WIDTH      32
239 SSP_GT_FTOFPCU_MATCH_TABLE    0      # 0 is the old map, 1 is the
      new map Andrea provided after the last run
240
241
242 # 'SSP_GT_STRG_' - sector trigger bits - logic inside single sector
243
244 #####
245 #
246 # Sector Trigger bit 0
247 #
248 # DC_INBEND x HTCC x (PCAL+ECAL)>300MeV x PCAL>60MeV x ECAL>10MeV
249 #####
250 SSP_GT_STRG                      0
251 SSP_GT_STRG_EN                    1
252
253 # HTCC trigger logic
254 SSP_GT_STRG_HTCC_EN                1
255 SSP_SLOT 3      # sector 1 SSP
256 SSP_GT_STRG_HTCC_MASK              0x0000000000FF
257 SSP_SLOT 4      # sector 2 SSP
258 SSP_GT_STRG_HTCC_MASK              0x00000000FF00
259 SSP_SLOT 5      # sector 3 SSP
260 SSP_GT_STRG_HTCC_MASK              0x000000FF0000
261 SSP_SLOT 6      # sector 4 SSP
262 SSP_GT_STRG_HTCC_MASK              0x0000FF000000
263 SSP_SLOT 7      # sector 5 SSP
264 SSP_GT_STRG_HTCC_MASK              0x00FF00000000
265 SSP_SLOT 8      # sector 6 SSP
266 SSP_GT_STRG_HTCC_MASK              0xFF0000000000
267 SSP_SLOT all
268 SSP_GT_STRG_HTCC_WIDTH              0
269
270 # PCAL cluster trigger logic
271 SSP_GT_STRG_PCAL_CLUSTER_EMIN_EN    1
272 SSP_GT_STRG_PCAL_CLUSTER_EMIN      600
273 SSP_GT_STRG_PCAL_CLUSTER_WIDTH     96
274
275 # ECAL cluster trigger logic
276 SSP_GT_STRG_ECAL_CLUSTER_EMIN_EN    1
277 SSP_GT_STRG_ECAL_CLUSTER_EMIN      100
278 SSP_GT_STRG_ECAL_CLUSTER_WIDTH     96
279
280 # PCAL+ECAL cluster trigger logic: EMIN in 0.1MeV units
281 SSP_GT_STRG_ECALPCAL_CLUSTER_EMIN_EN 1
282 SSP_GT_STRG_ECALPCAL_CLUSTER_EMIN    3000
283 SSP_GT_STRG_ECALPCAL_CLUSTER_WIDTH   96
284
285 # DC
286 SSP_GT_STRG_DC_EN                    1
287 SSP_GT_STRG_DC_ROAD_REQUIRED          0
288 SSP_GT_STRG_DC_ROAD_INBEND_REQUIRED  1
289 SSP_GT_STRG_DC_ROAD_OUTBEND_REQUIRED  0
290 SSP_GT_STRG_DC_MULT_MIN                5
291 SSP_GT_STRG_DC_WIDTH                  32
292
293
294
295 #####
296 #

```

```

297 # Sector Trigger bit 1
298 #
299 #   DC_INBEND x HTCC x PCAL>300MeV
300 #####
301 SSP_GT_STRG                               1
302 SSP_GT_STRG_EN                             1
303
304 # HTCC trigger logic
305 SSP_GT_STRG_HTCC_EN                         1
306 SSP_SLOT 3      # sector 1 SSP
307 SSP_GT_STRG_HTCC_MASK                       0x0000000000FF
308 SSP_SLOT 4      # sector 2 SSP
309 SSP_GT_STRG_HTCC_MASK                       0x00000000FF00
310 SSP_SLOT 5      # sector 3 SSP
311 SSP_GT_STRG_HTCC_MASK                       0x000000FF0000
312 SSP_SLOT 6      # sector 4 SSP
313 SSP_GT_STRG_HTCC_MASK                       0x0000FF000000
314 SSP_SLOT 7      # sector 5 SSP
315 SSP_GT_STRG_HTCC_MASK                       0x00FF00000000
316 SSP_SLOT 8      # sector 6 SSP
317 SSP_GT_STRG_HTCC_MASK                       0xFF0000000000
318 SSP_SLOT all
319 SSP_GT_STRG_HTCC_WIDTH                       0
320
321 # PCAL cluster trigger logic
322 SSP_GT_STRG_PCAL_CLUSTER_EMIN_EN             1
323 SSP_GT_STRG_PCAL_CLUSTER_EMIN               3000
324 SSP_GT_STRG_PCAL_CLUSTER_WIDTH              96
325
326 # DC
327 SSP_GT_STRG_DC_EN                           1
328 SSP_GT_STRG_DC_ROAD_REQUIRED                 0
329 SSP_GT_STRG_DC_ROAD_INBEND_REQUIRED          1
330 SSP_GT_STRG_DC_ROAD_OUTBEND_REQUIRED         0
331 SSP_GT_STRG_DC_MULT_MIN                     5
332 SSP_GT_STRG_DC_WIDTH                        32
333
334
335 #####
336 #
337 # Sector Trigger bit 2
338 #
339 #   DC x FTOFPCU x PCAL>15 MeV
340 #####
341 SSP_GT_STRG                               2
342 SSP_GT_STRG_EN                             1
343
344 # PCU trigger logic
345 SSP_GT_STRG_FTOFPCU_EN                     1
346 SSP_GT_STRG_FTOFPCU_WIDTH                   64
347 SSP_GT_STRG_FTOFPCU_MATCH_MASK              8
348
349 # SSP_GT_STRG_FTOFPCU_MATCH_MASK   N
350 # N: 1 = +/-0 FTOF strip tolerance
351 #   2 = +/-1 FTOF strip tolerance
352 #   4 = +/-2 FTOF strip tolerance
353 #   8 = +/-3 FTOF strip tolerance
354 #  16 = +/-4 FTOF strip tolerance
355 #  32 = +/-5 FTOF strip tolerance
356
357
358 # PCAL cluster trigger logic
359 SSP_GT_STRG_PCAL_CLUSTER_EMIN_EN             1

```

```

360 SSP_GT_STRG_PCAL_CLUSTER_EMIN          100
361 SSP_GT_STRG_PCAL_CLUSTER_WIDTH        96
362
363 # DC
364 SSP_GT_STRG_DC_EN                      1
365 SSP_GT_STRG_DC_ROAD_REQUIRED           0
366 SSP_GT_STRG_DC_ROAD_INBEND_REQUIRED    0
367 SSP_GT_STRG_DC_ROAD_OUTBEND_REQUIRED   0
368 SSP_GT_STRG_DC_MULT_MIN                 5
369 SSP_GT_STRG_DC_WIDTH                    32
370
371
372
373 #####
374 #
375 # Sector Trigger bit 3
376 #
377 # DC x FTOFPCU x PCAL>15 MeV x PCAL < 60 MeV x ECAL>40 MeV x ECAL <
    120 MeV , This is Muon trigger
378 #####
379 SSP_GT_STRG                             3
380 SSP_GT_STRG_EN                           1
381
382 # PCU trigger logic
383 SSP_GT_STRG_FTOFPCU_EN                   1
384 SSP_GT_STRG_FTOFPCU_WIDTH               16
385 SSP_GT_STRG_FTOFPCU_MATCH_MASK          8
386
387 # SSP_GT_STRG_FTOFPCU_MATCH_MASK      N
388 # N: 1 = +/-0 FTOF strip tolerance
389 #   2 = +/-1 FTOF strip tolerance
390 #   4 = +/-2 FTOF strip tolerance
391 #   8 = +/-3 FTOF strip tolerance
392 #  16 = +/-4 FTOF strip tolerance
393 #  32 = +/-5 FTOF strip tolerance
394
395 # PCAL cluster trigger logic: EMIN in 0.1 MeV units
396 SSP_GT_STRG_PCAL_CLUSTER_EMIN_EN         1
397 SSP_GT_STRG_PCAL_CLUSTER_EMIN           100
398 SSP_GT_STRG_PCAL_CLUSTER_EMAX           600
399 SSP_GT_STRG_PCAL_CLUSTER_WIDTH          96
400
401 # ECAL cluster trigger logic: EMIN in 0.1MeV units
402 SSP_GT_STRG_ECAL_CLUSTER_EMIN_EN         1
403 SSP_GT_STRG_ECAL_CLUSTER_EMIN           400
404 SSP_GT_STRG_ECAL_CLUSTER_EMAX           1200
405 SSP_GT_STRG_ECAL_CLUSTER_WIDTH          96
406
407 # DC
408 SSP_GT_STRG_DC_EN                      1
409 SSP_GT_STRG_DC_ROAD_REQUIRED           0
410 SSP_GT_STRG_DC_ROAD_INBEND_REQUIRED    0
411 SSP_GT_STRG_DC_ROAD_OUTBEND_REQUIRED   0
412 SSP_GT_STRG_DC_MULT_MIN                 5
413 SSP_GT_STRG_DC_WIDTH                    32
414
415
416 #####
417 #
418 # Sector Trigger bit 4 #
419 #
420 # DC x FTOFPCU x PCAL>15 MeV x CTOF
421 #####

```

```

422 SSP_GT_STRG                               4
423 SSP_GT_STRG_EN                             1
424
425 # PCU trigger logic
426 SSP_GT_STRG_FTOFPCU_EN                       1
427 SSP_GT_STRG_FTOFPCU_WIDTH                   64
428 SSP_GT_STRG_FTOFPCU_MATCH_MASK              8
429
430 # SSP_GT_STRG_FTOFPCU_MATCH_MASK    N
431 # N: 1 = +/-0 FTOF strip tolerance
432 #    2 = +/-1 FTOF strip tolerance
433 #    4 = +/-2 FTOF strip tolerance
434 #    8 = +/-3 FTOF strip tolerance
435 #   16 = +/-4 FTOF strip tolerance
436 #   32 = +/-5 FTOF strip tolerance
437
438 # PCAL cluster trigger logic: EMIN in 0.1MeV units
439 SSP_GT_STRG_PCAL_CLUSTER_EMIN_EN             1
440 SSP_GT_STRG_PCAL_CLUSTER_EMIN               100
441 SSP_GT_STRG_PCAL_CLUSTER_WIDTH              96
442
443 # CTOF logic
444 SSP_GT_STRG_CTOF_EN                           1
445 SSP_GT_STRG_CTOF_WIDTH                       64
446 SSP_GT_STRG_CTOF_MASK                       0xFF
447
448 # DC
449 SSP_GT_STRG_DC_EN                             1
450 SSP_GT_STRG_DC_ROAD_REQUIRED                  0
451 SSP_GT_STRG_DC_ROAD_INBEND_REQUIRED          0
452 SSP_GT_STRG_DC_ROAD_OUTBEND_REQUIRED         0
453 SSP_GT_STRG_DC_MULT_MIN                       5
454 SSP_GT_STRG_DC_WIDTH                          32
455
456
457 #####
458 #
459 # Sector Trigger bit 5
460 #
461 # HTCC x (PCAL+ECAL)>300MeV x PCAL>60MeV x ECAL>10MeV
462 #####
463 SSP_GT_STRG                                   5
464 SSP_GT_STRG_EN                               1
465
466 # HTCC trigger logic
467 SSP_GT_STRG_HTCC_EN                           1
468 SSP_SLOT 3      # sector 1 SSP
469 SSP_GT_STRG_HTCC_MASK                         0x0000000000FF
470 SSP_SLOT 4      # sector 2 SSP
471 SSP_GT_STRG_HTCC_MASK                         0x00000000FF00
472 SSP_SLOT 5      # sector 3 SSP
473 SSP_GT_STRG_HTCC_MASK                         0x000000FF0000
474 SSP_SLOT 6      # sector 4 SSP
475 SSP_GT_STRG_HTCC_MASK                         0x0000FF000000
476 SSP_SLOT 7      # sector 5 SSP
477 SSP_GT_STRG_HTCC_MASK                         0x00FF00000000
478 SSP_SLOT 8      # sector 6 SSP
479 SSP_GT_STRG_HTCC_MASK                         0xFF0000000000
480 SSP_SLOT all
481 SSP_GT_STRG_HTCC_WIDTH                        0
482
483 # PCAL cluster trigger logic
484 SSP_GT_STRG_PCAL_CLUSTER_EMIN_EN             1

```



```

485 SSP_GT_STRG_PCAL_CLUSTER_EMIN          600
486 SSP_GT_STRG_PCAL_CLUSTER_WIDTH        96
487
488 # ECAL cluster trigger logic
489 SSP_GT_STRG_ECAL_CLUSTER_EMIN_EN        1
490 SSP_GT_STRG_ECAL_CLUSTER_EMIN          100
491 SSP_GT_STRG_ECAL_CLUSTER_WIDTH         96
492
493 # PCAL+ECAL cluster trigger logic: EMIN in 0.1MeV units
494 SSP_GT_STRG_ECALPCAL_CLUSTER_EMIN_EN    1
495 SSP_GT_STRG_ECALPCAL_CLUSTER_EMIN      3000
496 SSP_GT_STRG_ECALPCAL_CLUSTER_WIDTH     96
497
498
499
500 #####
501 #
502 # Sector Trigger bit 6
503 #
504 #   HTCC x PCAL>300MeV
505 #####
506 SSP_GT_STRG                              6
507 SSP_GT_STRG_EN                            1
508
509 # HTCC trigger logic
510 SSP_GT_STRG_HTCC_EN                       1
511 SSP_SLOT 3      # sector 1 SSP
512 SSP_GT_STRG_HTCC_MASK                     0x0000000000FF
513 SSP_SLOT 4      # sector 2 SSP
514 SSP_GT_STRG_HTCC_MASK                     0x00000000FF00
515 SSP_SLOT 5      # sector 3 SSP
516 SSP_GT_STRG_HTCC_MASK                     0x000000FF0000
517 SSP_SLOT 6      # sector 4 SSP
518 SSP_GT_STRG_HTCC_MASK                     0x0000FF000000
519 SSP_SLOT 7      # sector 5 SSP
520 SSP_GT_STRG_HTCC_MASK                     0x00FF00000000
521 SSP_SLOT 8      # sector 6 SSP
522 SSP_GT_STRG_HTCC_MASK                     0xFF0000000000
523 SSP_SLOT all
524 SSP_GT_STRG_HTCC_WIDTH                    0
525
526 # PCAL cluster trigger logic
527 SSP_GT_STRG_PCAL_CLUSTER_EMIN_EN          1
528 SSP_GT_STRG_PCAL_CLUSTER_EMIN            3000
529 SSP_GT_STRG_PCAL_CLUSTER_WIDTH           96
530
531
532
533 #####
534 # Sector Trigger bit 7 #
535 #
536 # PCAL(> 10 MeV) ECAL(>10 MeV)
537 #####
538 SSP_GT_STRG                              7
539 SSP_GT_STRG_EN                            1
540
541 # PCAL cluster trigger logic: EMIN in 0.1 MeV units
542 SSP_GT_STRG_PCAL_CLUSTER_EMIN_EN          1
543 SSP_GT_STRG_PCAL_CLUSTER_EMIN            100
544 SSP_GT_STRG_PCAL_CLUSTER_WIDTH           96
545
546 # ECAL cluster trigger logic: EMIN in 0.1MeV units
547 SSP_GT_STRG_ECAL_CLUSTER_EMIN_EN          1

```

```

548 SSP_GT_STRG_ECAL_CLUSTER_EMIN          100
549 SSP_GT_STRG_ECAL_CLUSTER_WIDTH       96
550
551
552 #####
553 # 'SSP_GTC_' - central detectors logic
554 #####
555
556 SSP_GTC_LATENCY          5000
557
558 SSP_GTC_FT_ESUM_DELAY    0
559 SSP_GTC_FT_CLUSTER_DELAY 1180
560 SSP_GTC_FT_ESUM_INTWIDTH 0
561
562 SSP_GTC_FANOUT_ENABLE_CTOFHGCC 1
563 SSP_GTC_FANOUT_ENABLE_CND      1
564
565 #####
566 # 'SSP_GTC_CTRG_' - central detectors trigger bits
567 #####
568
569 #####
570 # Central Trigger bit 0      CTRG0:  FT(200-4000) xHD(2)
571 #####
572 SSP_GTC_CTRG 0
573
574 SSP_GTC_CTRG_EN          1
575 SSP_GTC_CTRG_FT_CLUSTER_EN 1
576 SSP_GTC_CTRG_FT_CLUSTER_EMIN 200
577 SSP_GTC_CTRG_FT_CLUSTER_EMAX 4000
578 SSP_GTC_CTRG_FT_CLUSTER_HODO_NMIN 2
579 SSP_GTC_CTRG_FT_CLUSTER_NMIN 1
580 SSP_GTC_CTRG_FT_CLUSTER_WIDTH 0
581 SSP_GTC_CTRG_FT_ESUM_EN 0
582 SSP_GTC_CTRG_FT_ESUM_EMIN 0
583 SSP_GTC_CTRG_FT_ESUM_WIDTH 0
584
585
586 #####
587 # Central Trigger bit 1      CTRG1:  FT(500-8500) 2 clusters
588 #####
589 SSP_GTC_CTRG          1
590 SSP_GTC_CTRG_EN      1
591
592 SSP_GTC_CTRG_FT_CLUSTER_MULT_EN 1
593 SSP_GTC_CTRG_FT_CLUSTER_MULT_COINCIDENCE 16
594 SSP_GTC_CTRG_FT_CLUSTER_MULT_MIN 2
595
596 SSP_GTC_CTRG_FT_CLUSTER_EMIN 500
597 SSP_GTC_CTRG_FT_CLUSTER_EMAX 8500
598 SSP_GTC_CTRG_FT_CLUSTER_HODO_NMIN 0
599 SSP_GTC_CTRG_FT_CLUSTER_NMIN 1
600 SSP_GTC_CTRG_FT_CLUSTER_WIDTH 0
601
602 #####
603 # Central Trigger bit 2      CTRG2:  FT(100-16000)
604 #####
605 SSP_GTC_CTRG          2
606 SSP_GTC_CTRG_EN      1
607
608 SSP_GTC_CTRG_FT_CLUSTER_EN 1
609 SSP_GTC_CTRG_FT_CLUSTER_EMIN 100
610 SSP_GTC_CTRG_FT_CLUSTER_EMAX 16000

```

```

611 SSP_GTC_CTRG_FT_CLUSTER_HODO_NMIN 0
612 SSP_GTC_CTRG_FT_CLUSTER_NMIN 1
613 SSP_GTC_CTRG_FT_CLUSTER_WIDTH 0
614 SSP_GTC_CTRG_FT_ESUM_EN 0
615 SSP_GTC_CTRG_FT_ESUM_EMIN 0
616 SSP_GTC_CTRG_FT_ESUM_WIDTH 0
617
618 #####
619 # Central Trigger bit 3 CTRG3: FT(300-8500)xHD(2)
620 #####
621 SSP_GTC_CTRG 3
622 SSP_GTC_CTRG_EN 1
623
624 SSP_GTC_CTRG_FT_CLUSTER_EN 1
625 SSP_GTC_CTRG_FT_CLUSTER_EMIN 300
626 SSP_GTC_CTRG_FT_CLUSTER_EMAX 8500
627 SSP_GTC_CTRG_FT_CLUSTER_HODO_NMIN 2
628 SSP_GTC_CTRG_FT_CLUSTER_NMIN 1
629 SSP_GTC_CTRG_FT_CLUSTER_WIDTH 0
630 SSP_GTC_CTRG_FT_ESUM_EN 0
631 SSP_GTC_CTRG_FT_ESUM_EMIN 0
632 SSP_GTC_CTRG_FT_ESUM_WIDTH 0
633
634
635 SSP_CRATE end
636
637
638 #####
639 # Trigger stage 3 (vtp in trig2 crate) #
640 #####
641
642 VTP_CRATE trig2vtp
643
644 ##VTP_W_OFFSET 7900
645 #VTP_W_OFFSET 7650
646 VTP_W_OFFSET 6624
647 VTP_W_WIDTH 400
648
649 # slot: 10 13 9 14 8 15 7 16 6 17 5 18 4 19 3 20
650 # payload: 1 2 3 4 5 6 7 8 9 10 11 12 13 14 15 16
651 VTP_PAYLOAD_EN 0 0 1 0 1 0 1 0 1 0 1 0 1 0 1 0
652
653
654 # global latency
655 ##VTP_GT_LATENCY 6450
656 VTP_GT_LATENCY 5426
657
658
659 VTP_GT_WIDTH 16
660
661 # TRIGGER BITS:
662 # trig number
663 # | ssp trig mask
664 # | | ssp sector mask
665 # | | | multiplicity
666 # | | | | coincidence=#extended_clock_cycles
667 # | | | | | ssp central trig mask
668 # | | | | | | delay(in 4ns ticks)
669 # | | | | | | |
670 #
671 # Electron, All Sectors with DC
672 VTP_GT_TRGBIT 0 3 63 1 1 0 0 # SSP STRG0|STRG1, SECTOR 1-6
673

```

```

674 # Electron, Individual Sectors with DC Roads
675 VTP_GT_TRGBIT 1 3 1 1 1 0 0 # SSP STRG0|STRG1, SECTOR 1
676 VTP_GT_TRGBIT 2 3 2 1 1 0 0 # SSP STRG0|STRG1, SECTOR 2
677 VTP_GT_TRGBIT 3 3 4 1 1 0 0 # SSP STRG0|STRG1, SECTOR 3
678 VTP_GT_TRGBIT 4 3 8 1 1 0 0 # SSP STRG0|STRG1, SECTOR 4
679 VTP_GT_TRGBIT 5 3 16 1 1 0 0 # SSP STRG0|STRG1, SECTOR 5
680 VTP_GT_TRGBIT 6 3 32 1 1 0 0 # SSP STRG0|STRG1, SECTOR 6
681
682 # Electron, All sectors without DC_INBEND
683 VTP_GT_TRGBIT 7 96 63 1 1 0 0 # SSP STRG5|STRG6, SECTOR 1-6
684
685 # PCAL(>10)xECAL(>10 MeV) All sectors without DC
686 VTP_GT_TRGBIT 8 128 63 1 1 0 0 # SSP STRG7, SECTOR 1-6
687
688
689 # DC x FTOFPCU x PCAL>15MeV, Individual Sectors (for tagging/
        efficiency studies)
690 VTP_GT_TRGBIT 13 4 1 1 1 0 0 # SSP STRG2, SECTOR 1
691 VTP_GT_TRGBIT 14 4 2 1 1 0 0 # SSP STRG2, SECTOR 2
692 VTP_GT_TRGBIT 15 4 4 1 1 0 0 # SSP STRG2, SECTOR 3
693 VTP_GT_TRGBIT 16 4 8 1 1 0 0 # SSP STRG2, SECTOR 4
694 VTP_GT_TRGBIT 17 4 16 1 1 0 0 # SSP STRG2, SECTOR 5
695 VTP_GT_TRGBIT 18 4 32 1 1 0 0 # SSP STRG2, SECTOR 6
696
697
698 # FTOF x PCAL>15MeV x ECAL>40MeV (2 Sectors)
699 VTP_GT_TRGBIT 19 8 9 2 1 0 6 # SSP STRG3, SECTOR 1 & 4
700 VTP_GT_TRGBIT 20 8 18 2 1 0 6 # SSP STRG3, SECTOR 2 & 5
701 VTP_GT_TRGBIT 21 8 36 2 1 0 6 # SSP STRG3, SECTOR 3 & 6
702
703
704
705 # FT(300 - 8500) MeV x DC x FTOFPCU x PCAL>15MeV x CTOF (2 Sectors)
706 VTP_GT_TRGBIT 24 16 63 1 1 8 0 # SSP STRG4, SECTOR 1-6, CTRG3
707
708 # FT(200-4000)MeV x DC x FTOFPCU x PCAL>15MeV (2 Sectors)
709 VTP_GT_TRGBIT 25 4 63 2 1 1 0 # SSP STRG2, SECTOR 1-6, CTRG0
710
711 # 2 FT clusters (500-8500)MeV
712 VTP_GT_TRGBIT 26 0 63 1 0 2 0 # CTRG1
713
714 # FT(100-8000)MeV without hodoscope
715 VTP_GT_TRGBIT 27 0 63 1 0 4 0 # CTRG2
716
717 # PULSER
718 VTP_GT_TRG 31
719 VTP_GT_TRG_PULSER_FREQ 100.0
720
721 VTP_CRATE end
722
723 #####
724 # TS settings (trig1 crate)
725 #####
726
727 TS_CRATE trig1
728
729 #lock-roc mode
730 #TS_BLOCK_LEVEL 1
731 #TS_BUFFER_LEVEL 1
732
733
734 # with micromega
735 #TS_BLOCK_LEVEL 10

```

```

736 #TS_BUFFER_LEVEL      8
737 #TS_HOLDOFF           1 30 1
738 #TS_HOLDOFF           2 30 1
739 #TS_HOLDOFF           3 30 1
740 #TS_HOLDOFF           4 30 1
741
742 # production: 5 5 15 10
743 TS_BLOCK_LEVEL        40
744 TS_BUFFER_LEVEL       8
745 TS_HOLDOFF            1  5 1
746 TS_HOLDOFF            2  5 1
747 TS_HOLDOFF            3 15 1
748 TS_HOLDOFF            4 10 1
749
750 # crashes VTPs
751 #TS_BLOCK_LEVEL       40
752 #TS_BUFFER_LEVEL      8
753 #TS_HOLDOFF           1 10 1
754 #TS_HOLDOFF           2 10 1
755 #TS_HOLDOFF           3  7 1
756 #TS_HOLDOFF           4  5 1
757
758 #
759 # TS GTP trigger mask
760 #
761 TS_GTP_INPUT_MASK    0xFFFFFFFF
762
763 #bit 28
764 ##TS_GTP_INPUT_MASK  0x10000000
765 ##TS_GTP_INPUT_MASK  0x00000000
766
767
768 #
769 # TS FP trigger mask
770 #
771 # 0x80  - FARADAY
772 # 0x100 - SVT
773 # 0x200 - CTOF
774 # 0x400 - CND
775 # 0x800 - MVT
776 # 0x1000 - helicity
777
778 TS_FP_INPUT_MASK     0x00001080
779
780 ### Faraday cup prescale
781 TS_FP_PRESCALE       8 5
782
783
784 # TS_GTP_PRESCALE bit prescale
785 # TS_FP_PRESCALE bit prescale
786 # Note: actual prescale is 2^(prescale-1)+1
787 #       prescale from 0 to 15
788 #       bit from 0 to 31  Prescale=(1-32)
789
790 #
791 # NO PRESCALE ON MAIN TRIGGER BITS 1-7
792 # PRESCALE BIT NUMBER HERE IS +1 wrt BIT DEFINITION, I.E. BIT 0
793 #   ABOVE IS BIT 1 HERE, .. , BIT 31 ABOVE is BIT 32 HERE
794
795 # TriggerBits 7-Sector 1
796 TS_GTP_PRESCALE       8 6
797

```

```

798 # TriggerBits 8-Sector 4
799 TS_GTP_PRESCALE 9 12
800
801 ##### Not used #####
802
803 # TriggerBit 9
804 TS_GTP_PRESCALE 10 15
805
806 # TriggerBit 10
807 TS_GTP_PRESCALE 11 15
808
809 # TriggerBit 11
810 TS_GTP_PRESCALE 12 15
811
812 # TriggerBit 12
813 TS_GTP_PRESCALE 13 15
814
815
816 #
817 ##### FTOF*PCU tagging triggers
818 #
819 # TriggerBit 13 DC x FTOFPCU x PCAL>15MeV, S1
820 TS_GTP_PRESCALE 14 15
821
822 # TriggerBit 14 DC x FTOFPCU x PCAL>15MeV, S2
823 TS_GTP_PRESCALE 15 15
824
825 # TriggerBit 15 DC x FTOFPCU x PCAL>15MeV, S3
826 TS_GTP_PRESCALE 16 15
827
828 # TriggerBit 16 DC x FTOFPCU x PCAL>15MeV, S4
829 TS_GTP_PRESCALE 17 15
830
831 # TriggerBit 17 DC x FTOFPCU x PCAL>15MeV, S5
832 TS_GTP_PRESCALE 18 15
833
834 # TriggerBit 18 DC x FTOFPCU x PCAL>15MeV, S6
835 TS_GTP_PRESCALE 19 15
836
837 #
838 ##### OPPOSITE SECTOR TRIGGERS #####
839 #
840
841 # TriggerBit 19 FTOFxPCALxECAL S1-4
842 TS_GTP_PRESCALE 20 0
843
844 # TriggerBit 20 FTOFxPCALxECAL S2-5
845 TS_GTP_PRESCALE 21 0
846
847 # TriggerBit 21 FTOFxPCALxECAL S3-6
848 TS_GTP_PRESCALE 22 0
849
850 ##### Not used #####
851
852 # TriggerBit 22
853 TS_GTP_PRESCALE 23 15
854
855 # TriggerBit 23
856 TS_GTP_PRESCALE 24 15
857
858 #
859 ##### FT TRIGGERS #####
860 #

```

```
861 |
862 | # TriggerBit 24 Sector4xDC
863 | TS_GTP_PRESCALE 25 6
864 |
865 | # TriggerBit 25 FTx[FTOFxPCAL]^2
866 | TS_GTP_PRESCALE 26 0
867 |
868 | # TriggerBit 26 FTx[FTOFxPCAL]^3
869 | TS_GTP_PRESCALE 27 6
870 |
871 | # TriggerBit 27 Sector5xDC
872 | TS_GTP_PRESCALE 28 15
873 |
874 |
875 |
876 |
877 | # TriggerBit 28
878 | TS_GTP_PRESCALE 29 15
879 |
880 | # TriggerBit 29
881 | TS_GTP_PRESCALE 30 15
882 |
883 | # TriggerBit 30
884 | TS_GTP_PRESCALE 31 15
885 |
886 | #Pulser
887 | TS_GTP_PRESCALE 32 0
888 |
889 | # First arg: 0-disable,
890 | #           1-enable;
891 | #           | Prescale (15-7Hz, 7-3.5kHz, 5-15kHz, 4-30kHz,
892 | #           3-60kHz)
893 | TS_RANDOM_TRIGGER 0 5
894 |
895 | TS_CRATE end
```


Appendix B

Monte Carlo Particle Numbering Scheme

The here presented Monte Carlo particle numbering scheme, introduced in 1988 and then revised in 1998 (see Yost, 1988), aims to facilitate interfacing between detectors, simulators, and event generators used in particle physics.

The numbering scheme uses 7-digit number IDs, which can be summarized in:

$$\pm n \ n_r \ n_L \ n_{q1} \ n_{q2} \ n_{q3} \ n_J. \quad (\text{B.1})$$

This kind of encoding keeps the information about spin, flavor, internal quantum numbers, etc. The following steps explain how this codification works; for more detailed information, refer to Garren, 2008.

- Particles are given positive numbers, antiparticles negative numbers. The PDG convention for mesons is used, so that K^+ and B^+ are particles.
- Quarks and leptons are numbered consecutively starting from 1 and 11 respectively; to do this they are first ordered by family and within families by weak isospin.
- In composite quark systems (diquarks, mesons, and baryons) n_{q1-3} are quark numbers used to specify the quark content, while the rightmost digit $n_J = 2J + 1$ gives the system's spin. The scheme does not cover particles of spin $J > 4$.
- Diquarks have 4-digit numbers with $n_{q1} \geq n_{q2}$ and $n_{q3} = 0$.
- The numbering of mesons is guided by the nonrelativistic (L-S decoupled) quark model.
 - The numbers specifying the meson's quark content conform to the convention $n_{q1} = 0$ and $n_{q2} \geq n_{q3}$.
 - The quark numbers of flavorless, light (u, d, s) mesons are 11 for the member of the isotriplet (π_0 , ρ_0 , etc.), 22 for the lighter isosinglet (η , ω , etc.), and 33 for the heavier isosinglet (ϕ , etc.). Since isosinglet mesons are often large mixtures of uu + dd and ss states, 22 and 33 are assigned by mass and do not necessarily specify the dominant quark composition.
 - The fifth digit n_L is reserved to distinguish mesons of the same total (J) but different spin (S) and orbital (L) angular momentum quantum numbers. For $J > 0$ the numbers are: $(L, S) = (J - 1, 1); n_L = 0$, $(J, 0); n_L = 1$, $(J, 1); n_L = 2$ and $(J + 1, 1); n_L = 3$. For the exceptional case $J = 0$ the numbers are $(0, 0); n_L = 0$ and $(1, 1); n_L = 1$.

- If a set of physical mesons correspond to a (non-negligible) mixture of basis states, differing in their internal quantum numbers, then the lightest physical state gets the smallest basis state number.
- The sixth digit n_r is used to label mesons radially excited above the ground state.
- Numbers have been assigned for complete $n_r = 0$ S - and P -wave multiplets, even where states remain to be identified.
- In some instances assignments within the qq^- meson model are only tentative; here best guess assignments are made.
- Many states appearing in the Meson Listings are not yet assigned within the qq^- model. Here n_{q2-3} and n_J are assigned according to the state's likely flavors and spin; all such unassigned light isoscalar states are given the flavor code 22. Within these groups $n_L = 0, 1, 2, \text{etc.}$ is used to distinguish states of increasing mass. These states are flagged using $n = 9$. It is to be expected that these numbers will evolve as the nature of the states is elucidated. Codes are assigned to all mesons which are listed in the one-page table at the end of the Meson Summary Table as long as they have a preferred or established spin. Additional heavy meson states expected from heavy quark spectroscopy are also assigned codes.
- The numbering of baryons is again guided by the nonrelativistic quark model.
 - The numbers specifying a baryon's quark content are such that in general $n_{q1} \geq n_{q2} \geq n_{q3}$.
 - Two states exist for $J = 1/2$ baryons containing 3 different types of quarks. In the lighter baryon the light quarks are in an antisymmetric ($J = 0$) state while for the heavier baryon, they are in a symmetric ($J = 1$) state. In this situation n_{q2} and n_{q3} are reversed for the lighter state so that the smaller number corresponds to the lighter baryon.
 - At present most Monte Carlos do not include excited baryons and no systematic scheme has been developed to denote them, though one is foreseen. In the meantime, the use of the PDG 96 [5] numbers for excited baryons is recommended.
 - For pentaquark states $n = 9$, $n_r n_L n_{q1} n_{q2}$ gives the four quark numbers in order $n_r \geq n_L \geq n_{q1} \geq n_{q2}$, n_{q3} gives the antiquark number, and $n_J = 2J + 1$, with the assumption that $J = 1/2$ for the states currently reported.

Monte Carlo Particle Numbering List							
Leptons		Gauge Bosons		Light I=1 Mesons		Light Baryons	
e^-	11	g	21	π^0	11	p	2212
ν_e	12	γ	22	π^+	211	n	2112
μ^-	13	Z^0	23	$\rho(770)^0$	113	Δ^{++}	2224
ν_μ	14	W^+	24	$\rho(770)^+$	213	Δ^+	2214
τ^-	15	Z'/Z_2^0	32	$a_2(1320)^0$	115	Δ^0	2114
ν_τ	16	Z''/Z_3^0	33	$a_2(1320)^+$	215	Δ^-	1114

TABLE B.1: Monte Carlo particle numbering list example, reporting the most used codes in the carried-out analysis.

Appendix C

CLAS12Root Classes and Methods

A brief example of code showing the most recurring classes and methods, reported in listing C.1, will be now presented and commented on, focusing on the parts of the code fundamental to understanding the following steps.

LISTING C.1: CLAS12ROOT example code, demonstrating how to extract particle information from hipo files. Some of most used classes and methods are here shown.

```

1 //Opening file.
2 clas12reader c12("my/hipo/file.hipo");
3
4 //Looping over events.
5 while(c12.next())
6 {
7     // Checking if the event is empty.
8     if(!c12.getDetParticles().empty())
9     {
10
11         // Defining a std::vector of particles from FT detector.
12         auto particlesFT=c12.getByRegion(clas12::FT);
13
14         CountAndIndex(particlesFT, idx, nElectrons, idxElectrons, nPhotons
15             , idxPhotons);
16
17         // Ignore events with less than 1 e- and 2 g
18         if (nElectrons==1 && nPhotons==2)
19         {
20             for (int ii=0;ii<particlesFT.size();ii++)
21             {
22
23                 // Checking dt only between electrons and photon. Here checking
24                 // which particle is an electron //
25                 if(std::find(idxElectrons.begin(), idxElectrons.end(), ii) !=
26                     idxElectrons.end())
27                 {
28                     // Fixing counter for vector index //
29                     int counter=0;
30
31                     // Retrieving electron informations //
32                     InfoRetrieving(particlesFT, ii, CorrectTime, counter, Pe, PeNew
33                         , Pg1, Pg2, intime, PID);
34
35                     for (int jj=0;jj<particlesFT.size();jj++)
36                     {
37                         // Checking if the other particle is a photon //
38                         if(ii != jj)

```

```

38     {
39
40         // Retrieving photon informations //
41         InfoRetrieving(particlesFT, jj, CorrectTime, counter, Pe,
42                       PeNew, Pg1, Pg2, intime, PID);
43     }
44 }
45 }
46 }
47 }
48 }
49 }
50
51 ///////////////////////////////////////////////////////////////////
52 ////////////// Particles indexing ///////////////////////////////////
53 ///////////////////////////////////////////////////////////////////
54
55 void CountAndIndex(vector<region_part_ptr> particlesFT, int &idx,
56                  int &nElectrons, vector<int> &idxElectrons, int &nPhotons,
57                  vector<int> &idxPhotons){
58
59     for (auto particle : particlesFT)
60     {
61
62         switch (particle->getPid())
63         {
64
65             case 11:
66                 nElectrons++;
67                 idxElectrons.push_back(idx);
68                 break;
69             case 22:
70                 nPhotons++;
71                 idxPhotons.push_back(idx);
72
73         }
74
75         idx++;
76     }
77 }
78 ///////////////////////////////////////////////////////////////////
79 ////////////// Data collector ///////////////////////////////////
80 ///////////////////////////////////////////////////////////////////
81
82 void InfoRetrieving(vector<region_part_ptr> particlesFT, int
83                   PartIndex, double CorrectTime[3], int &counter, TLorentzVector *
84                   Pe, TLorentzVector *PeNew, TLorentzVector *Pg1, TLorentzVector *
85                   Pg2, int &intime, int PID[3]){
86
87     TimeRetriever(particlesFT, PartIndex, CorrectTime, counter);
88     MomentumRetriever(particlesFT, PartIndex, counter, Pe, PeNew, Pg1,
89                       Pg2);
90
91     if(counter!=0)
92     {
93         auto dT=CorrectTime[0]-CorrectTime[counter];
94
95         // Checking for time coincidence //

```

```

94     if (fabs(dT)<DELTA_TIME)
95         intime++;
96     }
97
98     PID[counter] = particlesFT[PartIndex]->getPid();
99     counter++;
100
101 }
102
103 ///////////////////////////////////////////////////////////////////
104 /////////////// Time collector ///////////////////////////////////
105 ///////////////////////////////////////////////////////////////////
106
107 void TimeRetriever(vector<region_part_ptr> particlesFT, int
108     PartIndex, double CorrectTime[3], int &counter){
109
110     if(particlesFT[PartIndex]->ftbpar()->getRows()!=0 && particlesFT[
111         PartIndex]->getPid()==11)
112         CorrectTime[counter]=particlesFT[PartIndex]->ftbpar()->getVt();
113     else
114     {
115         TVector3 pos1(particlesFT[PartIndex]->ft(FTCAL)->getX(),
116             particlesFT[PartIndex]->ft(FTCAL)->getY(),particlesFT[
117                 PartIndex]->ft(FTCAL)->getZ());
118         CorrectTime[counter]=((particlesFT[PartIndex]->ft(FTCAL)->getTime
119             ())- (pos1.Mag()/clight));
120     }
121 }
122
123 ///////////////////////////////////////////////////////////////////
124 /////////////// Momentum collector ///////////////////////////////////
125 ///////////////////////////////////////////////////////////////////
126
127 void MomentumRetriever(vector<region_part_ptr> particlesFT, int
128     PartIndex, int &counter, TLorentzVector *Pe, TLorentzVector *
129     PeNew, TLorentzVector *Pg1, TLorentzVector *Pg2){
130
131     if(particlesFT[PartIndex]->getPid()==11)
132     {
133         Pe->SetXYZM(particlesFT[PartIndex]->par()->getPx(),particlesFT[
134             PartIndex]->par()->getPy(),particlesFT[PartIndex]->par()->
135             getPz(),0.511E-3);
136         *PeNew = Correct_Electron(*Pe);
137     }
138
139     if(counter==1)
140     {
141         Pg1->SetXYZM(particlesFT[PartIndex]->par()->getPx(),particlesFT[
142             PartIndex]->par()->getPy(),particlesFT[PartIndex]->par()->
143             getPz(),0);
144     }
145
146     else if(counter==2)
147     {

```

```

145 | Pg2->SetXYZM(particlesFT[PartIndex]->par()->getPx(),particlesFT[
    | PartIndex]->par()->getPy(),particlesFT[PartIndex]->par()->
    | getPz(),0);
146 |
147 | }
148 | }

```

- **clas12reader**: as can be seen at line 1, the *clas12reader* class creates an object, here called *c12*, containing all the information stored inside the selected hipo file. Now *c12* can be used to call every *clas12root* method.
 - **getDetParticles**: the next *clas12reader* method, shown in the code at line 7, is *getDetParticles*. As can be intended from the name of this method, it reads from the hipo file a list of the detected particle for the current event. Each one of the particles, which can be extracted inside a *std::vector*, is a *particle*-type object, which will be later discussed in this list. Here, *getDetParticles* is paired with another C++ method: *empty*. In this case, the *empty* method check that the event under analysis has particles in it. This is an important check because any kind of bug or error can occur during data reconstruction, producing existing events without particles. The output of this method is a boolean, which can be true or false.
 - **getByRegion**: if requested, the code can selectively extract the particles needed from your event, via the *getByRegion* method (11). This method requires a parameter, which can be *FT*, *FD*, or *CD*, respectively selecting the event particles detected in the Forward Tagger, Forward Detector, and Central Detector. The resulting vector is the same as seen before for *getDetParticles*.
- **particle**: *particle*-type objects are the most used in this analysis, carrying all the particle information necessary to proceed in the study. They got a wide set of methods, most of which will be now presented.

Objects and methods not here explained will have a brief description when shown later in the thesis.

- **getPid**: extracting the particle identification code, this method is fundamental for the understanding of what kind of particles are involved in the analyzed event. More information about the PID can be found in Appendix B. The output of *getPid* is an *int* value, and the most recurring PID in our code, for example, used at line 63 and 67, are 11 (electrons) and 22 (photons).
- **ftbpar**: this method makes the user capable to access all the parameter contained in the forward tagger bank. *ftbpar* is shown along two other methods: the C++ method *getRows* (109) and *getVt* (110). The first one is here used to check the FT banks: if the event is empty, this process is skipped; the second one extract the *Vertex Time* for the electron of the current event, where the vertex is the track position with the smallest distance to the beam axis.
- **ft**: the *ft* method can access the banks of every forward tagger detector; as can be seen at line 116, the detector has to be chosen as the option of the *ft* method. The information can be then accessed using *getX*, *getY*, *getZ* (detection coordinates), *getTime* (detection time), etc. Examples in listing at line 116.

- **par**: in case some other reconstructed information is needed, the method *par* can extract them from a *particle*-type object. For example, the extraction of the momenta via *getPz*, *getPy*, *getPx* can be seen at lines 130.

Bibliography

- Acker, A. et al. (2020a). “The CLAS12 Forward Tagger”. In: *Nucl. Instrum. Meth. A* 959, p. 163475. DOI: [10.1016/j.nima.2020.163475](https://doi.org/10.1016/j.nima.2020.163475).
- (2020b). “The CLAS12 Micromegas Vertex Tracker”. In: *Nucl. Instrum. Meth. A* 957, p. 163423. DOI: [10.1016/j.nima.2020.163423](https://doi.org/10.1016/j.nima.2020.163423).
- Agostinelli, S. et al. (2003). “GEANT4—a simulation toolkit”. In: *Nucl. Instrum. Meth. A* 506, pp. 250–303. DOI: [10.1016/S0168-9002\(03\)01368-8](https://doi.org/10.1016/S0168-9002(03)01368-8).
- Al Ghouli, H. et al. (2017). “Measurement of the beam asymmetry Σ for π^0 and η photoproduction on the proton at $E_\gamma = 9$ GeV”. In: *Phys. Rev. C* 95.4, p. 042201. DOI: [10.1103/PhysRevC.95.042201](https://doi.org/10.1103/PhysRevC.95.042201). arXiv: [1701.08123](https://arxiv.org/abs/1701.08123) [nucl-ex].
- Al Ghouli, H. et al. (2021). “The GlueX beamline and detector”. In: *Nuclear Instruments and Methods in Physics Research Section A: Accelerators, Spectrometers, Detectors and Associated Equipment* 987, p. 164807. ISSN: 0168-9002. DOI: <https://doi.org/10.1016/j.nima.2020.164807>.
- Amarian, M. et al. (2001). “The CLAS forward electromagnetic calorimeter”. In: *Nucl. Instrum. Meth. A* 460, pp. 239–265. DOI: [10.1016/S0168-9002\(00\)00996-7](https://doi.org/10.1016/S0168-9002(00)00996-7).
- Anderson, R. L. et al. (Oct. 1971). “High-Energy π^0 Photoproduction from Hydrogen with Unpolarized and Linearly Polarized Photons”. In: *Phys. Rev. D* 4 (7), pp. 1937–1946. DOI: [10.1103/PhysRevD.4.1937](https://doi.org/10.1103/PhysRevD.4.1937). URL: <https://link.aps.org/doi/10.1103/PhysRevD.4.1937>.
- Antonioli, M. A. et al. (2020). “The CLAS12 Silicon Vertex Tracker”. In: *Nucl. Instrum. Meth. A* 962, p. 163701. DOI: [10.1016/j.nima.2020.163701](https://doi.org/10.1016/j.nima.2020.163701).
- Asryan, G. et al. (2020). “The CLAS12 forward electromagnetic calorimeter”. In: *Nucl. Instrum. Meth. A* 959, p. 163425. DOI: [10.1016/j.nima.2020.163425](https://doi.org/10.1016/j.nima.2020.163425).
- Bacchetta, Alessandro et al. (2004). “Single-spin asymmetries: The Trento conventions”. In: *Phys. Rev. D* 70, p. 117504. DOI: [10.1103/PhysRevD.70.117504](https://doi.org/10.1103/PhysRevD.70.117504). arXiv: [hep-ph/0410050](https://arxiv.org/abs/hep-ph/0410050).
- Baltzell, N. et al. (2018). *CLAS12 Offline Software*. <https://github.com/JeffersonLab/clas12-offline-software>.
- (2019). *Accesssing Bank Data In C++*. <https://github.com/JeffersonLab/clas12root/blob/master/docs/AccesssingBankDataInCpp.txt>.
- (2020). “The CLAS12 beamline and its performance”. In: *Nucl. Instrum. Meth. A* 959, p. 163421. DOI: [10.1016/j.nima.2020.163421](https://doi.org/10.1016/j.nima.2020.163421).
- Battaglieri, M. et al. (2005). “Experiment E12-11-005 Meson Spectroscopy with low Q^2 electron scattering in CLAS12”.
- (2015). “CLAS12 Forward Tagger (FT) Technical Design Report”. URL: <https://www.ge.infn.it/~batta/jlab/ft-tdr.2.2.pdf>.
- Bedlinskiy, I. et al. (2014). “Exclusive π^0 electroproduction at $W > 2$ GeV with CLAS”. In: *Phys. Rev. C* 90.2. [Addendum: *Phys. Rev. C* 90, 039901 (2014)], p. 025205. DOI: [10.1103/PhysRevC.90.039901](https://doi.org/10.1103/PhysRevC.90.039901). arXiv: [1405.0988](https://arxiv.org/abs/1405.0988) [nucl-ex].
- Boyarinov, S. et al. (2020). “The CLAS12 Data Acquisition System”. In: *Nucl. Instrum. Meth. A* 966, p. 163698. DOI: [10.1016/j.nima.2020.163698](https://doi.org/10.1016/j.nima.2020.163698).

- Brun, R. and F. Rademakers (1997). “ROOT: An object oriented data analysis framework”. In: *Nucl. Instrum. Meth. A* 389. Ed. by M. Werlen and D. Perret-Gallix, pp. 81–86. DOI: [10.1016/S0168-9002\(97\)00048-X](https://doi.org/10.1016/S0168-9002(97)00048-X).
- Burkert, V. D. et al. (2020). “The CLAS12 Spectrometer at Jefferson Laboratory”. In: *Nucl. Instrum. Meth. A* 959, p. 163419. DOI: [10.1016/j.nima.2020.163419](https://doi.org/10.1016/j.nima.2020.163419).
- Carman, D. S. et al. (2020a). “The CLAS12 Central Time-of-Flight system”. In: *Nucl. Instrum. Meth. A* 960, p. 163626. DOI: [10.1016/j.nima.2020.163626](https://doi.org/10.1016/j.nima.2020.163626).
- (2020b). “The CLAS12 Forward Time-of-Flight system”. In: *Nucl. Instrum. Meth. A* 960, p. 163629. DOI: [10.1016/j.nima.2020.163629](https://doi.org/10.1016/j.nima.2020.163629).
- Chatagnon, P. et al. (2020). “The CLAS12 Central Neutron Detector”. In: *Nucl. Instrum. Meth. A* 959, p. 163441. DOI: [10.1016/j.nima.2020.163441](https://doi.org/10.1016/j.nima.2020.163441).
- Collins, P. D. B. (May 2009). *An Introduction to Regge Theory and High-Energy Physics*. Cambridge Monographs on Mathematical Physics. Cambridge, UK: Cambridge Univ. Press. ISBN: 978-0-521-11035-8. DOI: [10.1017/CB09780511897603](https://doi.org/10.1017/CB09780511897603).
- Collins, P. D. B. and T. D. B. Wilkie (1981). “Regge Cuts and Neutral Pion Electroproduction”. In: *Z. Phys. C* 7, p. 357. DOI: [10.1007/BF01431568](https://doi.org/10.1007/BF01431568).
- Contalbrigo, M. et al. (2020). “The CLAS12 Ring Imaging Cherenkov detector”. In: *Nucl. Instrum. Meth. A* 964, p. 163791. DOI: [10.1016/j.nima.2020.163791](https://doi.org/10.1016/j.nima.2020.163791).
- De Vita, R. et al. (2018). *Jefferson Lab 12-GeV Experimental Computing Review: CLAS12 Software and Computing Overview*. https://indico.jlab.org/event/294/contributions/4400/attachments/3566/4319/20181126_clas12_devita_V1_full.pdf.
- Donnachie, A. and Yu. S. Kalashnikova (2016). “Photoproduction of $a_0(980)$ and $f_0(980)$ ”. In: *Phys. Rev. C* 93.2, p. 025203. DOI: [10.1103/PhysRevC.93.025203](https://doi.org/10.1103/PhysRevC.93.025203). arXiv: [1507.07408](https://arxiv.org/abs/1507.07408) [hep-ph].
- Fair, R. et al. (2020). “The CLAS12 superconducting magnets”. In: *Nucl. Instrum. Meth. A* 962, p. 163578. DOI: [10.1016/j.nima.2020.163578](https://doi.org/10.1016/j.nima.2020.163578).
- Garren, L. et al. (2008). *Monte Carlo particle numbering scheme*. <https://pdg.lbl.gov/2008/reviews/rpp2008-rev-monte-carlo-numbering.pdf>.
- Gavalian, G. et al. (2018). *HIPO File Format*. https://userweb.jlab.org/~gavalian/docs/sphinx/hipo/html/chapters/hipo_introduction.html.
- Glazier, D. et al. (2019a). *BruFit: a RooFit based event based maximum likelihood fitting package*. <https://github.com/dglazier/brufit>.
- (2019b). *CLAS12ROOT – CLAS12 analysis tools for HIPO data using C++ and ROOT*. <https://github.com/JeffersonLab/clas12root>.
- Goldstein, G. R. and J. F. Owens (1973). “ π^0 photoproduction in a weak-regge-cut model”. In: *Phys. Rev. D* 7, pp. 865–879. DOI: [10.1103/PhysRevD.7.865](https://doi.org/10.1103/PhysRevD.7.865).
- Goloskokov, S. V. and P. Kroll (2010). “An Attempt to understand exclusive π^+ electroproduction”. In: *Eur. Phys. J. C* 65, pp. 137–151. DOI: [10.1140/epjc/s10052-009-1178-9](https://doi.org/10.1140/epjc/s10052-009-1178-9). arXiv: [0906.0460](https://arxiv.org/abs/0906.0460) [hep-ph].
- Halzen, F. and A. D. Martin (1984). *Quarks and Leptons: An Introductory Course in Modern Particle Physics*. New Publisher, 978-0471887416.
- Hand, L. N. (1963). “Experimental investigation of pion electroproduction”. In: *Phys. Rev.* 129, pp. 1834–1846. DOI: [10.1103/PhysRev.129.1834](https://doi.org/10.1103/PhysRev.129.1834).
- Jacob, M. and G. C. Wick (1959). “On the General Theory of Collisions for Particles with Spin”. In: *Annals Phys.* 7, pp. 404–428. DOI: [10.1016/0003-4916\(59\)90051-X](https://doi.org/10.1016/0003-4916(59)90051-X).
- Kubarovsky, V. (2020). *CLAS12 Trigger*. https://wiki.jlab.org/physdivwiki/images/4/4d/Trigger_task_force.pdf.
- Laget, J. M. (2011). “Unitarity constraints on neutral pion electroproduction”. In: *Phys. Lett. B* 695, pp. 199–204. DOI: [10.1016/j.physletb.2010.11.014](https://doi.org/10.1016/j.physletb.2010.11.014). arXiv: [1004.1949](https://arxiv.org/abs/1004.1949) [hep-ph].

- Leemann, C. W., D. R. Douglas, and G. A. Krafft (2001). “The Continuous Electron Beam Accelerator Facility: CEBAF at the Jefferson Laboratory”. In: *Ann. Rev. Nucl. Part. Sci.* 51, pp. 413–450. DOI: [10.1146/annurev.nucl.51.101701.132327](https://doi.org/10.1146/annurev.nucl.51.101701.132327).
- López, R. Delgado (2017). *Study of the Electroweak Symmetry Breaking Sector for the LHC*. Springer. DOI: [10.1007/978-3-319-60498-5](https://doi.org/10.1007/978-3-319-60498-5).
- Mathieu, V. et al. (2018). “Structure of Pion Photoproduction Amplitudes”. In: *Phys. Rev. D* 98.1, p. 014041. DOI: [10.1103/PhysRevD.98.014041](https://doi.org/10.1103/PhysRevD.98.014041). arXiv: [1806.08414](https://arxiv.org/abs/1806.08414) [hep-ph].
- Mathieu, V. et al. (2015). “Neutral pion photoproduction in a Regge model”. In: *Physical Review D* 92. DOI: [10.1103/physrevd.92.074013](https://doi.org/10.1103/physrevd.92.074013).
- Mestayer, M. D. et al. (2020). “The CLAS12 drift chamber system”. In: *Nucl. Instrum. Meth. A* 959, p. 163518. DOI: [10.1016/j.nima.2020.163518](https://doi.org/10.1016/j.nima.2020.163518).
- Newton, J. (2021). “ J/ψ Photoproduction Near Threshold with CLAS12”. PhD thesis. Old Dominion University.
- Pilloni A., Celentano A. (n.d.). *AMPTOOLS implementation of Regge model for π^0 photoproduction*.
- Pivk, Muriel and Francois R. Le Diberder (2005). “SPlot: A Statistical tool to unfold data distributions”. In: *Nucl. Instrum. Meth. A* 555, pp. 356–369. DOI: [10.1016/j.nima.2005.08.106](https://doi.org/10.1016/j.nima.2005.08.106). arXiv: [physics/0402083](https://arxiv.org/abs/physics/0402083).
- Schilling, K., P. Seyboth, and Guenter E. Wolf (1970). “On the Analysis of Vector Meson Production by Polarized Photons”. In: *Nucl. Phys. B* 15. [Erratum: *Nucl.Phys.B* 18, 332 (1970)], pp. 397–412. DOI: [10.1016/0550-3213\(70\)90070-2](https://doi.org/10.1016/0550-3213(70)90070-2).
- Segarra, E. P. et al. (2020). “The CLAS12 Backward Angle Neutron Detector (BAND)”. In: *Nucl. Instrum. Meth. A* 978, p. 164356. DOI: [10.1016/j.nima.2020.164356](https://doi.org/10.1016/j.nima.2020.164356). arXiv: [2004.10339](https://arxiv.org/abs/2004.10339) [physics.ins-det].
- Sharabian, Y. G. et al. (2020). “The CLAS12 high threshold Cherenkov counter”. In: *Nucl. Instrum. Meth. A* 968, p. 163824. DOI: [10.1016/j.nima.2020.163824](https://doi.org/10.1016/j.nima.2020.163824).
- Ungaro, M. (2019). *The LUND Format*. <https://gemc.jlab.org/gemc/html/documentation/generator/lund.html>.
- Ungaro, M. et al. (2020a). “The CLAS12 Geant4 simulation”. In: *Nucl. Instrum. Meth. A* 959, p. 163422. DOI: [10.1016/j.nima.2020.163422](https://doi.org/10.1016/j.nima.2020.163422).
- (2020b). “The CLAS12 Low Threshold Cherenkov detector”. In: *Nucl. Instrum. Meth. A* 957, p. 163420. DOI: [10.1016/j.nima.2020.163420](https://doi.org/10.1016/j.nima.2020.163420).
- Walker, R. L. (1969). “Phenomenological analysis of single pion photoproduction”. In: *Phys. Rev.* 182, pp. 1729–1748. DOI: [10.1103/PhysRev.182.1729](https://doi.org/10.1103/PhysRev.182.1729).
- Yost, G. P. et al. (1988). “Review of Particle Properties: Particle Data Group”. In: *Phys. Lett. B* 204, pp. 1–486. DOI: [10.1016/0370-2693\(88\)90505-9](https://doi.org/10.1016/0370-2693(88)90505-9).
- Ziegler, V. et al. (2020). “The CLAS12 software framework and event reconstruction”. In: *Nuclear Instruments and Methods in Physics Research Section A: Accelerators, Spectrometers, Detectors and Associated Equipment* 959, p. 163472. ISSN: 0168-9002. DOI: <https://doi.org/10.1016/j.nima.2020.163472>.